8-2016

Modeling picking on pharmaceutical tablets

Shrikant Swaminathan
Purdue University

PURDUE UNIVERSITY
GRADUATE SCHOOL
Thesis/Dissertation Acceptance

This is to certify that the thesis/dissertation prepared

By Shrikant Swaminathan

Entitled
Modeling Picking on Pharmaceutical Tablets

For the degree of   Doctor of Philosophy

Is approved by the final examining committee:

Prof. Carl R. Wassgren Jr.
Chair

Prof. Charles M. Krousgrill

Prof. Marcial Gonzalez

Prof. Rose Prabin Kingsly Ambrose

To the best of my knowledge and as understood by the student in the Thesis/Dissertation Agreement, Publication Delay, and Certification Disclaimer (Graduate School Form 32), this thesis/dissertation adheres to the provisions of Purdue University's "Policy of Integrity in Research" and the use of copyright material.

Approved by Major Professor(s):   Prof. Carl R. Wassgren Jr.

Approved by: Prof. Jay P. Gore   07/18/2016

Head of the Departmental Graduate Program   Date

MODELING PICKING ON PHARMACEUTICAL TABLETS

A Dissertation

Submitted to the Faculty

of

Purdue University

by

Shrikant Swaminathan

In Partial Fulfillment of the

Requirements for the Degree

of

Doctor of Philosophy

August 2016

Purdue University

West Lafayette, Indiana

Dedicated to my beloved parents.

ACKNOWLEDGMENTS

"If you fail, never give up because 'F.A.I.L.' means **F**irst **A**ttempt **I**n **L**earning. End is not the end, in fact 'E.N.D.' means **E**ffort **N**ever **D**ies. If you get no as an answer, remember 'N.O.' means **N**ext **O**pportunity. So, lets be positive !"– A.P.J Kalam

As a graduate student at Purdue University for almost seven years there are many wonderful people who have helped me though my scientific journey and have been instrumental in making this dissertation possible. It is my pleasure to thank each and every one of you.

I owe my deepest gratitude to my advisor Prof. Carl R. Wassgren for his guidance and patience at every step of the way. Professor Wassgren you have given me the freedom and opportunity to develop as a researcher. I have learned a lot from you and hope to follow your systematic approach to research for the rest of my life. I would also like to extend my gratitude to Prof. Ambrose, Prof. Gonzalez, Prof. Litster and Prof. Krousgrill for their service on my examination committee. Their feedback related to my dissertation work is greatly appreciated.

I am grateful to Dr. Jon Hilden and Mr. Brian Ramey at the 'Eli Lilly and Company and Company'for their constant encouragement and support of my work. I appreciate your weekly feedback over the past three years in shaping my work.

I would like to thank Bill Turner and Chuck Kettler at 'Natoli Engineering Company Inc.'for their help in making the specialty punches and dies used in this work. A special thanks to Jeffery Huddleston at the 'Artisan and Fabrication Laboratory'(AFL), not only for all the technical support in making the 'Purdue in-house compaction simulator'but also for your friendship. A special thanks to Pam Lachcik for taking the time to train me on the XRCT instrument and answering all my queries.

I am also grateful to Prof. Jennifer Sinclair Curtis, Dr. Bruno Hancock and Dr. William Ketterhagen who made their valuable time available every week during the initial stages of my graduate work. Your guidance helped me stay on the right path and helped me in my research work. A special thanks to my internship mentors Daniel Blackwood [1], Dr. Ariel Muliadi [2], Dr. Pingjun Tang [2], Dr. Joseph Bullard [2], Dr. Tuhin Sinha [3], Dr. Kamal Sikka [3] and Randy Werner [3] for shaping and honing my research skills.

It has been my pleasure to have worked with some of the finest research students in my lab. Avik, Ben, Harsh, Kevin, Liza, Madhusudan, Mohammad, Nathan, PJ, Rahul, Rohit, Shankali, Siddhartha, Simseok, Tuhin, Tim and Yu. I would like to thank you for putting up with my eccentricities in the lab and providing constructive feedback during our weekly group meetings. I would like to specially acknowledge Avik, Ben, Rahul, Rohit, Tuhin and Yu for the enlightening scientific discussions. You guys have helped me in my research in numerous ways.

I would like to thank Abishek, Bryan, Dustin, Eli, Fouad, Ganeshchandra, Sree Harshita, Krishnan, Kartik, Leonid, Michael(s), Patrick, Praneet, Priyanka, Pratik, Rohit, Sudarshan, Sukanya, Swathi and Tyler for providing the necessary comic relief. You guys helped me relax and maintain my sanity. I will always miss the fun times I have had with each and every one of you. I would also like to thank Prof. William Oakes, Prof. Carla Zoltowski and the entire EPICS staff at Purdue for helping me contribute to society using my engineering skills. Everyone, I would like you to know that even though you were not directly related to my research work I cannot imagine this journey without your support.

I would now like to thank the people who are closest to me. Anand and Yuvraj thank you for being my apartment mates for the last four years. Seeing you guys work hard always keeps me motivated. Next I would like to thank my Krishnan Chitappa and Usha Chitti. Chitappa and Chitti without your support this journey would have

---

[1] Pfizer Worldwide Research and Development, Pfizer Inc., Groton CT.

[2] Material Assessment Group, Vertex Pharmaceuticals Inc., Boston MA.

[3] IBM Microelectronics, Hopewell Junction, NY.

been over even before it started. For this I will always be in your debt. I would like to extend my sincerest thanks to all the members of my family for their encouragement. Finally, the credit for all my success goes to the hardwork and sacrifice of my parents. Appa thank you for always believing in me and being an example of hardwork and selflessness. Amma thank you for dedicating your life to my well being, loving me, caring for me and fighting my battles when I couldn't do so myself. Amma and Appa I thank you for your patience and dedicate this dissertation to you!

TABLE OF CONTENTS

LIST OF TABLES

LIST OF FIGURES

SYMBOLS

p Hydrostatic stress $[N/m^2]$

p_u Hyrdostatic stress during uniaxial compression $[N/m^2]$

p_d Hydrostatic stress during diametrical compression test $[N/m^2]$

p_c Hydrostatic stress during powder compaction test $[N/m^2]$

q Mises equivalent stress $[N/m^2]$

q_u Mises equivalent stress during uniaxial compression $[N/m^2]$

q_d Mises equivalent stress during diametrical compression test $[N/m^2]$

q_c Mises equivalent stress during powder compaction test $[N/m^2]$

S_{ij} Deviatoric stress $[N/m^2]$

δ_{ij} Dirac delta operator

σ_{ij} Stress tensor $[N/m^2]$

σ_u Uniaxial compression breakage stress $[N/m^2]$

σ_d Diametrical compression breakage stress $[N/m^2]$

$\sigma_{c,r}$ Radial stress during powder compression test $[N/m^2]$

$\sigma_{c,x}$ Axial stress during powder compression test $[N/m^2]$

ϵ_{vol}^p Volumetric plastic strain

ϵ_e elastic strain

ϵ_p plastic strain

F_u Uniaxial compression breakage force $[N]$

F_d Diametrical compression breakage force $[N]$

d Cohesion $[N/m^2]$

β Internal friction angle $[°]$

F_s Shear line

F_t Transition curve

F_c	Elliptical cap
R	Cap eccentricity parameter
α	Transition constant
p_a	Stress evolution parameter $[N/m^2]$
p_b	Hydrostatic yield stress $[N/m^2]$
m	mass$[kg]$
η	Relative density
h	Compact height $[m]$
ϵ	Waimer shear cone angle $[°]$
v	velocity $[m/s]$
D	Diameter of the cylindrical compact
t	Thickness of the cylindrical compact
ρ	Apparent Density of the powder compact $[g/cm^3]$
ρ_{true}	True density $[g/cm^3]$
E	Young's modulus $[N/m^2]$
G	Shear modulus $[N/m^2]$
ν	Poisson's ratio
F_{upper}	Upper punch load $[N]$
F_{lower}	Lower punch load $[N]$
μ	Coefficient of static friction
μ_w	Wall friction
b	Contact half width $[m]$
R	Platen Radius $[m]$
d_{50}	Median particle size
τ_n	Maximum failure traction $[N/m^2]$
δ_m	Damage initiation point $[\mu m]$
δ_t	Termination point $[\mu m]$
g	Plastic potential
τ_n	Peak adhesive traction

δ_m	Displacement at peak adhesive traction
δ_t	Displacement at termination of adhesive traction
K	Stress intensity factor
G_{ERR}	Energy release rate
K_{IC}	Critical stress intensity factor in mode I
$P_f racture$	Peak fracture load
$a_n otch$	Height of the notch
L_{beam}	Length of rectangular specimen
h_{beam}	Height of rectangular specimen
b_{beam}	Width of rectangular specimen
γ	Compatibility curve

ABBREVIATIONS

2D	Two Dimensional
3D	Three Dimensional
AFM	Atomic Force Microscope
DEM	Discrete Element Method
DPC	Drucker-Prager Cap
FDA	Food and Drug Administration
FEM	Finite Element Method
LEFM	Linear Elastic Fracture Mechanics
PAT	Process Analytical Technology
QbD	Quality by Design
RD	Relative Density
RH	Relative Humidity
SF	Solid Fraction
SFA	Surface Force Apparatus
SENB	Single Edge Notch Bend (test)
XRCT	X-ray Computed Micro Tomography

NOMENCLATURE

APAP   Acetaminophen

ASA   Acetylsalicylic Acid

IBU   Ibuprofen

MCC   Microcrystalline Cellulose

MgSt   Magnesium Stearate

ABSTRACT

Swaminathan, Shrikant Ph.D., Purdue University, August 2016. Modeling Picking on Pharmaceutical Tablets. Major Professor: Carl R. Wassgren, School of Mechanical Engineering.

Tablets are the most popular solid dosage form in the pharmaceutical industry because they are cheap to manufacture, chemically and mechanically stable and easy to transport and fairly easy to control dosage. Pharmaceutical tableting operations have been around for decades however the process is still not well understood. One of the common problems faced during the production of pharmaceutical tablets by powder compaction is sticking of powder to the punch face, This is known as 'sticking'. A more specialized case of sticking is picking when the powder is pulled away form the compact in the vicinity of debossed features. In the pharmaceutical industry, picking is solved by trial and error which is an expensive, labor intensive and time consuming affair.

The objective of this work was to develop, validate, and implement a modeling framework for predicting picking in powder compacts. The model was developed in Abaqus$^{\text{TM}}$ a commercially available finite element package. The resulting model was used to investigate the influence of debossed feature geometry viz. the stroke angle and degree of pre-pick, and, influence of lubricant on picking.

An important factor vital to the success of finite element modeling (FEM) used in this work is the constitutive relationship used to model the mechanical response of the powders compact when subjected to external loads. In this work, the modified Drucker-Prager Cap (DPC) constitutive relation was used to model the powder compact. The DPC model parameters were calibrated experimentally. The experimental procedure for measuring the (modified) Drucker-Prager Cap parameters is described in this work.

Additionally, the picking propensity of tablet depends on the adhesive interaction between the powder compact and punch face. An instrumented punch was developed in-house to characterize the adhesive force between a punch face and powder as a part of this work. The influence of the compact solid fraction and blend lubrication on the adhesive interaction was studied. The adhesive traction-displacement data was used as an input for the finite element model.

The picking behavior in the pharmaceutical compact was modeled using a fracture mechanics approach in the FEM model. This model was calibrated using the fracture toughness measurements of the powder. The experimental procedure to determine the fracture toughness using single edge notch bend test and 'inverse FEM'is described.

Experimental validation of the FEM simulation was performed by making tablets with debossed features and imagining the compact using x-ray computed micro tomography (XRCT). The density distribution in the compact and the dimensions of the debossed features in the experimentally produced tablets were compared to the FEM simulations. The post processing algorithms used for the experimental validation of the FEM results have also been discussed in this dissertation.

Lastly, a parametric study was performed to understand the impact of debossed feature dimensions and blend lubrication on picking behavior.

1. INTRODUCTION

1.1 Picking in Pharmaceutical Compacts

Solid oral dosage is the preferred pharmaceutical drug delivery format with over 90% of the drugs developed being administered orally [1]. Tablets and capsules are the two most common types of solid dosage forms. According to Lachman *et al.*, (1986) tablets are cheap and easy to manufacture, mechanically and chemically stable, deliver a drug with a high degree of accuracy and are compact which makes them easy to transport and store. From the patients perspective tablets are very convenient to use which results in improved patient compliance [2].

Powder compaction is a common manufacturing process used in the production of pharmaceutical tablets. In this process, loose powder particles are compressed in a die cavity by the application of pressure to form a solid green part of relatively high density that conforms to the shape of the cavity and the tooling used [3, 4]. A schematic of the tableting process is shown in Figure 1.1. The objective of any powder compaction process is to prepare compacts with desirable mechanical strength, minimal density gradients, shape within specified dimensional tolerances, minimal flaws or cracks and predictable and reproducible disintegration characteristics to ensure drug release to attain adequate bio-availability [5–8]. To achieve this objective, the overall powder compaction process is frequently optimized to specify a formulation, i.e., a mixture of powders, and the tooling and process parameters that result in a desirable compaction performance. In this work, pharmaceutical tablet compaction is the application of interest.

One of the many difficulties faced during the production of pharmaceutical tablets is powder sticking to punch faces during compaction [9]. Sticking occurs when the adhesive stresses between the punch face and powder exceeds the cohesive stresses

| Die Filling | Compression and Decompression | Ejection |

(a)　(b)　(c)　(d)　(e)
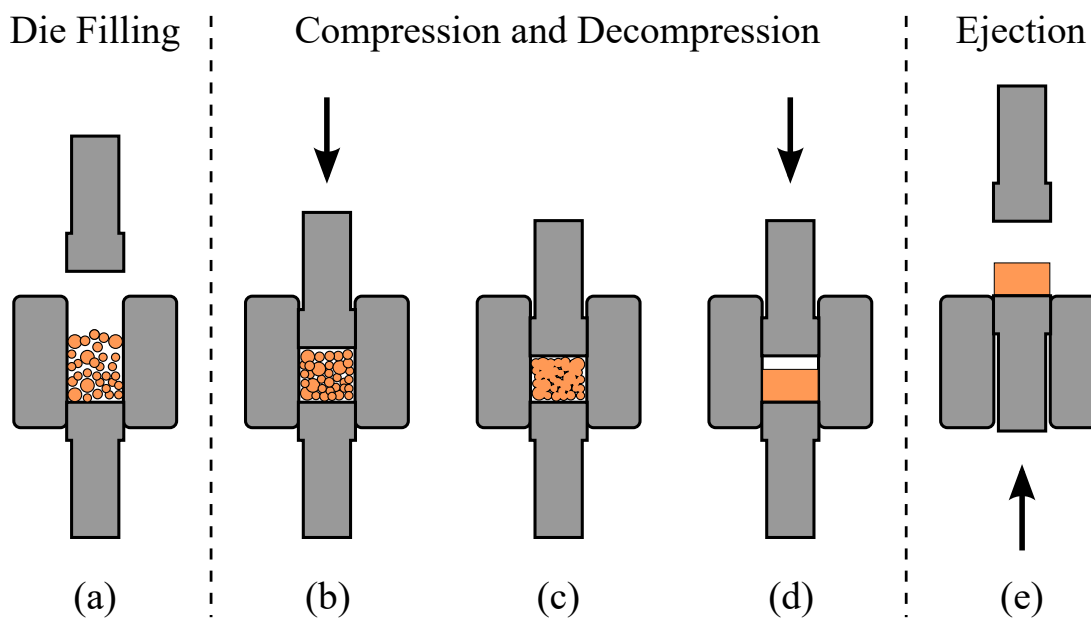
Figure 1.1.　Schematic of the tableting process (a) die filling, (b) particle re-arrangement, (c) particle fragmentation and plastic deformation, (d) decompression, (e) ejection.

within the tablet. In prior studies, it has been shown that the cohesive stresses within the tablet is a function of the tablet formulation and process parameters [9,10]. For a commercial tableting operation in which tablets are formed in rapid succession, picking and sticking can be particularly problematic as powder accumulates on the punch face which is then repeatedly compressed [2]. In a worst case scenario, this compressed powder can damage the tooling and/or the tablet press. Pharmaceutical tablets are frequently formed with debossed surface features (Figure 1.2) in order to identify the product, detect counterfeit and in some cases to facilitate tablet splitting with scoring line/lines [11,12]. Debossing is one of the preferred methods for imprinting tablets as debossing can be easily incorporated into the manufacturing process by embossing the punches used to create the tablets. In addition to sticking, powder-punch adhesion can also lead to picking. Picking which is a special case of sticking occurs when powder is pulled away from the powder compact in the vicinity of debossed features on the tablet face such as letters, numbers, symbols, and scoring lines. Picking and

sticking leads to poor tablet quality and incomplete or missing identification features on the tablets, potentially leading to rejection of those tablets [12]. The only way to reduce picking and sticking problems is to periodically clean the tablet press tooling after a set number of compaction cycles before the tableting process can be resumed. This process is both time consuming and expensive.

Figure 1.2. An example of debossed features on tablets used to detect counterfeiting.

In most cases, picking and sticking problems are addressed using a trial and error approach. However, these methods fail to capture the physics of the entire powder compaction process such as influence of tool geometry, compression, decompression and ejection. With the Food and Drug Administration (FDA) advocating Process Analytical Technology (PAT) and Quality by Design (QbD) initiatives to better understand the design and control of pharmaceutical manufacturing processes, there is

a need to develop and apply predictive tools that can accurately describe the powder motion, stresses, and densification and provide an in-depth understanding of the powder compaction process. One approach that has been particularly effective in predicting these quantities is the finite element method (FEM) [13–16].

The FEM algorithm consists of dividing the powder into a number of continuously distributed elements and prescribing application-specific dynamic and/or kinematic boundary conditions [17]. The resulting element stresses and deformations (strains) are then numerically computed using an appropriate phenomenological constitutive relation subject to the constraints of linear momentum, conservation of mass, conservation of energy and kinematic comparability. The success of any FEM model depends on the constitutive model used to describe the deformation behavior of the powder and the interaction properties used to describe powder-tooling interaction and process parameters used in the simulation. At present, there are no constitutive models based on first principle to capture the effect of particle shape, size, packing and inter-particle interaction to describe the deformation behavior of particulate systems. The lack of a constitutive model is mainly due to poor understanding of all the effects of particulate level process on the bulk level constitutive response of the powder [5]. Thus, current FEM approaches use a phenomenological model to capture the constitutive response of the powder at a macroscopic level. The Drucker-Prager Cap model is one such model. Application of this algorithm to simulate powder roll compaction [13, 14, 18–21] and tablet compaction [22–25] has been implemented successfully to investigate the influence of formulation and process parameters.

However, in our study we found that a constitutive model which captures the deformation mechanics of the powder bed alone is insufficient to describe the initiation and propagation of cracks in the powder compact which we hypothesize results in picking and sticking of the powder compact. This requires additional detailed modeling of the interaction behavior between the punches and dies (collectively known as tooling) and, the powder bed undergoing compaction. Additionally, a separate model is needed to describe the the growth of cracks in the powder compact during

the decompression or relaxation phase of the compaction process. Thus, in this work a computational framework using FEM was developed to study picking in pharmaceutical powder compacts.

The success of a phenomenological constitutive model is heavily dependent on the material calibration experiments used to capture the mechanical response of the powder bed [26, 27]. Thus the model calibration protocol is discussed in depth in this dissertation. In this framework, the modified-DPC model was used to to model the powder as a continuum, an adhesive traction separation law was used to model the interaction between the powder compact and tooling and, finally a cohesion zone modeling approach based on fracture mechanics was used to model the initiation and growth of cracks in the powder compact during the decompression phase. In this dissertation an attempt was made to use the FEM modeling technique to quantitatively predict the post-compaction geometric dimensions and local solid fraction in the vicinity of debossed surface features on the tablet which I hypothesize is key to predicting picking. The results of the FEM simulation were validated experimentally using X-ray computed tomography (XRCT) and image-processing. In addition, a parametric studies was performed to investigate what elements of the embossed geometry increase or decrease the likelihood of picking. Specific thesis objectives and goals are stated in Section 2.2. The outcome of this study provided incite into the factors that cause picking in pharmaceutical tablets. The findings of this work can be used to better design formulation and powder compaction tooling.

1.2   Organization of Thesis

In Chapter 2 the approaches used to quatify and/or reduce picking in prior studies is presented. Additionally, the specific research goals and objectives are explicitly listed. Individual objectives of the thesis are addressed in Chapters 3 through 7. The theory and calibration of the DPC model parameters is presented in Chapter 3. In Chapter 4 a detailed description of the apparatus used to measure the powder punch

face adhesion and the methodology used for the adhesion measurement is presented. In Chapter 5 the protocol to measure the fracture toughness of the powder compact is discussed. The fracture toughness was used to model the crack initiation and propagation process in the compact. The FEM modeling framework used in this study is described in Chapter 6. To validate the FEM simulations experimentally compacts with debossed features were made and imaged using x-ray computed micro tomography (XRCT). The methodology to measure the density distribution within the debossed compact and The specific dimensions of the debossed features on the compact measured by image processing of the XRCT images is discussed in Chapter 7. The results of the FEM parametric study and experimental validation of the FEM simulations are presented in Chapter 8. Finally, concluding remarks are provided in Chapter 9 and recommendations for future work are suggested in Chapter 10.

2. BACKGROUND AND APPROACH

In this chapter the techniques used in prior studies by other researchers to quantify and/or reduce picking and sticking in pharmaceutical compacts is presented. Additionally, the thesis objectives are listed.

2.1   Picking Literature

The Tablet Specification Manual of the American Pharmaceutical Association [28] provides recommendations, presumably found through experience, to reduce some of the problems associated with tablet debossing. These include keeping the stroke angle, i.e., the angle of the debossed valley walls with respect to the vertical, within a specified range, making the area of confined features, such as the interior regions of an "A"or "8"as large as possible, and avoiding sharp corners, such as those found on the letters "W"and "Y". A commonly used qualitative assessment tool that is used in the pharmaceutical industry to evaluate the propensity of a formulation to pick, is an embossed punch with a combination of letters and numbers like 'A6W8' (Figure 2.1) which are anecdotally know to cause problems and produce a batch of debossed compacts. If a predefined number of tablets in the batch exhibit picking the formulation is rejected.

There are very few prior studies that have examined picking . However, many researchers have examined sticking (picking is a subset of sticking) , which is when material adheres to the punch away from debossed features. From prior studies the key factors that lead to picking and sticking on pharmaceutical powder compacts are:

- poorly designed tooling leading to stress concentrations at concave debossed features such as interior corners and valleys [29–31],

Figure 2.1. An embossed punch with the letters 'A6W8' commonly used as a qualitative assessment tool to evaluate the propensity of a formulation to pick and stick in the pharmaceutical industry.

- selection of tooling material, punch-tip coatings and surface roughness [32–36] and

- formulation properties and tabletting process parameters [37–42].

2.1.1 Literature Focused on Tooling Design

Waimer *et al.* [29] investigated the influence of engraving features using small conical debossing shear cones on the punchs surface (Figure 2.2). This study showed that the shear cones on the punch face modified the shear stress distribution within the tablet. Increasing the shear cone angle ϵ, corresponding to decreasing the stroke angle, resulted in decreasing adhesion forces.

Roberts *et al.* [30] investigated the influence of punch tip geometry and embossment on sticking for a lactose-ibuprofen formulation. The study showed that increasing the concavity of the punch from flat face to a concave punch increased sticking. Increasing the punch diameter from 10 mm to 12 mm did not significantly impact
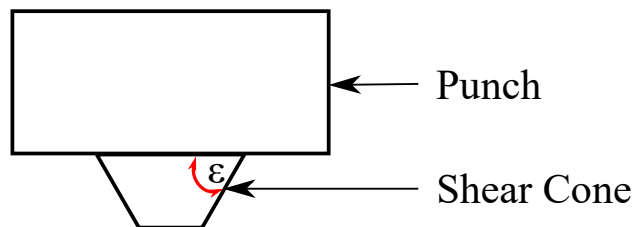
Figure 2.2. Schematic of a shear cone used by Waimer et al. [29]. The angle of the shear cone is ϵ.

sticking behavior. However, the presence of punch embossment significantly increased the sticking. The author hypothesized that the increase in sticking could be due to increase in shear force at the lateral face of the embossment (stress concentration).

Laity [31] studied the effect of embossed punch features on the compaction behavior of micro-crystalline cellulose (MCC). Cylindrical compacts were produced with single and double furrows Figure 2.3 across the compacts top face. Using a small angle x-ray scattering technique, this study demonstrated that large changes in relative density occur in the vicinity of the furrows (debossed feature), with smaller relative densities near the furrows flanks and larger relative densities at the furrow base. In addition, smaller density regions around the furrows were prone to cracking and flaking, especially in the region between the double furrows.

2.1.2 Literature Focused on Tooling Material and Punch Tip Coating

Tsiftsoglou and Mendes [35] found that boron alloy coated tools required smaller ejection forces and, consequently, sticking propensity to the tooling was reduced for ibuprofen tablets. However Shah *et al.* [43] reported that boron-alloy coating increased ejection and adhesion forces for acetaminophen tablets [43]. A study by Schumann and Searle [36] concluded that chromium nitrite ion bombardment treat-
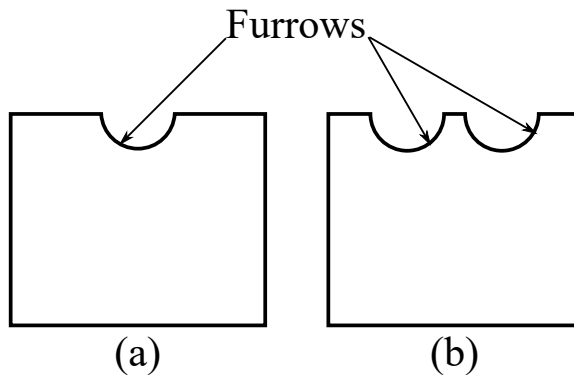
Figure 2.3. Schematic of the cylindrical MCC compacts produced by Laity [31]. (a) A compact with a single furrow across the compacts top face. (b) A compact with a double furrow.

ment of the punch surface eliminated sticking behavior but chrome electro-plating of the tools did not cause any noticeable change in sticking behavior over uncoated tools for ibuprofen tablets. Roberts *et al.* [44] showed that chrome plating the punch tip did not alleviate picking and sticking problems and smoother tooling surfaces did not necessarily correspond to a reduction in sticking. In contrast, Pedersen *et al.* [45] found that chrome plating of tooling surfaces decreased sticking behavior for acetaminophen tablets. To summarize, there is no clear consensus on the effectiveness of punch tip coatings in literature. The efficacy of punch-tip coating should be evaluated on a case to case basis based on the formulation and process parameters.

2.1.3 Literature Focused on Formulation Properties and Tableting Process Parameters

Mullarney *et al.* [46] and Strickland *et al.* [37] showed that addition of magnesium stearate to most formulation in limited quantities ($< 1\%$) reduced sticking behavior. However Mullarney *et al.* noted that, addition of magnesium stearate to a formulation containing ibuprofen exacerbated sticking. Addition of magnesium stearate is also know to cause other tableting problems like capping and edge chipping due

Figure 2.4. Compaction tooling with titanium and tungsten carbide punch tip coating.

to poor mechanical strength of the resulting tablet [47–49]. Increasing the active pharmaceutical ingredient (API) percentage worsened sticking behavior.

Mullarney *et al.*, Waimer *et al.* [9] and Wang *et al.* [39] noted that increasing the compaction force increased the propensity to stick for very cohesive powders [50] like sorbitrol, ibuprofen (IBU) and acetaminophen. However Roberts *et al.* [32] reported that increasing the compression force decreases sticking propensity for acetylsalicylic acid (ASA) and ibuprofen while increasing the compression force increased sticking propensity for lactose.

Goodhart *et al.* [51] studied the effect of granulation on sticking. They reported that the sticking propensity was lower for granulated mannitol produced by spray dried granulation in comparison to powdered mannitol.

It should be noted that prior studies have tried to correlate many other parameters with sticking like ejection force, moisture content, punch surface hydrophobicity, residual wall stress, temperature, etc. It can be argued that some of the results obtained is an artifact of the evaluation technique used to quantify sticking. A detailed discussion of some of the methods used by researchers in the past to quantify sticking is presented in Chapter 4.

2.2   Research Goal and Objectives

The goal of the proposed thesis work is to develop a better understanding of picking on pharmaceutical powder compacts so as to develop a predictive tool to minimize this problem.The specific objectives of the proposed research are:

1. Develop FEM computational models for predicting if picking will occur during tableting. Picking is assumed to occur if the adhesive load between the powder and a boundary on an FEM element is greater than the cohesive load between neighboring elements.

2. Develop image processing algorithms for measuring various features of debossed tablets produced in FEM simulations and experiments. These features include stroke angle, stroke depth, debossed volume, and relative density field. The images for experimental tablets will be generated using x-ray micro computed tomography (XRCT).

3. Validate the FEM model by comparing the geometric and relative density features in a debossed tablet to XRCT measurements of a tablet produced in experiments under the same conditions. The image processing algorithms described in Objective 2 will be used.

4. Develop an experimental technique to measure adhesion properties between a powder and a punch surface.

5. Develop an experimental technique to measure the fracture toughness of the compact.

6. Incorporate an adhesion and cohesion model in the FEM/DPC framework. The properties from Objective 4 and 5 respectively will be used in the model.

7. Validate the computational model developed in Objective 6 against experimental measurements using the same techniques as described in Objectives 2 and Objective 3.

8. Perform a parametric study to examine the influence of debossed feature parameters (stroke depth, stroke angle, and pre-pick) and formulation properties on the propensity to pick.

3. DRUCKER-PRAGER CAP CONSTITUTIVE MODEL

3.1 Introduction

Fundamental to the FEM method is the constitutive model relating the applied traction to the resulting stress and strain (and/or strain rates) for the material being modeled. In this chapter the modified DPC model is described in detail. Additionally the experimental procedures used to determine the model parameters are also presented.

3.2 Background

The continuum approach to model tablet compaction has been adopted from soil mechanics. A number of critical state models have been proposed to describe the densification behavior of powder, such as those proposed by Drucker [52], Schofield [53], Green [54], DiMaggio and Sandler [55], and Gurson [56]. The term "critical state" refers to the response of the material while it is yielding. These early models included a elliptical cap i.e. a critical state model governed yielding and plastic flow due to material densification. The Drucker-Prager Cap (DPC) model [57,58] improved upon these prior models by including shearing behavior in addition to elliptical cap to capture the material behavior in the decompression and ejection phase. A further improvement to the DPC model, known as the modified-DPC model, includes the dependence of the DPC yielding behavior on the powders instantaneous solid fraction [20].

3.2.1 Description of the Modified-Drucker-Prager/Cap (DPC) Model

A constitutive model that is used to define the behavior of an elastic-plastic material has three major aspects:

- a yielding criterion,

- a flow rule and

- a hardening criteria

The hardening crietia describes the evolution of the cap (work hardening) as a function of the volumetric plastic strain. In the case of an isotropic material this definition can be simplified using stress invariants.The DPC models yield functions and flow rules are functions of two stress invariants: the hydrostatic stress, p, and the Mises equivalent stress, q. The hydrostatic stress is defined as the trace of the stress tensor σ_{ij},

$$p = -\frac{1}{3}\sigma_{ii} \ . \tag{3.1}$$

The Mises equivalent stress is proportional to the magnitude of the inner product of the deviatoric stress tensor, $S_{ij} = \sigma_{ij} - p\delta_{ij}$, where the quantity δ_{ij} is the Dirac delta operator,

$$q = \sqrt{\frac{3}{2}S_{ij}S_{ij}} \ . \tag{3.2}$$

The DPC models yield functions appear as three curves in the p-q plane: a shear line F_s, an elliptical cap F_c, and a transition curve F_t. Each of these curves is described in the following paragraphs and are depicted graphically in Figure 3.1.

The shear yield line is described by the powder compacts cohesion d and internal friction angle β according to the relation,

$$F_s(p,q) = q - p\tan\beta - d = 0 \ . \tag{3.3}$$

An applied stress state located below the line results in only elastic distortion of the powder compact. A stress state located on the shear yield line indicates volumetric dilation and fracture of the powder compact. Note that for the modified-DPC model, the values for d and β may change, depending on the powder compacts instantaneous solid fraction. The elliptical cap F_c is given in the DPC model as,

$$F_c(p,q) = \left[(p - p_a)^2 + \left(\frac{Rq}{1 + \alpha + \alpha/\cos\beta} \right)^2 \right]^{1/2} - R(d + p_a\tan\beta) = 0 \ , \tag{3.4}$$
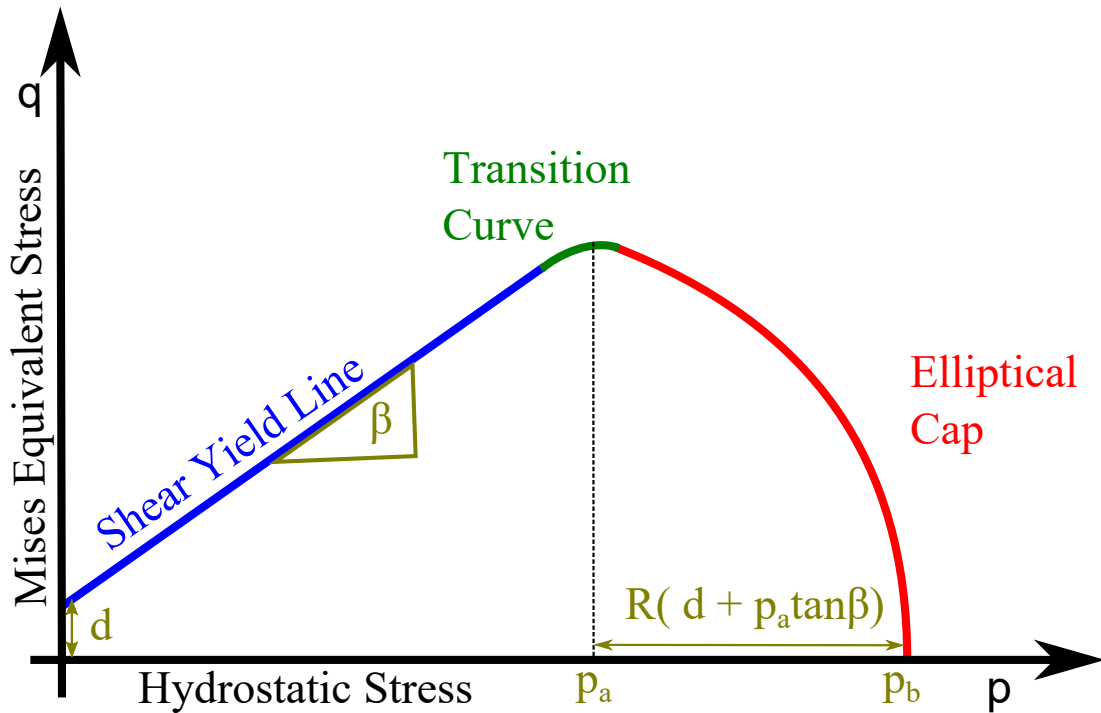
Figure 3.1. A plot illustrating the DPC yield envelopes at a fixed solid fraction. Note that for the modified-DPC model, yield envelopes can shift for each solid fraction.

where p_a is known as the stress evolution parameter, R is the eccentricity, or aspect ratio, of the elliptical cap, and α $(0.05 \leq \alpha \leq 0.1)$ is a constant used to smoothly transition between the cap and the transition curve, which is discussed in the following paragraph. A stress state falling on the cap represents densification of the powder.

The transition curve F_t is included in numerical implementations of the DPC model in order to provide numerical stability when stress states transition between the cap and shear envelopes. This transition curve is given by,

$$F_t(p,q) = \left\{ (p - p_a)^2 + \left[q - \left(1 - \frac{\alpha}{\cos \beta} \right) (d + p_a \tan \beta)^2 \right] \right\}^{1/2}$$
$$ - \alpha \, (d + p_a \tan \beta) = 0 \; . \tag{3.5}$$

The curves F_s, F_c, and F_t only identify when yielding of the material occurs; they do not provide information on the powders resulting deformation. This information is described in terms of material (differential) strains,

$$d\varepsilon_{ij} = d\varepsilon_{ij}^e + d\varepsilon_{ij}^p \; , \tag{3.6}$$

where ϵ_{ij} is the total strain, ϵ_{ij}^e is the (recoverable) elastic strain, and ϵ_{ij}^p is the (unrecoverable) plastic strain. The elastic strain is given by,

$$d\varepsilon_{ij}^e = \frac{(1-\nu)}{E} d\sigma_{ij} - \frac{\nu}{E} d\sigma_{kk} \delta_{ij} \tag{3.7}$$

where linearly elastic, isotropic material behavior is assumed, with E and ν being the materials elastic modulus and Poissons ratio, respectively.

The plastic strain is calculated using a plastic potential g, defined such that,

$$d\varepsilon_{ij}^p = d\lambda \frac{\partial g}{\partial \sigma_{ij}} \; , \tag{3.8}$$

where, $d\lambda$ is a stress increment dependent positive scalar [59]. In the DPC model, it is assumed and shown experimentally by Sinka et al. [60, 60] that a normality condition holds on the cap and transition yield curves, known as associated flow, such that at the cap curve,

$$g = F_c(p, q) \; , \tag{3.9}$$

and at the transition curve,

$$g = F_t(p, q) \; , \tag{3.10}$$

The associated flow rule relates the radial and axial strains and stresses during tablet compaction to the slope of the elliptical cap in Figure 3.1. On the shearing line, however, the flow is assumed to be non-associative ($g \neq F_s(p, q)$). On this line the plastic potential is given by,

$$g = \left\{ [(p - p_a) \tan \beta]^2 + q^2 \right\}^{1/2} \; . \tag{3.11}$$

The strains on the shear yield line use this plastic flow potential in conjunction with Equation 3.8. Equations 3.3 - 3.7 show that use of the DPC model requires knowledge

of seven parameters: d, β, p_a, R, α, E, and ν. The transition constant is typically set arbitrarily to a value in the range $0.05 \leq \alpha \leq 0.1$ so that the numerical computations are stable. Thus, there are actually only six parameters that must be determined through material characterization experiments. For the modified-DPC model, these six parameters must be determined as a function of the solid fraction. The following section provides the theoretical foundation for how the six parameters are determined from three independent tests, each performed as a function of powder compact solid fraction.

3.3   Materials

The modified DPC parameters for two powder formulations were characterized in the current work. The compositions of these formulations are provided in Table 3.1. These particular formulations were chosen based on the recommendation of the projects industrial sponsor. The formulation without magnesium stearate (MgSt) is anticipated to result in a larger degree of picking as compared to the one with magnesium stearate.

3.4   Experimental Calibration of Modified-DPC Material Parameter

The mechanical tests used to determine DPC parameters were performed on cylindrical compacts produced using a uniaxial punch and die system installed on a universal material testing machine (MTS model C43.504). A computer-aided design (CAD) model of the system is shown in Figure 3.2(a). A 10 mm diameter, 22.2 mm tall die was used with flat-faced upper and lower punches. The lower punch remained fixed throughout the experiments. Load cells (MTS model 661.20F-03; Interface model LBM-50K) were mounted on the punches to record upper and lower uniaxial compression forces. A servo encoder on the MTS measured the upper punch's axial displacement. A piezoelectric pressure sensor (Kistler, model 6183) was installed radially in the die so that its tip made direct contact with the powder in order to measure

Table 3.1.   The powder formulations characterized and modeled in the present work.

Components	Brand Name (Manufacturer)	Composition (% w/w)	
		Blend w/o MgSt	Blend w MgSt
Microcrystalline cellulose	Avicel PH200 (FMC Corp.)	62.16	61.54
Mannitol	Pearlitol SD 200 (Roquette Pharma.)	31.08	30.77
Croscarmellose sodium	Carboxymethylcellulose Sodium Type A (DFE Pharma.)	6.76	6.69
Magnesium stearate	Magnesium Stearate Vegetable Source (Bioconvergence LLC.)	0	1

the radial stress during compression of the compacts. The lower punch location was adjusted so the pressure sensor was located approximately at the mid-height of the compacts at maximum compression (Figure 3.2(b)). The die walls and punch faces were coated with a thin layer of magnesium stearate prior to all compact manufacturing and testing steps in order to approximate frictionless boundary surfaces. This coating was produced by compressing and discarding a slug of magnesium stearate before every compaction run. All compacts were produced at a loading and unloading strain rate of approximately 5 mm/min in order to maintain quasi-static loading conditions. The dwell time was zero in all cases. The MTS TestWorks^{TM} software and an NI BNC-2110 data acquisition board were used to acquire sensor data at a rate of 1000 Hz. Changes in relative humidity have been shown to have an influence on powder properties [61, 62]. The measurements performed in these studies were performed in typical room conditions. Measurements of the room temperature
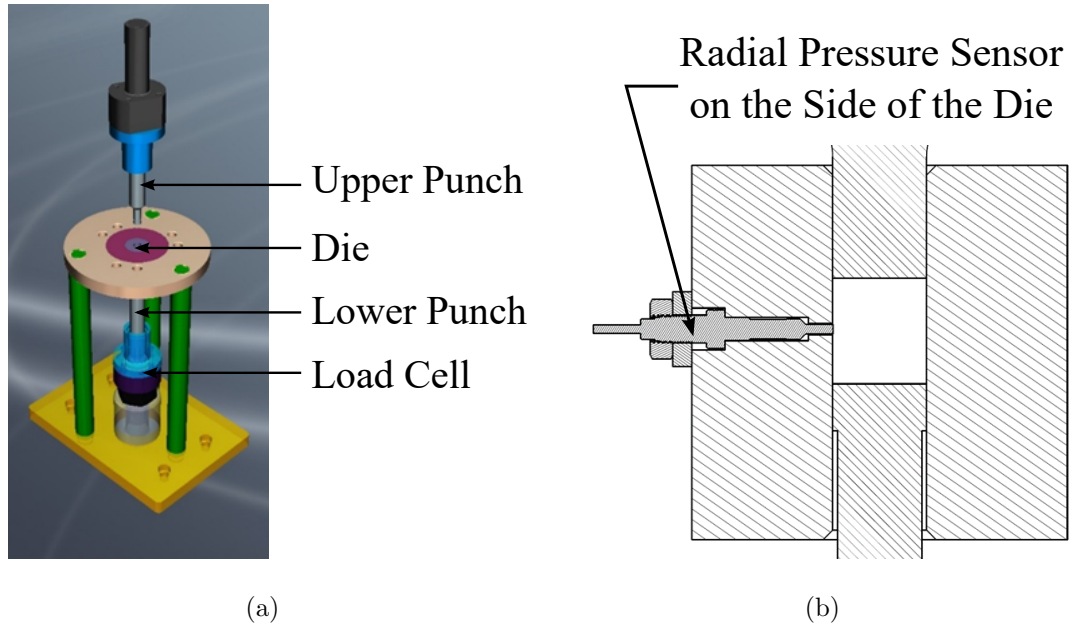
Figure 3.2. (a) A schematic of the punch and die system used to create and test powder compacts used for material characterization. (b) A schematic showing the location of the radial pressure sensor.

showed that it varied by 5.2 °C (17.6 °C to 22.8 °C) while the relative humidity varied by 14% (45% RH to 59% RH). The influence of humidity on powder properties is very powder specific. For both mannitol and microcrystalline cellulose, increasing the moisture content in the powder increases the cohesion and friction angle of the powders [63, 64].

Determination of the six DPC parameters at a single solid fraction involved three tests. The first two were used to measure a compacts strength, from which the shear yield parameters d (cohesion) and β (internal friction angle) were obtained. The third test was a confined uniaxial compression test, in which the axial and radial stresses were measured as a function of axial strain during both compression and decompression of the powder. Data obtained from this third test were used to obtain the elliptical cap surface parameters R (cap eccentricity) and p_a (stress evolution parameter), as well as the elastic parameters E (elastic modulus) and ν (Poissons ratio). Since the modified DPC model parameters vary with the solid fraction, the three tests

were performed over the range of relative densities expected in the FEM simulations, which in the present case ranges from 0.3 to 0.95. The theory and procedures for calculating these parameters from measured data are described in the following paragraphs. The shear line parameters d and β at a given solid fraction were found using

(a)   (b)
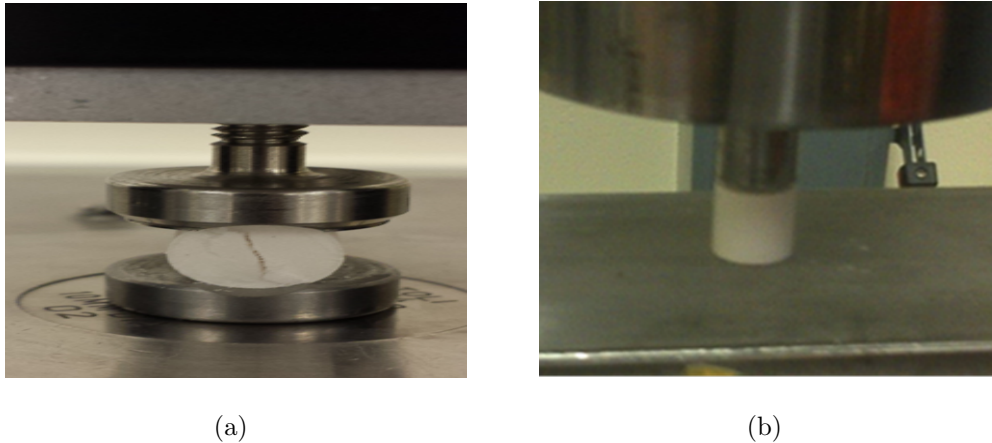
Figure 3.3. Photographs from (a) a diametrical compression failure test for a $D/h > 1$ compact, and (b) a uniaxial compression failure test for a $D/h < 1$ compact.

a method adapted from Procopio [65]. Two cylindrical compacts at the same post-ejection solid fraction were produced. The two compacts had different aspect ratios: $D/h > 1$ and $D/h < 1$, where D was the compact diameter and h was its height. In the present work, 1100 mg of powder was used to produce a large aspect ratio compact while 250 mg of powder was used to create a smaller aspect ratio compact. Both compacts were loaded until failure, with the $D/h > 1$ compact loaded uniaxially and the $D/h < 1$ compact loaded diametrically using curved platens (Figure 3.4). The loading rate during these compact failure tests was maintained at 5 mm/min, identical to the rate used to create the compacts. Because the aspect ratios of the compacts vary, there is the potential for bias in the measurements. However, care was taken to ensure the uniaxial test sample aspect ratios were greater than one and the aspect ratios for the diametrical test samples were less than one, as assumed in the theoretical analysis models. Note that these loading tests were performed soon after

the creation of the compact in order to avoid significant post-compaction changes in compact solid fraction due to creep. Caliper measurements of the compact dimensions showed that little post-compaction deformation occurred between compact creation and failure testing.

For uniaxial compression, given by the subscript "u", the hydrostatic stress p_u and Mises stress q_u at failure are,

$$p_u = \tfrac{1}{3}\sigma_u \, , \tag{3.12}$$

$$q_u = -\sigma_u \, , \tag{3.13}$$

where,

$$\sigma_u = \frac{4F_u}{\pi D^2} \, . \tag{3.14}$$

is the stress in the uniaxial direction. The parameter F_u is the uniaxial load at failure. For the diametrical loading case, given by the subscript "d", the stress state is a modified Hertz solution for curved anvils proposed by Awaji and Sato [66],

$$p_d = \tfrac{2}{3}\sigma_d \, , \tag{3.15}$$

$$q_d = \sqrt{13}\sigma_d \, , \tag{3.16}$$

assuming $D/h > 1$, where,

$$\sigma_d = \left\{ 1 - 1.15\left(\frac{b}{R}\right)^2 + 0.22\left(\frac{b}{R}\right)^3 \right\} \frac{2F_d}{\pi Dt} \, . \tag{3.17}$$

is the stress at the failure location (at the tablets center). The parameter F_d is the applied diametrical force at failure, t is the compact thickness, b is the contact half width, and R is the radius of the anvils.

As shown in Procopio [65], both (p_u, q_u) and (p_d, q_d) lie on the shear yield line. Using these parameters, the powder cohesion d and internal friction angle β can be expressed as,

$$d = \frac{\sigma_u \sigma_d \left(\sqrt{13} - 2\right)}{\sigma_u - 2\sigma_d} \, , \tag{3.18}$$

and,

$$\beta = \tan^{-1}\left[\frac{3\left(\sigma_u - d\right)}{\sigma_u}\right] \, . \tag{3.19}$$

Note that although uniaxial and diametrical compression tests were performed in the current work, other tests could also have been used to provide the shear yield line parameters. For example, the cohesion and internal friction angle could have been determined using simple tension or pure shear tests. The uniaxial and diametrical compression tests were used here due to their simplicity and equipment availability.

The elliptical cap hardening parameters p_a and R were found using a confined uniaxial compression test, signified using a subscript "c". This test was performed with the powder located within the die. In contrast to the compact failure tests, the confined uniaxial tests were performed with varying amounts of powder so that the distance between the punches at maximum compression was $h = 7.5$ mm, regardless of the powders solid fraction. The mass of powder, m, for a target solid fraction of η is,

$$m = \eta \rho_{\text{true}} \frac{\pi D^2}{4} h \ , \tag{3.20}$$

where 'ρ_{true}' is the true density of powder. The true density, which is the chemical density of the material, was assumed to equal the powders apparent density, which includes the volume of inaccessible pores within particles. The apparent densities of the blends with and without magnesium stearate were measured via helium pycnometry (Micromeritics AccuPyc II 1340, n = 10 measurements each) and found to be 1.553 ± 0.005 and 1.529 ± 0.008 g/cm^3 respectively. In comparison, the calculated true densities were found to be 1.535 (with MgSt) and 1.542 (without Mgst), respectively. The true density values are closer to each other and in the opposite rank order as compared to the measured values. However, additional investigation also revealed a significant difference in moisture contents of the two blends (2.97-3.21% and 7.21-9.45% for with and without blends, respectively). The apparent density was used for the calculations in this work since this measurement includes any moisture that may have been absorbed during storage of the materials.

Assuming frictionless die walls, which are approximated in practice by applying magnesium stearate to the die walls prior to testing, measurements were made of

the radial $\sigma_{r,c}$ and axial $\sigma_{z,c}$ stresses at the instant when the powder densified to the target solid fraction η. The corresponding hydrostatic and Mises stresses are,

$$p_c = -\frac{1}{3}\left(\sigma_{z,c} + 2\sigma_{r,c}\right) \ , \tag{3.21}$$

and,

$$q_c = \left|\sigma_{z,c} - \sigma_{r,c}\right| \ . \tag{3.22}$$

Furthermore, assuming that the die perfectly rigid, i.e., there is no elastic or plastic deformation in the radial direction,

$$d\varepsilon_{ij}^p\big|_c = d\lambda \left.\frac{\partial g}{\partial \sigma_r}\right|_c = 0 \ . \tag{3.23}$$

Substituting Equation (3.4) into Equation (3.23) yields,

$$R = \sqrt{\frac{2}{3q}\left(p_c - p_a\right)} \ . \tag{3.24}$$

Substituting Equation (3.24) into Equation (3.5) gives a closed form solution for p_a,

$$p_a = \frac{-3q_c - 4d\tan\left(\beta\right)}{4(\tan\left(\beta\right))^2} + \frac{\sqrt{9q_c^2 + 24d(\tan\left(\beta\right))^2 p_c q_c + 16(\tan\left(\beta\right))^2 q_c^2}}{4(\tan\left(\beta\right))^2} \ . \tag{3.25}$$

With the stress evolution parameter p_a and cap eccentricity R known, the hydrostatic yield stress (p_b in Figure 3.1) can also be computed,

$$p_b = p_a\left(1 + R\tan\beta\right) + Rd \ . \tag{3.26}$$

It is often of interest to report p_b as a function of the plastic volumetric strain ϵ_{vol}^p since this relation is used in ABAQUS for calculation of the current stress state. In turn, the plastic volumetric strain may be related to the powders solid fraction according to the relation proposed by Gurson [56],

$$\eta = \eta_0 \exp\left(-\varepsilon_{vol}^p\right) \ , \tag{3.27}$$

where n_0 is the materials solid fraction that corresponds to zero volumetric plastic strain. The solid fraction at zero volumetric plastic strain is typically taken as the

(a) Uniaxial Breakage Test.

(b) Diametrical Breakage Test.
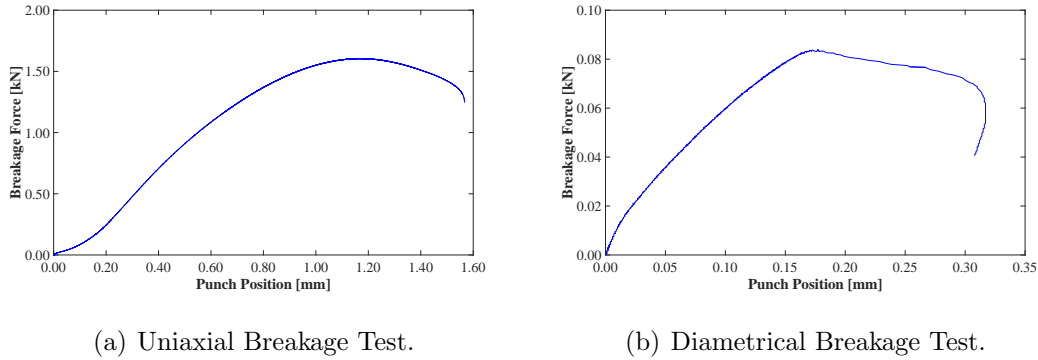
Figure 3.4. Typical data from the breakage test. The peak value of the force was used to determine the uniaxial and diametrical breakage stress.

powders poured bulk solid fraction [20]. The remaining DPC parameters are elastic parameters that can be determined from the materials elastic recovery during the decompression phase of the confined uniaxial compression test. Assuming a rigid die and isotropic, homogeneous behavior, the generalized Hookes law reduces to the following closed form solutions for the Poisson's ratio, ν, and Young's modulus, E,

$$v = \frac{\frac{d\sigma_{rr}}{d\varepsilon_{zz}^e}}{\frac{d\sigma_{rr}}{d\varepsilon_{zz}^e} + \frac{d\sigma_{zz}}{d\varepsilon_{zz}^e}} \ , \tag{3.28}$$

$$E = \frac{d\sigma_{zz}}{d\varepsilon_{zz}^e} - 2v\frac{d\sigma_{rr}}{d\varepsilon_{zz}^e} \ . \tag{3.29}$$

In Equaion (3.28) and Equation (3.29), $d\sigma_{rr}/d\epsilon_{zz}^e$ and $d\sigma_{zz}/d\epsilon_{zz}^e$ are the slopes of the stress-axial strain curves in the radial and axial directions, respectively, during the materials elastic recovery. Since the DPC model parameters vary with the powder density, the three previously described tests were performed at different solid fraction in order to fully describe the compaction behavior of the powder. The next few paragraphs discuss how to post process the stress and strain data to obtain the DPC parameters. Typical results from the uniaxial and diametrical loading tests are shown in Figure 3.4(a) and Figure 3.4(b) respectively. Here, the force measured by the MTS Criterion™ load cell was plotted against the instruments upper punch position.

Initially, prior to the upper punch making contact with the compact, the measured force was zero. Upon contact with the compact, an increase in measured force was observed. The force continually increases until a maximum is reached, beyond which a decrease was observed, indicating failure of the powder compact. The maximum force values reported in the uniaxial and diametrical loading test were used in the calculation of cohesion and friction angle. Typical data from the die compaction
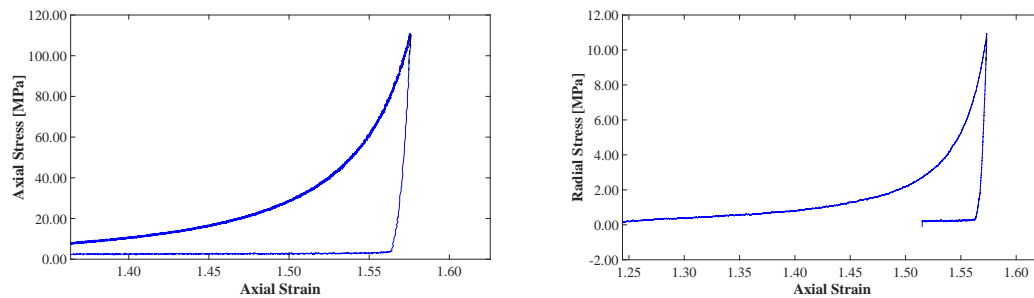
(a) Axial stress as a function of axial strain.   (b) Radial stress as a function of axial strain.

Figure 3.5. Typical data from a compression test. The portion of the data used in the calculation of 'E' and 'ν' is highlighted with a black dashed line.

test are shown in Figure 3.5(a) and Figure 3.5(b). In Figure 3.5(a), the force during compaction was obtained by averaging the force recorded by the load cell on the upper and lower punches was converted to axial stress and plotted against the axial strain. In Figure 3.5(b), the radial stress was measured by the radial pressure sensor is plotted against the axial strain. The axial strain is computed from the punch displacement data knowing the initial fill height of the powder. The slope of the unloading curves from Figure 3.5(a) and Figure 3.5(b) are used to compute the elastic modulus E and Poissons ratio ν. The elastic modulus and Poissons ratio should be evaluated at the onset of unloading before the upper and lower punch lose contact with the compact. The influence of the sampling region on the elastic parameters has been discussed by Han *et al.* [67]. Note that the slopes vary during unloading [67], so it is critical to ensure that only the linear part of the unloading slope is used in the calculation of

the elastic parameters. In this work only the first 1000 points of an unloading curve were used to calculate these slopes, corresponding to a punch displacement of 83 μm. These points have been highlighted in black in Figure 3.5(a) and Figure 3.5(b).

3.5   Results

The modified DPC parameters for two powder formulations were characterized in the current work. The compositions of these formulations are provided in Table 3.1. The modified DPC material parameters for the formulations were measured using the procedures described in Section 3.4. The six DPC parameters are plotted in Figure 3.5 as functions of the solid fraction. Because the largest component by weight in the blends is Avicel PH200, DPC parameters measured for pure Avicel PH200 are included in the plots as a point of comparison. Note that modified DPC parameters for Avicel PH102 have been reported previously in the literature [20, 68] and have quantitative values similar to the Avicel PH200 values tested here.

The difference in the with- and without-MgSt formulation mechanical properties is typical of blends with small amounts of lubrication as reported in the literature [69,70]. The blend with magnesium stearate has larger cohesion, but both blends have similar elastic stiffness. Usually the addition of a lubricant results in decreased compact strength [40, 49, 71]. Thus, additional measurements were performed on both blends to verify the observed trends. Further discussion on these trends is presented in the conclusions section. Blends with large cohesion have been reported to have larger strength [72]. An internal friction angle of 70 degrees is consistent with the behavior of pharmaceutical and metal powders [58, 67]. The hydrostatic yield strength for the blend without MgSt is slightly larger than the one with MgSt, which means that a larger punch force would be necessary to compact the without-blend to a given relative density as compared to the blend with MgSt [72]. The addition of a lubricant facilitates particle re-arrangement during compaction and thus a larger relative density is achieved at a smaller punch force.
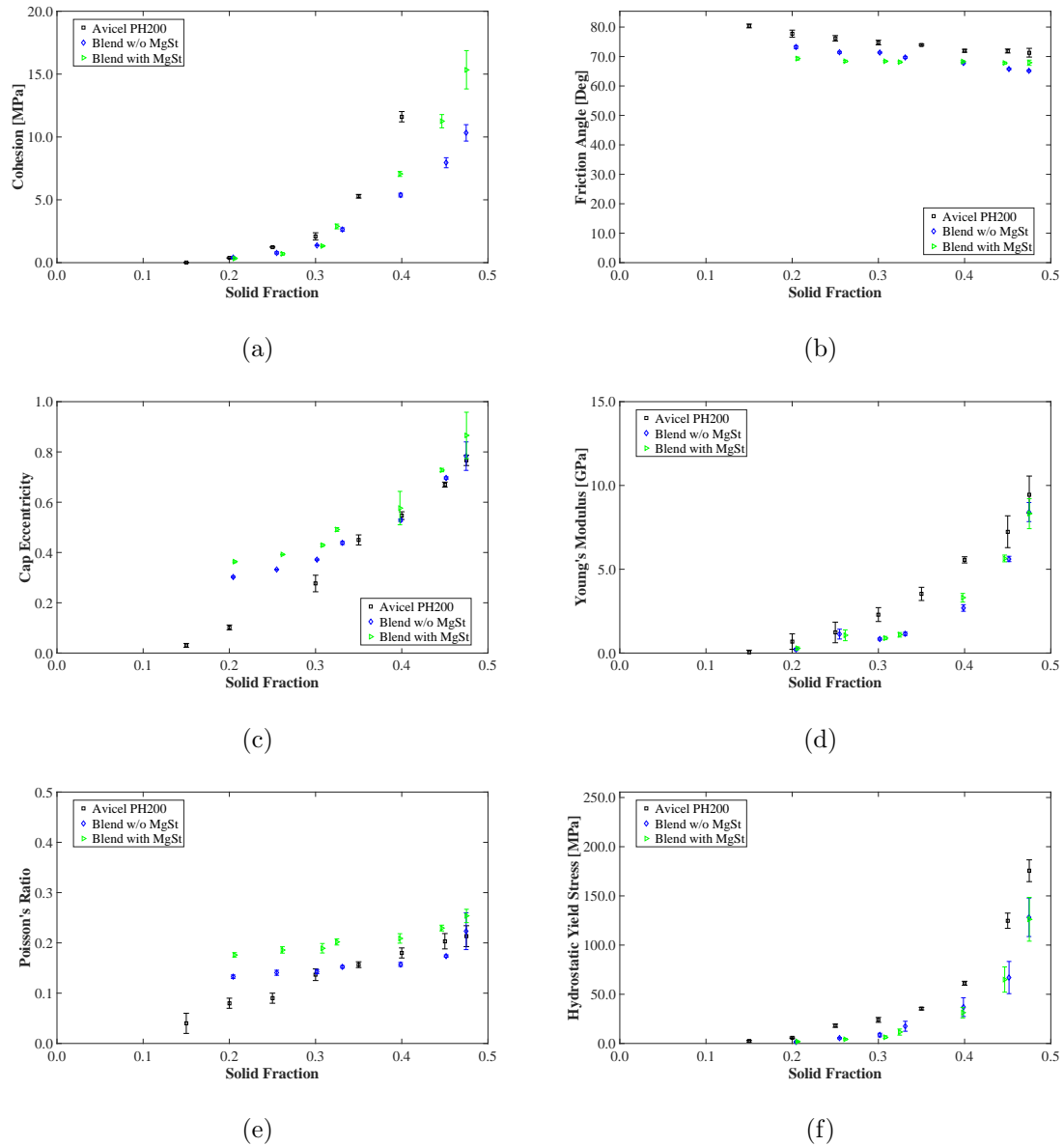
Figure 3.6. DPC material parameters for the formulations used in the present study. Data for Avicel PH200 are included for comparison. The scatter bars on the data points correspond to error propagation in the measurement of individual components used to calculate each parameter.

3.6 Summary

This chapter describes a methodology for measuring powder DPC properties. The DPC material parameters can be used as a tool for material assessment. However,

it must be noted that in this study the strength of the blend containing magnesium stearate was stronger than the blend without magnesium stearate, which is contrary to what is normally observed [40, 49, 71]. These blends were stored in an environment in which the humidity was not controlled beyond typically building conditions. A fraction of the same blends, having lower moisture content stored at a different facility showed the opposite trend; the with-MgSt blend was weaker than the without-MgSt blend. Imaging of the different blends showed that the blends with higher moisture content were more agglomerated than the blends with lower moisture content. The apparent densities of the blends with lower moisture content were also different (1.541±0.009 for the without-MgSt blend, 1.539±0.007 for the with-MgSt blend) and closer to the true density values than the blends with higher moisture content. These results suggest that absorbed moisture has an influence on the blends DPC properties. Hence, the influence of the lubricant observed in this work may not be typical. In the next chapter we describe the methodology to obtain the adhesive interaction parameters between the tooling and the powder compaction using an instrumented punch for these blends.

4. CALIBRATION OF ADHESION MODEL

4.1 Introduction

The powder-punch face adhesive surface interaction model in the FEM simulation was calibrated using an instrumented punch that can measure the adhesive force between the powder and the punch. This chapter begins with a brief review of the phenomena that can lead to powder-punch adhesion. Further sections in this chapter discuss the construction and working of the adhesion punch developed in-house,measurements of adhesive properties for the formulations used in this work.

4.2 Mechanisms Leading to Adhesion

The adhesive force between a punch face and powder is a result of several different mechanisms including van der Waals forces, electrical forces, electrostatic forces, capillary forces, and contact melting [2, 39, 73]. The forces resulting from permanent or instantaneous dipole moments between molecules are collectively known as 'van der Waals forces'. van der Waals forces occur between all materials and are most significant when surfaces are in close proximity, less than 100 nm [74]. Capillary forces arise from liquid bridges in the gap between contacting bodies. In dry, cold compacted powders, liquid bridging can be neglected as a significant source of adhesion [75]. Electrical forces arise from differences in the contact potential for a particle-surface contact in a dry environment and are only relevant for particles smaller than 5 μm [76]. Electrostatic forces arise from an accumulation or depletion of charge on materials. Tribocharging of materials, especially non-conductive ones in low humidity environments, is a common source of charge transfer [77]. This force is most relevant for particles between 5 μm to 100 μm [76, 78]. Contact melting occurs for materials that have a low melting point. The heat generated during powder com-

paction can partially melt particles onto a punch face resulting in adhesion. Clearly, the mechanisms leading to adhesion are quite complex and require equally complex techniques to measure them. Some of the adhesion force measurement techniques used in the pharmaceutical industry are discussed in the next sub-section.

4.3   Techniques for Measuring Adhesion

The adhesive interaction between a punch face and powder may be characterized by measuring the maximum adhesive force, F_{adhesion}, the work required to separate two adhered surfaces, W_{adhesion}, or the mass of powder adhered to a punch face, M_{adhered}. These quantities can be measured at the particle or bulk levels. In general, the techniques used to measure the force at the particle level require advanced technique in comparison to methods used to measure the force at the bulk level. Several of the important experimental measurement techniques used to characterize powder-punch face adhesive interactions are discussed in this section. A more comprehensive discussion of the different measurement techniques may be found in Podczeck [79].

4.3.1   Characterization of Adhesion by Particle-level Measurements

Two common measurement techniques used to characterize the adhesive interaction at the particle-level are force microscopy techniques and centrifuging techniques. Force microscopy involves the measurement of the interaction force between a sample and a probe as a function of their mutual separation distance. The interaction force is measured using a calibrated spring or, more recently, a piezo-electric crystal, which provides a more accurate measurement of the adhesive force. The separation distance between the two surfaces is monitored using an optical technique such as light interferometry. The Surface Force Apparatus (SFA) was the first technique based on force microscopy [80]. Force microscopy techniques have been improved to create more specialized techniques such as atomic force microscopy (AFM), lateral/frictional force microscopy (LFM), and ultra high vacuum atomic force microscopy (UHV-

AFM) [81–84]. A comprehensive discussion on force microscopy techniques may be found in Wang et al. [2] and Podczeck [79]. Force microscopy is becoming a standard technique for particle-level adhesion measurements since it allows for precise measurement of contact force and separation distance. However, these techniques are time consuming and require specialized equipment.

A popular technique used in the pharmaceutical industry to measure adhesion forces for individual particles is centrifuging [85]. In this technique, particles are adhered to an outward facing surface and subject to rotation, for example in a centrifuge. The particle will leave the surface when the centrifugal force on the particle equals the adhesion force,

$$F_{\text{adhesion}} = m\omega^2 R \ , \tag{4.1}$$

where 'm' is the particle mass, 'ω' is rotation speed, and 'R' is the distance between the particle and the axis of rotation. This technique is much simpler and easier to perform than force microscopy methods; however, information on the adhesion force as a function of surface separation distance is unavailable.

These particle-level techniques have two significant limitations. First, a large number of particle-level measurements are needed for statistical significance, especially since irregularly shaped particles may have different adhesive force profiles depending on their orientation. And second, these particle-level techniques are not typically performed for particles undergo significant plastic deformation or fracture, which would be the case during a compaction process. Hence, powder adhesion is also studied at the bulk level [9, 29, 46, 75, 86–88].

4.3.2 Characterization of Adhesion by Bulk-level Measurements

There have been several methods described in the literature for characterizing the adhesive force during the detachment phase of tablet compaction [9, 46, 86, 87]. Naito and Nakamichi [86] measured the "slipping force" between an upper punch face and a tablet, which was defined as the force applied at a given radius required to twist

the upper punch off the tablet surface. Tablets were made in a single station tablet press fitted with a modified upper punch and split die assembly. After the tablet was compressed, the upper punch was not retracted from the die and instead the punch and die assembly was transferred to a separate device to measure the slipping force. This slipping force was measured three times. If sticking occurred, then a larger force value was measured during the first punch rotation. The force measured in the second and third rotations was due to friction as opposed to adhesion. A challenge with this method is that the measured force is dependent on the fidelity of the transfer to the slipping force assembly. If the equipment is jostled, then it is possible that the adhesive bond between the powder and punch face may change. More significantly, the torque required to twist a compact from a punch surface is not a measure of the force required to pull a tablet off the punch surface in a perpendicular direction, as would be the case in a tableting operation.

An alternate approach to measuring the adhesion force was devised by Mitrevej and Augsburger [87]. These authors measured the sweep-off force between the lower punch and the tablet, and thus characterized adhesion between the tablet and lower punch surface. As with the previously described measurement method, there are practical concerns with this technique. First, the measured force is a combination of the adhesion force and the inertial force required to sweep the tablet off the punch (the sweeping action occurs rapidly). Second, the adhesion force is measured after ejection from the die. Frictional interactions with the die wall during ejection and elastic rebound of the tablet after the upper punch retracts, and especially upon leaving the die may cause changes to the stress state at the lower punch-compact interface. Lastly, as with the "slipping force" technique described previously, the sweep-off technique is not a direct measure of the perpendicular pull off force, but instead is a shear force measure.

Macdonald et al. [46] used a punch with a detachable face in a rotary tablet press. The mass of powder stuck to the punch surface was measured periodically during a tableting operation to determine sticking tendency. Although measuring the

mass of the powder stuck to the punch can give a good estimate of sticking tendency in practice, it does not provide adhesion force information that can be used in a predictive manner such as in a finite element method model.

Waimer et al. [9] developed a punch with a central bore to accommodate an instrumented pipe for measuring the adhesion force in a single station tablet press. The instrumented pipe contained strain gauges capable of measuring very small strains. A steel disk was attached to the end of the central, instrumented pipe and a thin steel membrane was welded to the punch face forming a seal. A schematic of the punch is shown in Figure 4.1. During the compression phase of tableting, the compression load is transferred from the steel disk to the metal body of the punch and no load is felt by the instrumented pipe. During the unloading phase, the membrane adheres to the compact, thus stretching the instrumented pipe. The degree of strain is monitored by the strain gauges and converted to a stress value. This device provides in-die adhesion force measurements in the direction perpendicular to the compact face. One of the drawbacks of the Waimer *et al.* punch is that a given adhesive load located at the circumference of the punch will result in a smaller measured strain than the same adhesive load located at the center of the punch.
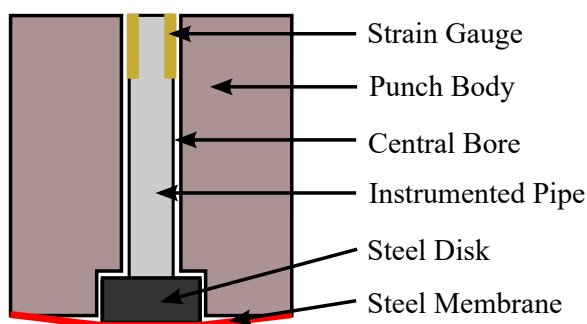
Figure 4.1. Schematic of the adhesion punch used by Waimer *et al.* [9].

The current work describes the design and operation of an adhesion punch similar to the one described by Waimer *et al.* This new punch design measures the adhesive load using a load cell instead of strain gauges and has shielded sensing components,

thus giving a less noisy signal. The new apparatus also addresses the aforementioned spatial sensitivity drawback of the Waimer punch. The punch is used to measure the adhesion load-displacement curves for several pharmaceutical component powders and blends. The data collected in this study can be used in quantitative mechanics-based models, such as the finite element method.

4.4 Instrumented Punch Design and Operation

In this section, the design and operation of the new adhesion measurement punch is described. Calibration of the punch and signal post-processing are also discussed.

4.4.1 Punch Design

A schematic of the instrumented adhesion punch design is shown in Figure 4.2. The punch assembly consisted of a 22.22 N doughnut load cell (Futek Model No. FSH00313), a metal sleeve with internal diameter of 4.76 mm and outer diameter 9.97 mm, and an S7-ACG tool steel stepped metal rod with a metal cap that was screwed onto the stepped metal rod, which together acted as the top punch. The punch face diameter was 10 mm. The S7-ACG tool steel punch face was wet-lapped to a mirror finish. The adhesion punch assembly was attached to a machine connector piece so that it could be fitted onto a universal testing machine (MTS C43.504) to perform the adhesion measurements. The load cell was connected to a National Instruments$^{\text{TM}}$ data acquisition board (Model No. BNC-2110) using an Interface strain gauge transducer amplifier (Model SGA). The test data was acquired using the MTS Testworks$^{\text{TM}}$ software package at an acquisition rate of 1000 Hz.

4.4.2 Typical Operation Cycle

A typical tableting cycle for the instrumented adhesion punch can be divided into four zones (Figure 4.3). In this figure, the gold arrow shows the direction of
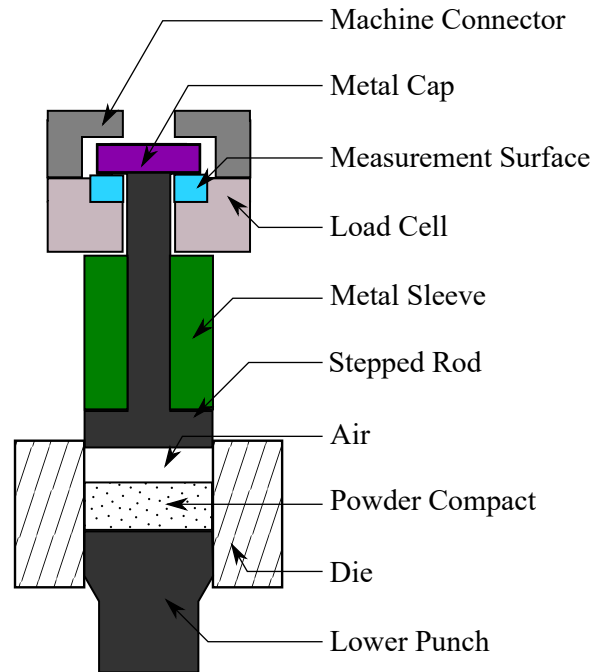
Figure 4.2. Annotated schematic of the instrumented adhesion punch (not to scale). Note that the die, powder compact, air, and lower punch are not part of the instrumented adhesion punch.

punch travel. Zone I is the part of the compaction process before the punch comes into contact with the loose powder bed. In this zone the metal cap of the punch (highlighted with the color purple in Figure 4.3(a)) is in contact with the measuring surface of the load cell (highlighted with the color blue in Figure 4.3(a)). Thus, the signal obtained from the adhesion load cell in this zone of the compaction process is the weight of the punch and the metal sleeve. In Zone II the punch comes into contact with the powder bed, resulting in a compressive load on the punch face. This compressive load causes the metal cap to lose contact with the load cell's measurement surface. Thus, any load on the punch greater than 2.51 N (weight of the punch and metal sleeve) is drained to the body of the load cell through the metal sleeve (highlighted with the color green in Figure 4.3(b)). During the initial stage of the decompression process the powder compact undergoes elastic relaxation. This phase of the unloading is not captured by the adhesion punch. Once the elastic relaxation is complete, the

punch experiences a tensile load due to the adhesive interaction between the punch and the powder compact (Zone III). As a result of this tensile force on the punch face, the metal cap contacts the measurement surface of the load cell (Figure 4.3(c)). The load measured by the load cell is equal to the sum of the weight of the punch, the sleeve, and the adhesive interaction force between the compact and punch face. Once the adhesive interaction is terminated, the load measured in the post compression phase (Zone IV) returns to the weight of the punch and metal sleeve (Figure 4.3(d)).
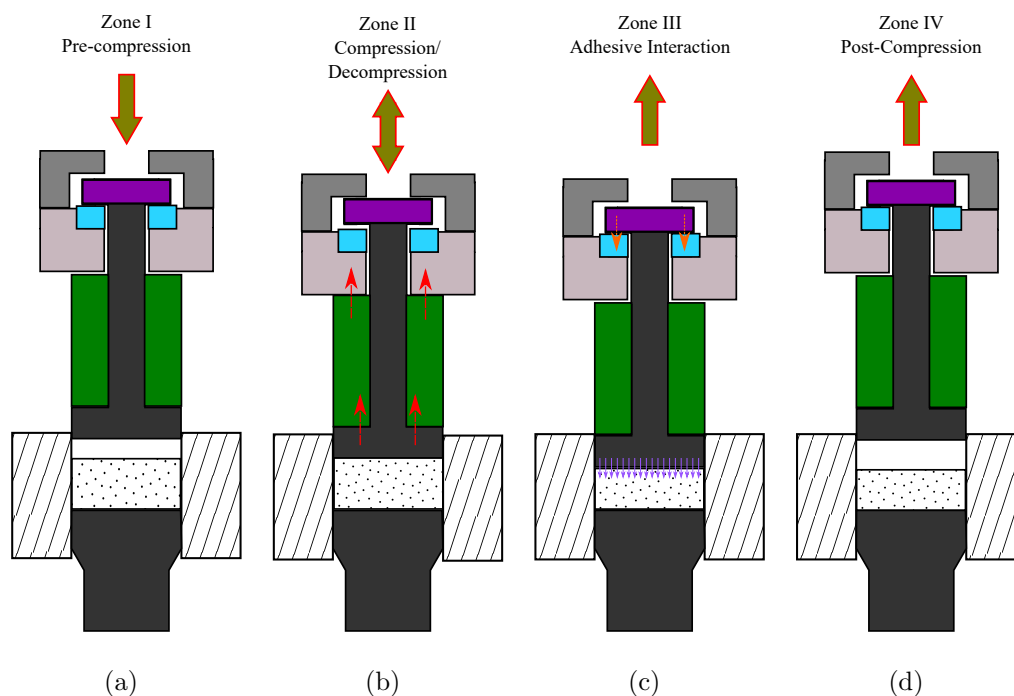
Figure 4.3. The typical operating cycle for the instrumented adhesion punch. The gold arrow indicates the direction of punch travel. In Zone II the punch first travels downwards to compress the powder to the specified solid fraction and then retracts.

4.4.3 Calibration

The instrumented punch was calibrated by applying forces on the punch from $2.5N$ N to 20.0 N in steps of 2.5 N using an MTS LSB.502 50.0 N load cell. The instrumented adhesion punch assembly was connected to the load cell using a hardened

steel bolt. The eight independent load measurements were fitted to a linear regression function with a regression coefficient of 0.9999.

4.4.4   Signal Post-processing

A typical force versus time output signal obtained from the adhesion punch is shown in Figure 4.4(a). This data, which was acquired during the compression of acetaminophen (APAP) powder to a relative density of 0.8, is representative of the output obtained from all of the tests. Data acquisition started when the top punch face enters the die. Thus, in this figure, zero time represents when the punch face is level with the top face of the die. As mentioned in Section 4.4.2, the force data acquired during powder compaction can be divided in four zones. These zones are clearly demarcated in Figure 4.4(a). Zone I is the pre-compaction zone when the punch is inside the die, but has not yet come in contact with the powder bed. The force value recorded by the load cell in this zone is the weight of the punch and metal sleeve, which for this case is 2.51 N. The weight of the punch assembly was verified independently using a mass balance. Zone II is the powder compaction zone and subsequent relaxation of the powder compact. During this phase the load recorded by the adhesion punch is zero because the metal cap of the adhesion punch is not in contact with load cell's measurement surface. The random, small load values recorded in this phase are noise, which is typical of any measurement device. The adhesive interaction between the punch face and the powder compact occurs in Zone III and is the region of interest for the experiments in this paper. Finally, Zone IV shows the loads recorded by the adhesion punch once the adhesive interaction has terminated. The load recorded in this zone is the weight of the adhesion punch and the metal sleeve.

Matlab$^{\text{TM}}$ is used to post-process the raw data. The post-processed signals are overlayed on the raw data in Figures 4.4(b) and 4.4(c). The raw data are first separated into the aforementioned four zones and only data from Zone III is post-

processed. The raw signal is passed through a Savitsky-Golay [89] filter to reduce the noise. Next, the weight of the punch and metal sleeve is subtracted from the load signal to isolate the adhesion information. The signal is then divided into adhesive loading and unloading regions, which are different from the compression and decompression phases of the powder compaction process, using the location of the peak force and fitting straight lines (Matlab function: polyfit()) to the different parts. The time $t' = 0$ corresponds to start of the adhesive loading signal. A plot of the post-processed force versus time curve is shown in Figure 4.4(b). The blue lines are for the loading portion while the red lines are for unloading. The translucent solid line is the raw data and the dashed line is the curve fit. The force-time curve is converted to a traction-displacement curve by multiplying the force with the cross-sectional area of the punch face and the time with the speed of the punch. The information in this form is useful in defining a traction-displacement relation for use in finite element method models.

It should be noted that during post-processing of the adhesion data, it was observed that for a small number of cases (less than 15%) that the force in the unloading part would not return to the punch and metal sleeve weight at the end of the adhesive interaction zone while the punch was still in the die (Zone IV). Further investigation of this phenomenon revealed that this behavior was caused by powder trapped between the punch circumference and the die wall. The data sets where this phenomenon was observed were discarded.
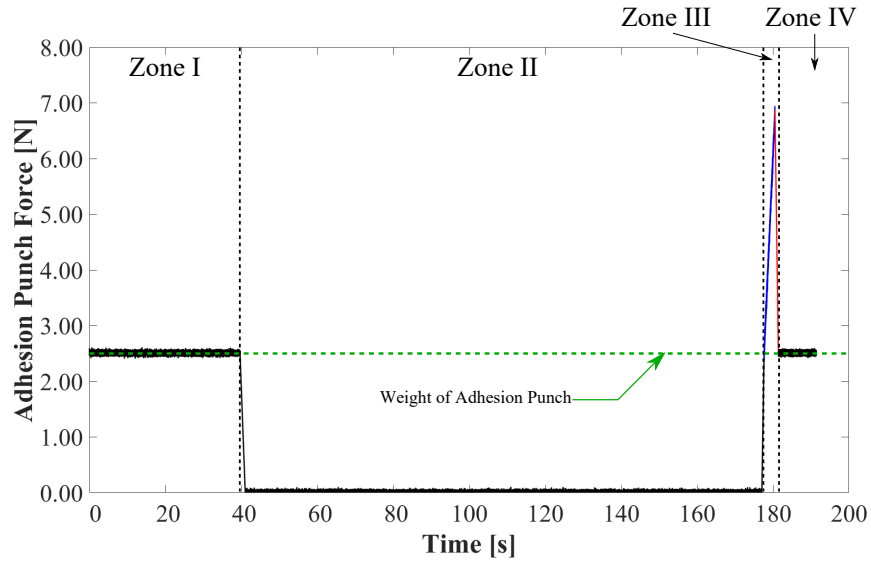
(a) Adhesion punch force plotted as a function of time during a typical compression cycle. The loading and unloading portions of the adhesion signal are plotted using blue and red colors, respectively. The black dotted line demarcate the different zones in the force signal. The green dotted line represents the weight of the punch and metal sleeve, which is subsequently subtracted from the signal.
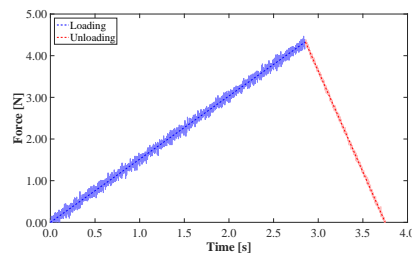
(b) The processed force signal plotted against time. The adhesive loading and unloading data are represented with blue and red lines, respectively. The raw signal is represented using translucent solid lines. The smoothened force signal is overlayed on raw data with a dashed line.
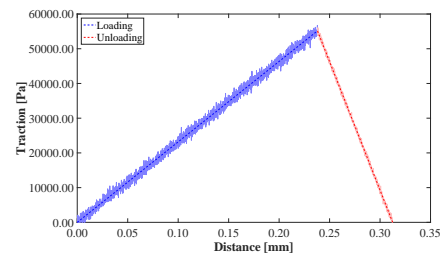
(c) The processed force signal converted to a traction-displacement signal. The adhesive loading and unloading data are represented with blue and red lines, respectively. The raw signal is represented using translucent solid lines. The smoothened signal is overlayed on raw data with a dashed line.

Figure 4.4.   Typical data from the instrumented adhesion punch before and after post-processing.

4.5 Material and Methods

In addition to testing model pharmaceutical powders blends described in Table 3.1, punch adhesion measurements were also made for acetaminophen and microcrystalline cellulose Avicel PH200. Acetaminophen is very sticky powder [90, 91] and thus was used for calibration. MCC is a commonly used pharmaceutical powder used as a non-sticking standard [9]

4.5.1 Sample Preparation

Multiple authors [9,29,73,87,92,93] have reported that the adhesive force between the punch surface and the powder compact varies with the compression force or solid fraction of the compact. Thus, the adhesive interaction between the powder and punch face was measured over a range of solid fractions from 0.3 to 0.9. In the present work, flat faced cylindrical compacts of diameter $D = 10$ mm and height $h = 7.5$ mm were produced. The mass of the compact m was varied to produce compacts of different solid fraction η,

$$m = \eta \rho_{\text{true}} \frac{\pi D^2}{4} h. \tag{4.2}$$

Note that the adhesive force interactions were measured only for those relative densities where mechanically stable compacts could be produced, i.e., those that remained intact after being ejected from the die.

4.5.2 Testing Methodology

The adhesion punch tests were performed using a single station uni-axial punch and die system installed on a universal material testing machine (MTS model C43.504). A 10 mm diameter, 22.22 mm tall die was used with the instrumented flat faced upper punch described in Section 4.4.1 and a standard flat faced $B2$-type lower punch. The lower punch remained stationary throughout the experiment. A servo encoder on the MTS machine recorded the upper punch's axial displacement. The compliance

of the punch was accounted for in these measurements. All compacts were produced at a constant loading and unloading rate of 5 mm/min. The dwell time was zero in all cases. The die walls were coated with a thin layer of magnesium stearate prior to producing each compact to facilitate removal of the compact from the die after the test. It should be noted that the punch face was not coated with lubricant since this would have interfered with the adhesion measurements. Before the start of each run, the punch and die were wiped clean with a lint-free dry rag and a lint-free rag containing iso-propyl alcohol. The die walls were coated with magnesium stearate between tests using a cotton swab after the alcohol evaporated.

Changes in the relative humidity and moisture content have been shown to influence the adhesive force between the powder and the punch face [9, 94, 95]. The measurements in this study were performed in typical room conditions. Measurements of room temperature showed that it varied by 6.2 °C (17.1 °C to 24.3 °C) while the relative humidity varied by 19% RH (45% RH to 64% RH). The temperature and relative humidity were monitored but not controlled.

4.6 Results and Discussion

In this section the results from the adhesion characterization tests are presented and discussed. First, the differences in the traction-displacement plots for the blends are described. The effects of solid fraction, and blend lubrication are presented in separate subsections.

4.6.1 Differences in Traction Displacement Behavior

Most studies on powder-punch adhesion only report the peak value of the adhesive force or the mass of powder adhered to the punch face [9, 39, 46, 73, 75, 88]. This type of data, however, does not contain the information needed for including adhesion in a finite element method model that could be used to predict picking and sticking, for example. A full description of the traction-displacement behavior is required [96, 97].

One of the simplest traction-displacement models is bi-linear, as shown in Figure 4.5 (refer to Park and Paulinoo [98] for a comprehensive review of traction-displacement laws). Using this model, the full adhesive interaction is defined by a failure traction τ_n, the displacement at which failure initiation occurs δ_m (the damage initiation point), and the displacement at which full separation occurs δ_t (the damage termination point). The region from $0 \leq \delta < \delta_m$ is referred to as the "growth zone" while the region $\delta_m \leq \delta \leq \delta_t$ is known as the "failure zone". The traction-displacement laws for several powders tested are shown in Figure 4.7 for an in-die solid fraction of 0.8. Clearly the bi-linear model is a good representation of the adhesive traction-displacement behavior between the powder and punch face for the tested materials. To test for repeatability, three replicates of the traction-displacement measurements were made for each material. The three replicates for acetaminophen at an in-die solid fraction of 0.8 are shown in Figure 4.6. The failure stress and damage initiation point vary little between the replicates, with spread-to-mean values of approximately 5.8% and 7.2%, respectively. The growth zone slope varies even less, with a variation of less than 4.2%. The damage termination point and failure zone slope vary much more, with spread-to-mean values of 20.5% and 12.5%, respectively. Regardless of the variability, the failure zone slope tends to have a much larger magnitude than the slope in the growth region, indicating that the bond fails rapidly.
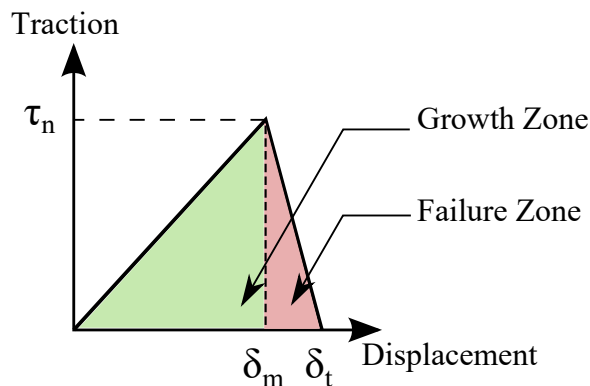
Figure 4.5. A bi-linear traction-displacement law.
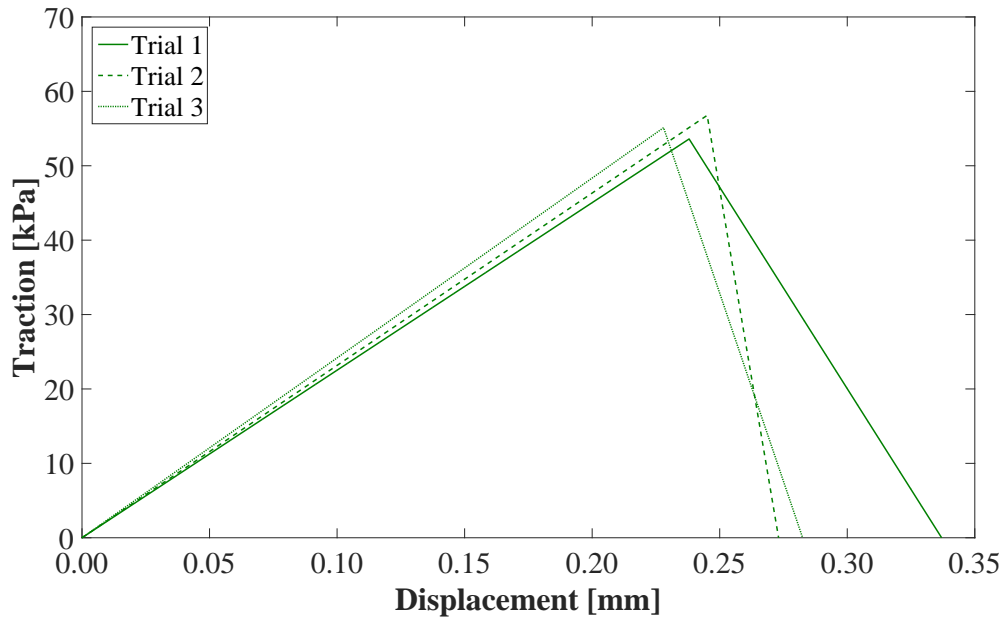
Figure 4.6. Three repeat measurements of the traction-displacement curves for acetaminophen at an in-die solid fraction of 0.8.

4.6.2 Influence of Solid Fraction and Blend Lubrication

Traction-displacement curves for acetaminophen as a function of in-die solid fraction are shown in Figure 4.8. The slopes in the growth zone are nearly equal regardless of solid fraction. Indeed, the growth zone slopes in this figure vary by less than 8.2% for solid fractions ranging from 0.50 to 0.95. In contrast, the failure stress (τ_n), and thus the displacement at which damage initiation begins (δ_m), increases with increasing solid fraction. Similar observations have been reported in the literature, with the maximum adhesive force or mass of material adhered to the punch increasing with increasing compaction stress [9, 46, 86–88].

Figure 4.9(a) plots the failure traction (τ_n) as a function of solid fraction for all of the powders tested in the current study. Similar to the observations for acetaminophen, the failure stress increases with in-die solid fraction for the other ma-
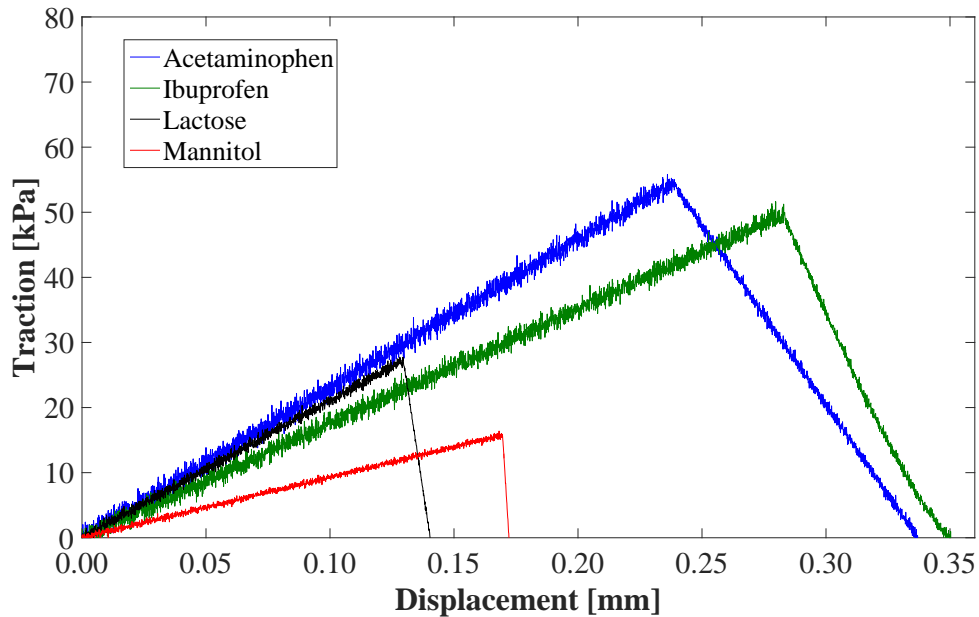
Figure 4.7. The traction-displacement behavior for four of the powders tested. The in-die solid fraction for these tests was 0.8.

terials, except for MCC (Avicel PH200). MCC did not adhere significantly to the punch face, although a small load was registered. Indeed, MCC is often used as a non-sticking powder to calibrate adhesion punches [9, 86]. The relationship between τ_n and solid fraction is nearly linear for all cases reported in this work, with the slope and intercept varying depending on the material. The larger compaction forces corresponding to larger in-die solid fractions increase the contact area between the particles and punch face as particles elastically and plastically deform and/or fracture. Additionally, the separation distance between particles and the punch decreases with increasing compaction force. This combination of effects will result in larger adhesive van der Waals forces. Other adhesive bonding mechanisms, such as contact melting, are also expected to increase with increasing compaction force, i.e., solid fraction. Thus, increasing solid fraction is expected to result in larger adhesive failure traction.
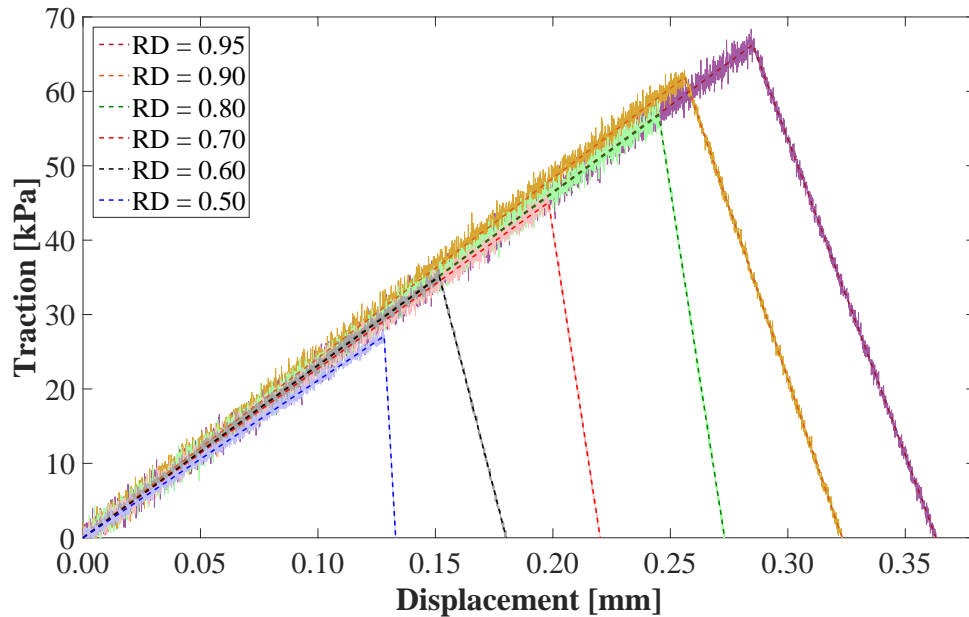
Figure 4.8. The traction-displacement curves for acetaminophen as a function of in-die solid fraction. The translucent solid line is the raw data. The dashed lines are the bi-linear model fit.

The growth zone slopes are plotted in Figure 4.9(b) as a function of solid fraction for the same materials, excluding MCC. As mentioned previously, these slopes vary little with solid fraction, but do vary with material. Since the failure traction increases linearly with solid fraction, the growth zone slope should remain constant with solid fraction for a bi-linear traction-displacement law.

The failure zone slopes are plotted in Figure 4.9(c). As discussed previously, there is more variability in these slopes, especially for mannitol and to a lesser degree, lactose. The failure zone slopes for ibuprofen and acetaminophen appear to be nearly independent of solid fraction, similar to the growth zone slopes. Note that the failure zone slopes are considerably larger in magnitude than the growth zone slopes indicating that failure of the adhesive bond occurs abruptly.

The influence of adding magnesium stearate (MgSt), a common pharmaceutical lubricant, was also examined in this work. As expected adding increasing amounts

of MgSt reduces the adhesive interaction. Prior studies [46, 99] have shown that increasing blend lubrication to a sufficiently large value results in a plateau in the adhesive interaction force. Note that for the blend containing MgSt the compacts experienced capping. Thus, although increasing blend lubrication helps reduce punch adhesion, it may also result in weak and damaged tablets.

Data from the literature is not available for making direct comparisons of the current data. However, Rasenack and Muller [100] reported poor "tabletability" for acetaminophen. They state that the poor tabletability was due to a combination of the strong inter-particle cohesion and strong powder-punch adhesion. Waimer et al. [9] measured the failure stress for sorbitol and observed that the adhesive force was larger at larger compaction forces. This essentially translates to higher adhesive stress at higher solid fractions.

4.7 Summary

In this chapter we discussed the development of an instrumented punch used to characterize the adhesive force between a punch face and powder. Measurements of the failure traction, growth zone slope, and failure zone slope were made for several pure pharmaceutical materials and blends containing a lubricant. The effects of compact solid fraction and mass fraction of lubricant were investigated.

This information is needed for modeling sticking and picking during tableting using numerical techniques such as the finite element method. The observations regarding solid fraction are also useful since they can be used to reduce the number of experimental measurements required for calibration of adhesion properties.

It is important to note that the data collected here was specifically for a stainless steel punch. The adhesive properties for other punch surface materials would likely be different. Measurements of the adhesion properties would need to be made for each powder-punch material pair. Furthermore, difference in adhesion properties are also expected for different punch face surface finishes.
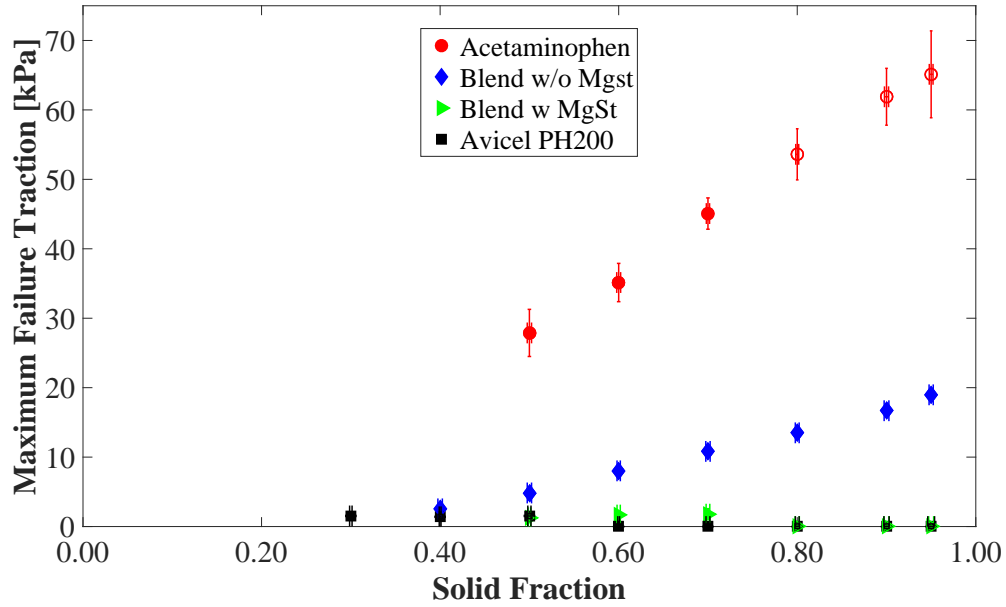
(a) Failure traction.
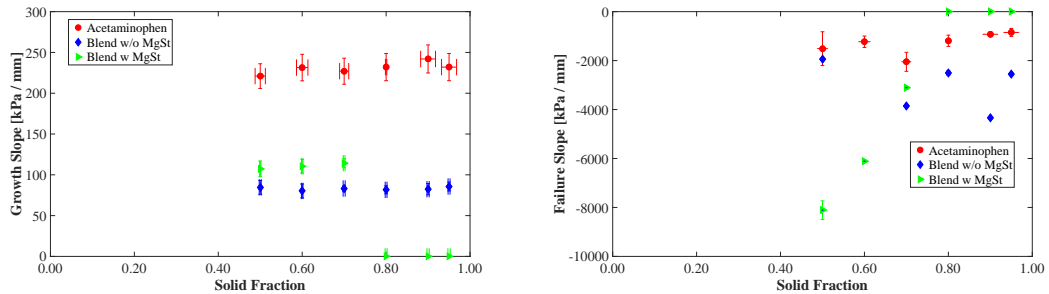
(b) Growth zone slope.

(c) Failure zone slope.

Figure 4.9. The failure traction (τ_n), growth zone slope, and failure zone slope plotted as functions of the in-die compact solid fraction for the tested pure materials. The plot symbols are the mean of three replicate experiments while the vertical and horizontal bars indicate the spread in the values and solid fraction, respectively. The open symbols indicate compacts that capped upon ejection from the die.

5. CALIBRATION OF COHESION MODEL

5.1 Introduction

In this chapter the methodology to obtain the bulk fracture toughness of the powder from single edge notch bend (SENB) test is presented. The fracture toughness was used to calibrate the bulk crack initiation and growth parameters in the finite element model presented in Chapter 6.

Traditionally, the measurement of fracture toughness is not widely adopted in the pharmaceutical industry since it requires a large amount of powder which is seldom available at the initial phase of drug development. Moreover, the fracture toughness is used in the pharmaceutical industry as an index to compare the strengths of different powders compacts and not for any kind of predictive modeling. However a few researches have measured the fracture toughness for a few commonly used pharmaceutical powders [101–104].

5.2 Theory of Fracture Mechanics

Fracture mechanics is based on the assumption that all materials have inherent flaws (crack) or develop flaws when subjected to stress [105]. When adequate stress is applied to a body the crack grows further from the crack tip. The growth of the crack can be seen as a superposition of three independent movement of the upper and lower crack surface known as the basic modes of crack propagation (Figure 5.1). The modes of crack propagation are defined as follows:

- Mode I or Opening mode: In this mode the crack surfaces open symmetrically w.r.t XZ and XY plane.
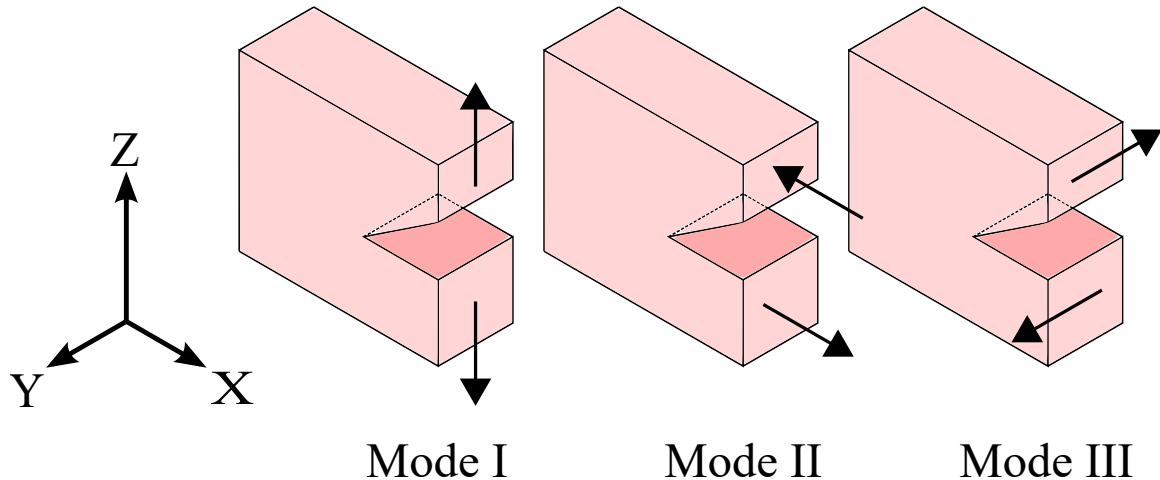
Figure 5.1. The basic modes of crack extension.

- Mode II or Sliding mode: In this mode the crack surfaces slide symmetrically w.r.t the XZ plane and skew-symmetrically with respect to the XY plane.

- Mode III or (Out of plane) Tearing mode: The crack surfaces slide with respect to each other skew-symmetrically w.r.t to the xy and xz plane.

The crack growth is accompanied by non-linear effects like crack tip stress singularity and plastic deformation near the crack tip. In some cases, the non-linearities can be assumed to be small when compared to the characteristic length scale of the part [106]. In such cases the crack initiation and growth process can be approximated using linear elastic fracture mechanics (LEFM) [105, 106]. The LEFM approximation has been reported by multiple authors as a reasonable assumption for powder compacted material [107, 108]. To model the initiation and crack growth in FEM softwares using the LEFM assumption a constitutive relationship for crack initiation and growth must be specified. Typically, the constitutive relationship is phenomenological in nature due to the absence of physics based first principle models for crack growth in powder compacts [109]. The parameters to define the crack pro-

rogation and growth were obtained from the experimental measurement of fracture toughness [98, 110–114].

5.3 Standard Technique for Measuring Bulk Fracture Toughness

One of the common test used to calculate fracture toughness is the single edge notch beam (SENB) test in three or four point bending. The three point bend test was used in this work to characterize the bulk fracture toughness of the powder compacts. In this test a rectangular test specimen is placed between two rigid pins and a third pin is lowered from above at the center of the beam to induce crack growth in Mode I (Figure 5.2). The basic concept behind this approach is that for crack initiation and growth under static loading the stress intensity should be greater than the critical value to initiate fracture (Stress intensity approach). An alternate way to think about this phenomenon is that the energy released during crack growth should exceed the energy needed to form a new surface (Strain energy approach). Assuming plane stress the stress intensity at the crack tip is related to the energy release rate as [105]:

$$K^2 = E \cdot G \ , \tag{5.1}$$

Where 'K'is the stress intensity factor, 'E'is the Young's modulus and 'G'is the strain energy release rate. The crack will grow when the stress and energy release rate reach a critical value. This is typically designated using the subscript 'IC'. The K_{IC} is calculated from the peak load '$P_{fracture}$', the notch dimension 'a_{notch}'and simply supported length of the beam 'L_{beam}'and the width 'h_{beam}'and in plane thickness 'b_{beam}'of the beam as,

$$K_{IC} = 3P_{fracture}L_{beam}\frac{\gamma}{2}a^{0.5}b_{beam}h_{beam}^2 \ , \tag{5.2}$$

where,

$$\gamma = 1.99 - 2.47\left(\frac{a_{notch}}{h_{beam}}\right) + 12.97\left(\frac{a_{notch}}{h_{beam}}\right)^2 - 23.17\left(\frac{a_{notch}}{h_{beam}}\right)^3 + 24.80\left(\frac{a_{notch}}{h_{beam}}\right)^4 \tag{5.3}$$

is the compatibility curve γ which is obtained empirically [115].
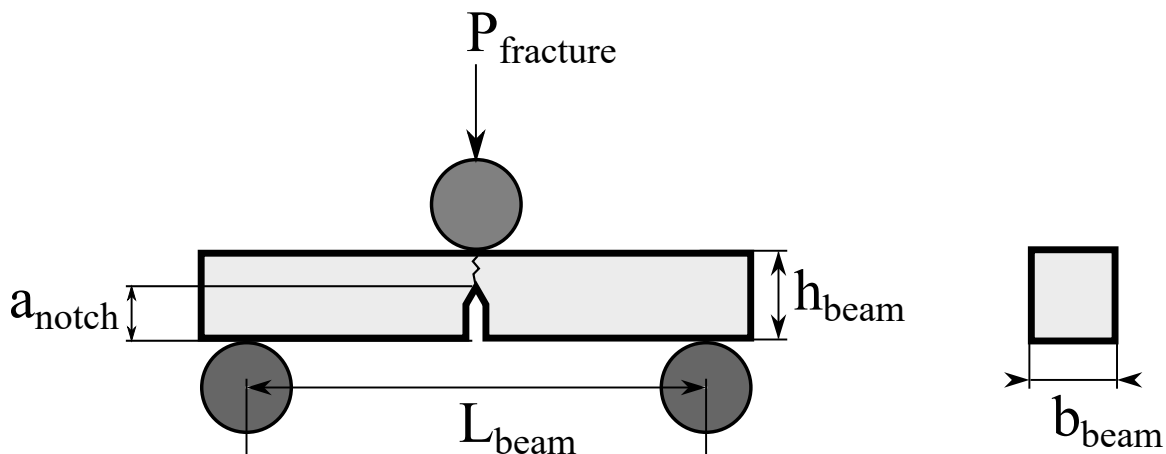
Figure 5.2.   Schematic of single edge bend test used to determine fracture toughness.

Typically, Equation 5.2 is used to obtain the fracture toughness. The compatibility curve in this equation however is not intended for samples produced by die compaction since compacts produced by die compaction have an inherent density distribution because of frictional interaction between the tooling and the powder [20,65,67]. Thus using the formula will give a conservative estimate of the fracture toughness. In such cases the fracture toughness is determined by matching the experimentally obtained load-displacement curve from the three point bending test to load-displacement curve obtained from finite element simulations for the same loading conditions [116]. This methodology is presented in Section 5.4.3 and Section 5.4.4.

5.4   Methodology

5.4.1   Material

In addition to testing model pharmaceutical powders blends described in Chapter 3, fracture toughness measurements were also made for Avicel PH200 a commonly

used pharmaceutical excipient for which fracture toughness values have been reported in literature [101–104, 117].

5.4.2   Sample Preparation

Multiple authors [102–104, 117] have reported that the fracture toughness of the powder compact varies with the compression force or solid fraction of the compact. Thus, the fracture toughness of the powder compact was measured over a range of solid fractions from 0.4 to 0.95. The bulk fracture toughness specimens were made for the three-point fracture testing was adapted from the ASTM E1820 [118] and E399-12 [119] standards. In these methods the K_{1C} is measured by ensuring that the plastic zone accompanying the crack tip is very small relative to the specimen thickness and the plane strain condition is dominant around the crack tip. Thus, rectangular parallelepiped compacts 34 mm x 8 mm x 4 mm were prepared for fracture testing on the MTS C43.504 universal testing machine. Special punches and dies were fabricated to create the rectangular samples with a V-shaped notched crack (Figure 5.3). A crack was produced normal to the 4 mm x 34 mm face in the compaction process. The depth of the notch was 4 mm and the notch angle was 60 degrees. The mass of the compact 'm' was varied to produce compacts of different solid fraction 'η',

$$m = \eta \rho_{\text{true}} L_{beam} b_{beam} h_{beam}. \tag{5.4}$$

To decrease the density gradients in the compact as a result of powder tooling friction, the tooling was cleaned with iso-propyl alcohol before each trail. After the cleaning step the punch and die were lubricated by compressing a MgSt compact. Note that the punch speed for sample preparation was maintained at 5 mm/min.

Figure 5.3. Tooling used to make compacts with v-notch for SENB fracture testing.
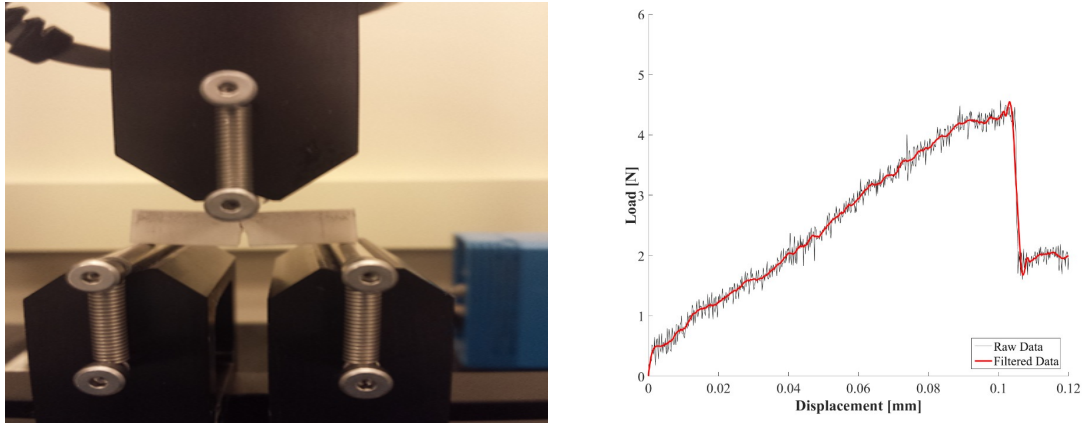
(a) Single edge notch test experimental setup.   (b) Typical test data obtained from SENB test.

Figure 5.4.   Experimental determination of fracture toughness from SENB test.

5.4.3   Load Displacement Curve from Single Edge Notch Bending Experiments

The load displacement curve needed to measure the fracture toughness was generated on a MTS C43.504 universal testing machine using the three point bending fixture. The test specimen was placed on two supporting pins at a distance of 32mm and a third pin was lowered from above at a constant rate of 5 mm/min until failure. The test terminated automatically when a break event was which was indicated by a sudden drop in the force signal. The test setup is shown in Figure 5.4(a) and sample data from the test is shown in Figure 5.4(b).

5.4.4   Fracture Toughness by FEM Back-fitting

The FEM simulations needed to calculate the fracture toughness was performed in Abaqus^{TM} a commercially available finite element program. A 2-D simulation was performed with a rectangular compact. The compact dimensions were identical to the compact used in the experimental 3-point bending test (Fig 5.5). The initial solid fraction of the FEM compact used in the 3-point bending simulation was defined using

a sub-modeling approach in Abaqus. In a sub-modeling approach the initial solid fraction and stress state of the FEM compact used for the 3-point bend simulation is obtained from a independent FEM simulation where a rectangular compact is produced by uniaxial compaction similar to the experiment.
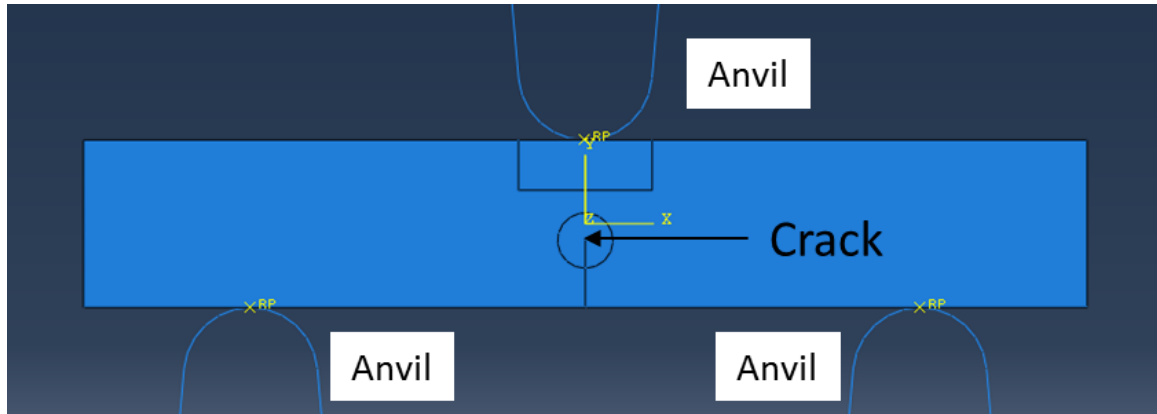
(a) FEM model setup of SENB test.
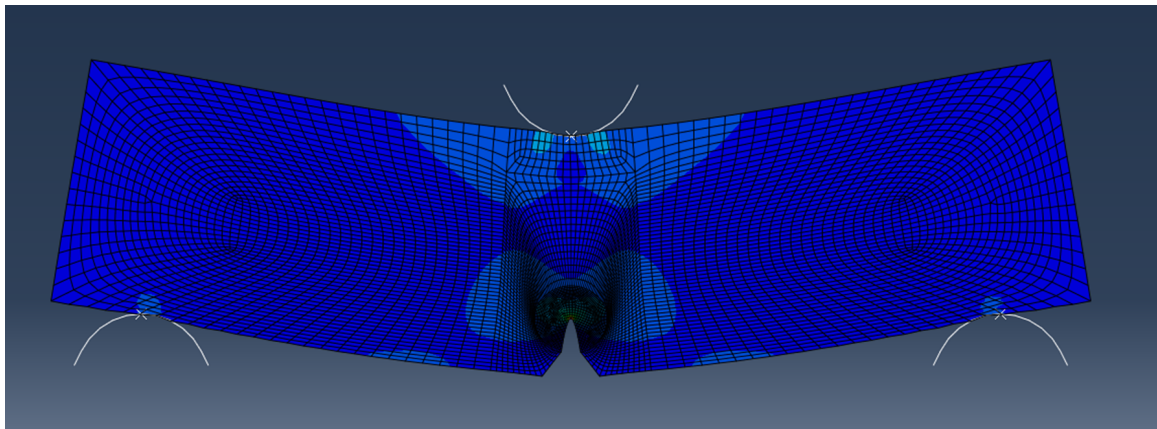
(b) Sample result from FEM model of SENB test.

Figure 5.5. FEM model to obtain compliance curve for SENB test.

The powder compact was represented with quad-dominated plane stress element with modified-DPC material properties. Simply supported condition is defined as the boundary condition and a seam crack is defined at the center of the beam. The model definition is completed by defining the crack tip and the crack propagation vector. The load is applied with a displacement controlled boundary condition to match the load-

ing conditions of the experiment. The simulation is solved using an implicit scheme and thus can be treated as a monotonic quasi-static loading condition similar to the experiment. The experimentally obtained load displacement curve was overlayed on the experimental FEM curve such that the peak load and crack extension from the experiment and simulation were within 5% of each-other (Figure 5.6). The fracture toughness is directly obtained as an output field from the Abaqus$^{\text{TM}}$ simulation. It should be noted that the shape of the load displacement curve obtained in FEM is different from the experimentally obtained load-displacement curve. Although the exact reason for the mismatch is unclear the mismatch may be attributed to the failure of the FEM model in capturing all the non-linearities during the experimental crack extension process.

5.5   Results

Figure 5.7 plots the stress intensity factor (K_{IC}) as a function of solid fraction for all of the powders tested in the current study. Similar to the observations by Roberts, 1991 [103], the stress intensity factor increases with in-die solid fraction. Stress intensity factor data for Avicel MCC PH200 reported in this study were ~10% higher when compared with values reported in prior studies. The cause of the difference could be the use of the 'inverse-FEM'technique used to determine fracture toughness rather than direct application of the Equation 5.2 as described in the ASTM standard. The use of inverse-FEM accounts for softening of the material as a result of crack propagation which could be the reason for the higher values. The relationship between K_{IC} and solid fraction is exponential for all powders tested which is consistent with prior work [102–104, 117]. The larger compaction forces corresponding to larger in-die solid fraction increases the cohesive bonding between the particles due to elastic and plastic deformation and/or fracture. Thus increasing the strength of the fracture specimen.
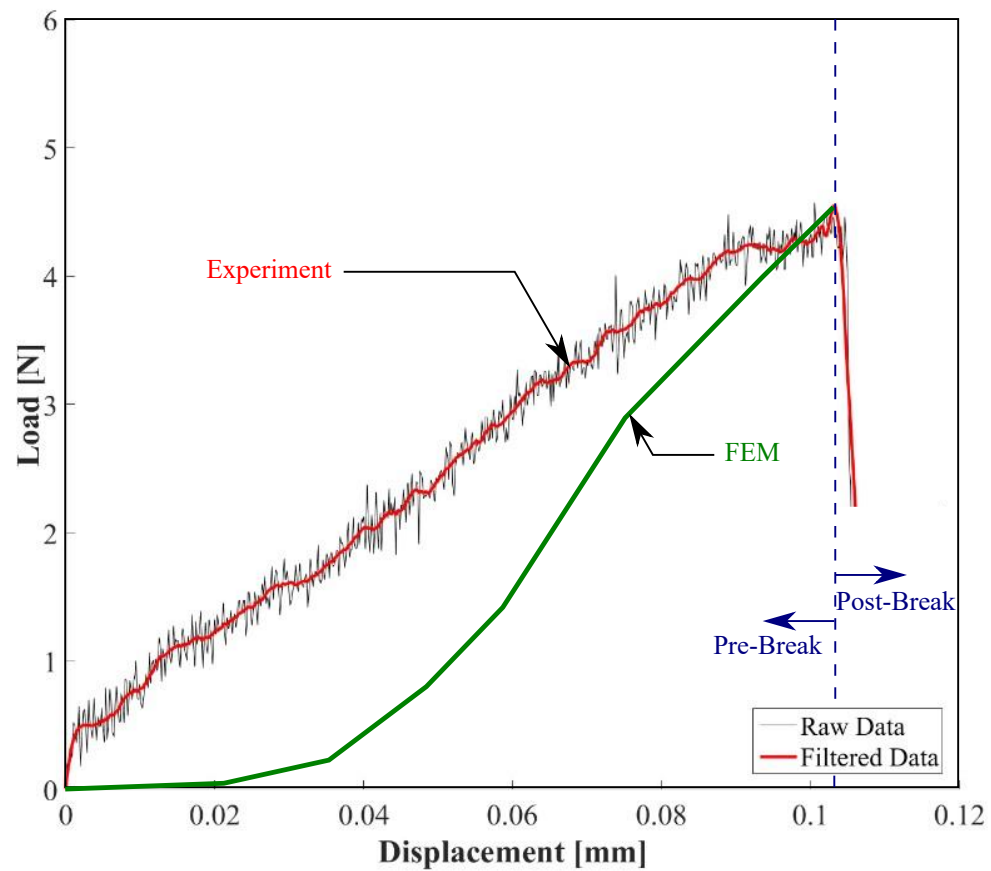
Figure 5.6. Comparison of experiment and FEM model results for determination of fracture toughness.

The influence of adding magnesium stearate (MgSt), a common pharmaceutical lubricant, was also examined in this work. As expected adding increasing amounts of MgSt reduces the fracture toughness which is consistent with prior studies [102–104, 117].
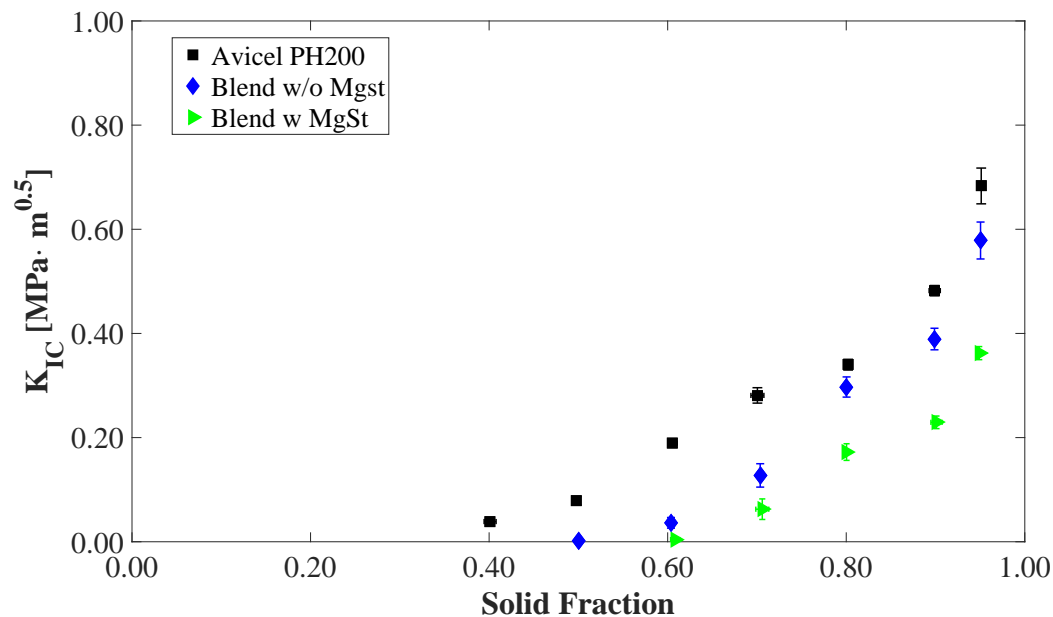
Figure 5.7. Stress Intensity factor as a function of solid fraction.

5.6 Summary

In this chapter the methodology for measurement of stress intensity factor using single edge notch bend test is discussed. The effects of compact solid fraction and mass fraction of lubricant were investigated.

This information is needed for modeling sticking and picking during tableting using numerical techniques such as the finite element method. The observations regarding solid fraction are also useful since they can be used to reduce the number of experimental measurements required for calibration of fracture toughness.

6. FINITE ELEMENT MODEL DEFINITION

6.1 Introduction

In this chapter the FEM framework used to model picking in powder compacts is presented. The DPC model parameters from Chapter 3, the adhesion parameters from Chapter 4 and the cohesion parameters from Chapter 5 are used in the definition of the finite element model.

Prior studies have shown that the modified-DPC model is a powerful tool to study powder compaction. Sinka *et al.* [15] and Han *et al.* [10] have shown that there is a density distribution within the powder compact as a result of the frictional interaction between the powder and tooling. Sinha et al. [5] investigated the sensitivity of the FEM model to fixed and density dependent material properties and showed that using density dependent properties gave a more accurate prediction of local solid fraction in the powder compact. However, these studies have assumed no adhesive interaction between the powder and punch surface which is essential to model picking behavior. In this chapter the FEM framework used to model the picking behavior is presented.

One of the objectives of this study was to understand the influence of the debossed feature geometry on picking behavior. Thus, a parametric study was performed in which the geometric parameters of the debossed feature were varied. In this study the letter 'O' was produced on the top face of a cylindrical compacts a rather simple geometry. Due to the axis-symmetric nature of the problem a 2D-slice of the cylindrical compact was simulated (Figure 6.1). This was also used an effective way to reduce computational cost.

A debossing feature is defined using five parameters [28] as shown in Fig 6.1: the stroke angle, stroke width, break radius, stroke radius, and degree of pre-pick. The degree of pre-pick is expressed as a percentage of the stroke depth. In this work the
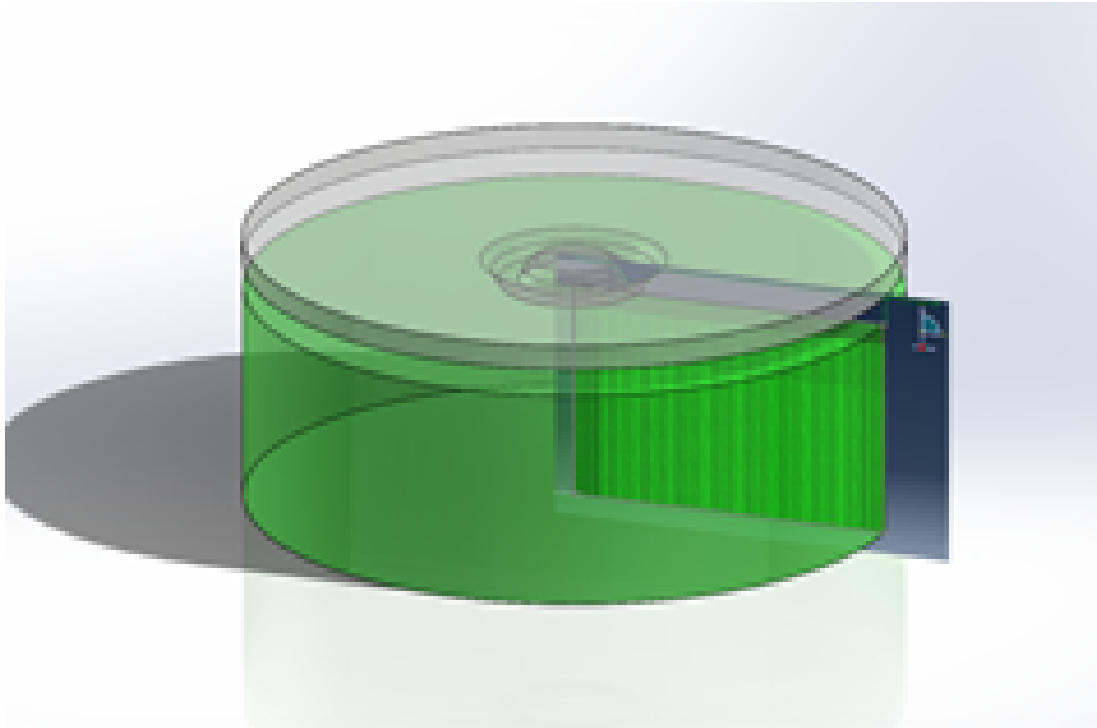
Figure 6.1. The 2D FEM simulation with the debossed feature over-layed on a 3D CAD model produced by revolving the 2D profile about the axis of symmetry.

stroke width was kept constant and the feature appearance was varied by changing the pre-pick and stroke angle. The stroke depth was a derived quantity of the stroke width and stroke angle. Because a circular feature is studied in the present work, the radius of the feature is an additional independent debossing parameter. The compact radius was set to be six times the stroke width of the feature while the final compact height was approximately five times the stroke width. This radius and height were shown through FEM simulations to be sufficiently large so that they had little influence on the final compact properties near the debossed feature.

As aforementioned the degree of pre-pick and the stroke angle were studied parametrically in the present work since anecdotally they are known to significantly influence picking behavior [28]. The remaining parameters were held constant. The values of the various debossing and compact geometric parameters are listed in Table 6.1
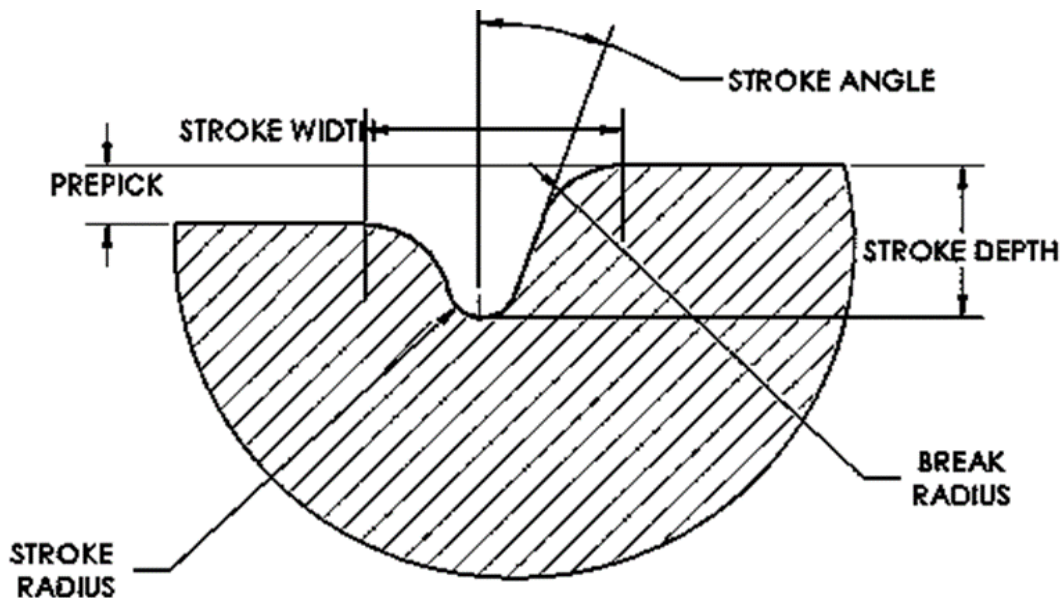
Figure 6.2. An illustration showing the definitions of various deboss-
ment parameters.

and are representative of values used in the commercial production of pharmaceutical
tablets.

Table 6.1. The debossment and compact geometric parameter values
used in the FEM studies.

Parameter	Value(s)
Stroke Angle [deg]	25, 30, 35, 40, 45
Pre-pick [%]	0, 16.7, 25.0, 33.3, 50.0
Stroke width [in. (mm)]	0.0115 (0.2921)
Break radius [in. (mm)]	0.003 (0.0762)
Stroke radius [in. (mm)]	0.003 (0.0762)
Feature radius [in. (mm)]	0.0115 (0.2921)
Compact width [in. (mm)]	0.157 (4.000)

The FEM modeling was performed using a sub-modeling approach. In this case it meant that compression and decompression phase of the tablet compaction process were simulated in two separate simulation. The stress state and density gradient from the compression phase simulation served as an input for the decompression phase simulation. The main reason for using this approach is to improve the computational efficiency of the overall simulation. The FEM model used for the decompression phase simulation was seeded with cohesive elements to model the crack initiation and growth. Additionally, an adhesive interaction property was specified to model the adhesive interaction between the punch surface and powder compact. Since these models are not required for the compression phase the sub-modeling approach leads to significant saving in computational cost.

6.2   Compression Simulation

The FEM simulations were performed in Abaqus/Explicit v6.14. Several assumptions are made in the FEM model: (1) negligible air effects, (2) the granular material stress-strain behavior is modeled by the modified-DPC constitutive relations (Chapter 3), (3) the punch and die are defined as rigid bodies, and (4) the powder compact, punch, and die system is axisymmetric, allowing for a 2D simulation to represent the full 3D compression process.

By default, ABAQUS uses only one set of DPC material properties based on the yield surfaces corresponding to a fixed solid fraction. A Abaqus subroutine (VUSD-FLD) is used to update the elasto-plastic material properties based on the evolution of relative density in the compact [5, 13, 20]. A flowchart of the subroutine is shown in Figure 6.2. At each time-step the subroutine obtained the strain increment and calculated the local solid fraction for each element in the compact. The subroutine then updated the elasto-plastic properties of each element based on the local solid fraction of the element from a table of material properties which was provided during

the material property definition. The updated material properties were used for the stress calculation in the subsequent time-step.
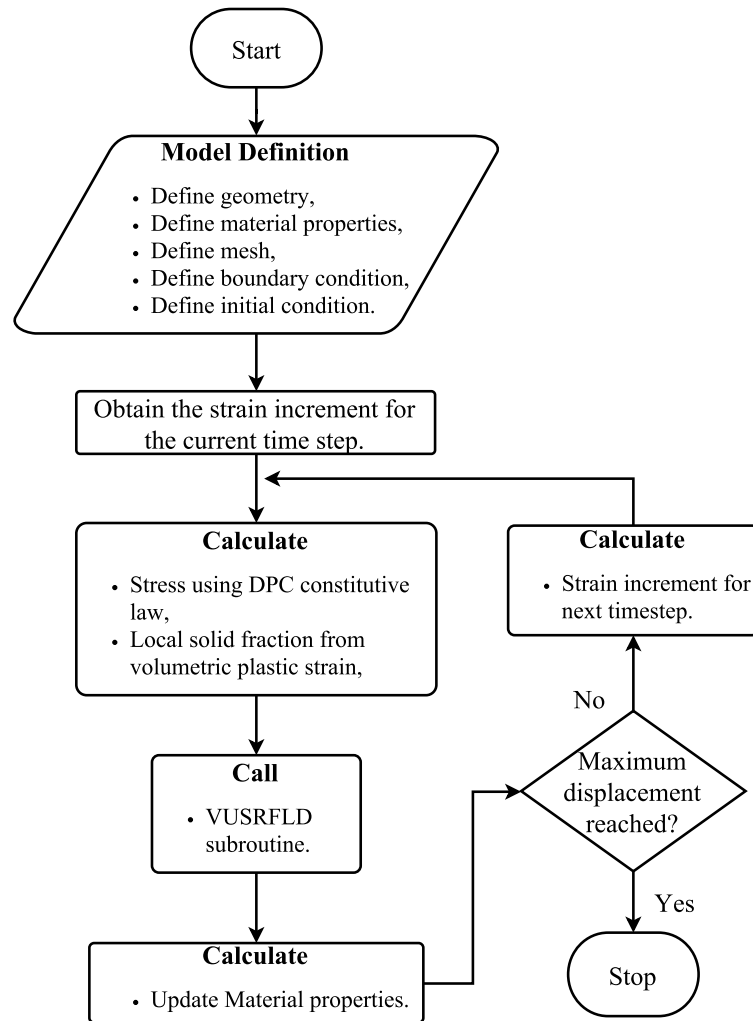
Figure 6.3. Flowchart of the user-defined subroutine.

The modeled system, is shown in Figure 6.2. It consists of a deformable powder contained within a movable upper punch, a fixed lower punch, a fixed die wall on the right hand side, and an axis of symmetry on the left hand side. The powder started with a uniform relative density of 0.35 (equal to the poured bulk density of the powder divided by the true density of the powder) and was flush with the axis of symmetry, die wall, and lower punch, with a flat upper surface in contact with the upper punch.

The powder was modelled using two-dimensional, four-node, axi-symmetric, linear quad, reduced integration elements (CAX4R). A finer mesh was used close to the upper punch, axi-symmetric, and die wall boundaries in order to better capture the large deformation gradients expected in those regions. Moreover, an adaptive meshing algorithm was employed to allow the elements to conform to large deformations. The mesh is checked and updated every five time steps. The powder was compacted by moving the upper punch downward until the final relative density of the compact was 0.85, which is typical for commercial pharmaceutical tablets [120].
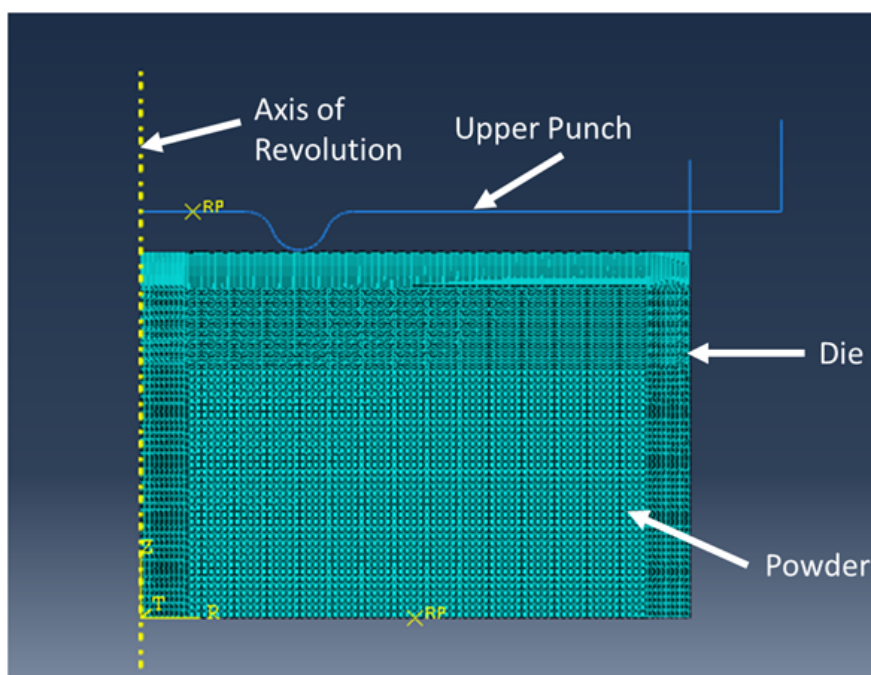
Figure 6.4. Image showing the initial configuration of the compression FEM simulations.

The powder-die boundary was modeled as being frictional, with a constant friction coefficient of $\mu_w = 0.0964$ for the blend without magnesium stearate and a value of $\mu_w = 0.0786$ for the blend with magnesium stearate. This small value is consistent with what might be expected for precision machined tooling surfaces. These friction coefficients were calculated independently of the powder characterization measurements in order to measure the coefficients of friction for unlubricated punches and

dies. These measurements were performed to simulate conditions consistent with industrial tableting processes where the tooling has no external lubrication. Using the loads measured at the upper and lower punches, F_{upper} and F_{lower}, respectively, and the radial stress, σ_r. Applying a force balance to the powder compact and re-arranging to solve for the wall friction coefficient gives,

$$\mu_w = \frac{F_{\text{upper}} - F_{\text{lower}}}{\pi D h \sigma_r} \ , \tag{6.1}$$

where, it has been assumed that the friction coefficient and radial stress are uniform over the die wall surface.

In order to ensure the FEM results were independent of the computational mesh, a mesh refinement study was performed on the 50 degree stroke angle and 0% prepick case. This case was chosen because the mesh deformation is expected to be the most significant in the parametric studies. The number of elements was increased from 7500 up to 18250 with the features stroke depth and stroke angle at the end of decompression used as performance measures (the methods for measuring these quantities are described in the following section). These quantities are used as performance criteria since they are quantities of interest in the present study. The results of the mesh refinement study are summarized in Table 6.2. The results show that the change in stroke depth is less than 3% for the model with the fewest elements compared to the model with most elements, while the change in stroke angle is less than 1%. Hence, the remainder of the simulations were performed with 12350 elements in order to provide good accuracy while maintaining reasonable computational cost.

Table 6.2. Results from the mesh refinement studies.

Number of Elements	Stroke Depth [in]	Stroke Angle [deg]
7500	0.18225	48.0025
9000	0.18706	47.9954
12350	0.18706	47.9545
18250	0.18706	47.9545

6.3   Decompression Simulation

The decompression phase was implemented in Abaqus using the sub-modeling approach as shown in Figure 6.5(a). In the sub-model the relative density and stress fields values for each element of the FEM compact was obtained from the end step of the compression simulation. In this state the powder compact is flush with the axis of symmetry, die wall, and lower punch just as before. The upper punch is in complete contact with the powder compact representative of the end of compression phase. Just as in the loading simulation the powder was modeled using two-dimensional, four-node, axi-symmetric, linear quad, reduced integration elements (CAX4R). Additionally, each integration point (node) is also seeded with two dimensional cohesive element (COH2D4) to model the crack initiation and growth process. The growth of the crack within the compact can be seen analogous to unzipping a zipper. The damage initiation criteria was selected as maximum principal stress. The damage evolution criteria for the simulation was selected as minimum energy [121]. Note that the adhesive and cohesive properties in the simulation were defined as a function of the solid fraction using a field variable. Thus in the unloading simulation the adhesive properties, cohesive properties and the material properties were varied as a function of the solid fraction with a user-defined subroutine. Identical to the loading simulation the powder-die boundary was modeled as being frictional with a constant friction. The powder punch interaction was modeled using the adhesive surface interaction property. The use of cohesion zone model makes the simulation expensive. The decompression simulation is roughly ∼50 times more computationally expensive compared to the compression simulation. There are a few underlying assumptions in the unloading simulation which should be explicitly mentioned. 1)In this approach the crack growth is not independent on the mesh density [122]. Thus to make the crack propagation more realistic it is suggested that the element dimension should represent the characteristic particle size [123–125]. The dimension of individual elements in the decompression simulation is 100μm x 50 μm. The particle size of the

(a)   (b)
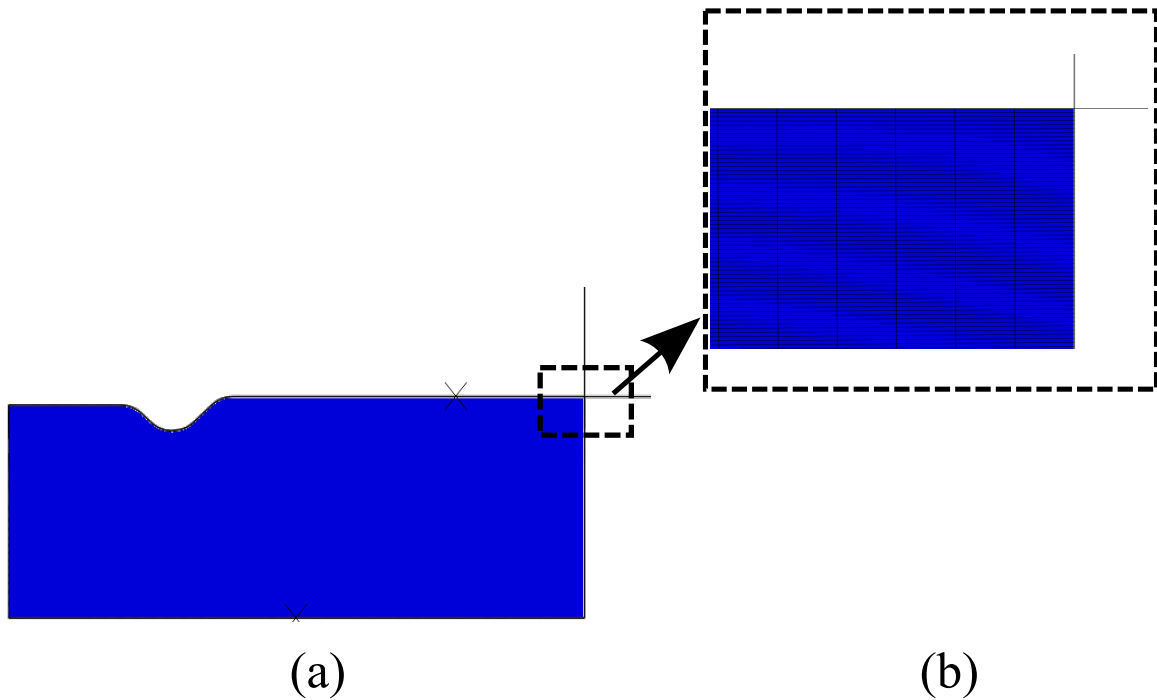
Figure 6.5.   Input for the decompression model.(a)The final state of
the compression model for the 25% pre-pick 45 degree stroke angle
compact (b) A zoomed view of the corner of the model displaying the
mesh used in the decompression model.

powder in the formulation varied from 34 μm to 200 μm. The particle size was char-
acterized using x-ray diffraction using a Malvern Mastersizer 2000 in conjunction with
the Sirocco dry dispersion attachment. 2) In the current approach the crack will only
travel along the boundary of an element and will propagate through an element. 3)
The time step for the unloading simulation was manually enforced at $1e - 11$ s to
ensure convergence. 4) The crack will only extend if the energy exceed at a given
time-step the critical energy to propagate the crack through the entire element. i.e.
partial crack growth along the element boundary was not allowed.

6.4   Summary

In this chapter the FEM framework developed to study picking behavior in powder compacts computationally in Abaqus a commercially available finite element package is discussed. The working of the user-defined subroutine to update material properties as a function of the local solid-fraction is discussed. The rationale for using the sub-modeling approach rather than a unified model for the compression and de-compression phase was explained. The parameters that were varied in the parametric study was also described. In the next chapter we focus on developing the methodology for experimental validation of the FEM simulation.

7. EXPERIMENTAL VALIDATION USING XRCT AND IMAGE-PROCESSING

7.1 Introduction

In this chapter the methodology developed to experimentally validate the FEM simulations is discussed. X-ray computed tomography imaging was used to map the outline of an experimentally produced compact with debossed features (Figure 7.1) and the compacts internal solid fraction field. In this chapter a brief description of the theory behind XRCT imaging, the limitations of XRCT and the method used to co-relate the gray intensity of XRCT image to the material density and subsequent image-processing of the XRCT image to obtain the dimensions of the debossed geometry is discussed.

7.2 Theory of XRCT

7.2.1 XRCT Principle

X-ray computed tomography (XRCT) is a the non-destructive technique which has been successfully used determine the internal structure (pores and defects) of the powder compact as well as the density distribution in the powder compact [60, 126, 127]. In simple terms XRCT provides cross-sectional images for different planes through a specimen object [128] which in this case is a powder compact. It uses the principle of third generation CT imaging illustrated in Fig 7.2. The powder compact is placed on a servo-controlled precision turn-table in a divergent beam of X-rays. As the X-ray beam passes through the specimen some portion of the X-ray beam is absorbed by the specimen. The intensity of the transmitted beam is measured by an array of detector. Note that the specimen is rotated about its own axis at a controlled step rate in the X-ray beam. This produces a series of X-ray shadow or projection

Figure 7.1. Debossed tablets produced for the experimental valida-
tion of the FEM simulation. Picking was observed in some of the
tablets produced experimentally.

images at different orientations. The sample is then translated vertically by a finite
amount to obtain a new series of projections at a new cross sectional plane of the
specimen. This entire set of projection images is used in the three dimensional ($3D$)
reconstruction of the specimen (called tomograph) using a mathematical algorithm
based on the Beer Lambert's law of absorption (Equation 7.1)

$$I = I_0 e^{-\mu x} \ . \tag{7.1}$$

Where I is the intensity of the transmitted ray, I_0 is the intensity of the incident
ray, μ is the local attenuation coefficient and x is the thickness of the material. The
reconstruction has a spacial volume resolution which is called a voxel. The voxel
size of the tomograph depends on the distance between the specimen and the X-
ray source which defines the magnification, the detector size and vertical step of the

specimen. In Equation 7.1 the local attenuation coefficient depends on the local
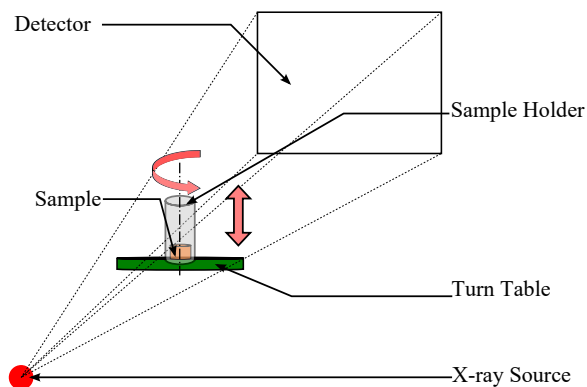
Figure 7.2. Schematic of X-ray tomography.

material density and the chemical structure of the material [129]. Thus for compacts made from a given material the intensity is purely a function of the local material density/ solid fraction. A comprehensive review on the XRCT technique is discussed in review papers by Stock [130, 131]. While XRCT is a powerful technique there are several artifacts that can cause errors in calculation of the absorption coefficient and subsequently in the reconstruction of the specimen. Some of these artifacts are discussed in the next section.

7.2.2 XRCT Reconstruction Artifacts

Some of the common artifacts observed in XRCT images are ring artifacts, sample misalignment, streak artifact. A more comprehensive discussion of the various artifacts can be found in S. Dale, (2014) [132]. These artifacts can be addressed through machine calibration, careful specimen preparation and/or post-processing the XRCT images [132].

Ring artifacts are caused by fluctuations in beam strength, contaminated flat panel detector or mis-calibrated detector [133–136]. This problem manifest as a sharp ring in the image a few pixels wide. This problem can be addressed by using appropriate post-processing algorithms for flat-field correction, and/or re-calibrating the detec-

tors. Sample misalignment artifact occurs when there is misalignment in the rotating parts like the sample holder or turn-table. This error can be seen as U-shaped arcs in the reconstructed images. This error can be eliminated by checking the alignment of all the moving parts or by specifying the actual center of rotation before the reconstruction of the specimen [132]. Streak artifacts occurs due to object motion during the imaging or by angular under-sampling. This error can be identified by unexpected high and low absorption near object edges. This error can be eliminated by increasing the number of projection angles [137]. Most artifacts can be corrected by diligent selection of process parameters used for the XRCT analysis. In most cases the optimum parameters XRCT are determined by trial and error. In the next section we discuss some of the rationale in the section of the parameters used for the XRCT experimental validation.

7.3   Selection of Process Parameters

Several process variables selected for the imaging process can affect the end quality of reconstructions. The process variables that can be altered are the initial X-ray energy, the exposure time per projection, and the number of projections taken per 180° rotation. The initial x-ray energy in conjunction with the exposure time per projection determine the quality of the image. A large exposure time and X-ray energy can saturate the detector thus reducing the contrast between the image and the background. However lower than required energy and exposure time will result in a noisy image. The sampling time and energy must be determined a-priori by trial and error for optimum image quality. The number of projections taken per 180° is one of the key factors that effects the quality of the reconstructed image. Larger the number of angular steps will produce a shaprer image but also increase the imaging and reconstruction time for the image. Similar to the x-ray energy and exposure time the size of the angular step size is determined by trial and error [129].

In this study the calibration slugs were imaged using a Scano Medical μCT 40 . X-rays were produced using a voltage of 55 kVp and a power of 8 W. Three thousand six hundred x-ray intensity projections were taken per 180° rotation of the cylindrical slug. The resulting spatial resolution of the imaged slugs was 6.43 μm per voxel side. An average of two measurements was used to calculate the absorption intensity for a voxel. An aluminum filter of 1 mm thickness was used to reduce the low energy x-ray intensity, which can be preferentially absorbed and result in beam hardening artifacts [39-41]. The x-ray absorption coefficients are converted to a gray intensity value ranging between 0 and 255, with larger values corresponding to larger absorption coefficients. A median image filter with a radius of 20 voxels was used to reduce the noise in the images [39, 41].

7.4   Solid Fraction Calibration for Powder Compacts

Cylindrical compacts of 6 mm diameter, 2.5 mm thickness of a given formulation were produced for relative densities ranging between 0.60 and 0.95. These slugs were used to produce a calibration curve relating gray intensity of the image from the XRCT measurements and powder solid fractions. The slugs were made by keeping the height constant and varying the powder mass to obtain different relative densities. The slugs were created using the same compaction fixture and speed described in Section 3.4. As with the DPC calibration compacts, the die wall and punch surfaces were lubricated with magnesium stearate in order to minimize the influence of friction. The use of flat-faced punches, lubrication, and a small aspect ratio helped to produce slugs with little variation in their internal solid fraction.

Images from several of the calibration slugs are shown in Figure 7.3, with the corresponding frequency distributions of gray intensity shown in Figure 7.4. Note that the frequency distributions include values from approximately $\sim 10^8$ voxels per slug. A secondary peak is observed in Figure 7.4 due to voxels containing a combination of both voids and material. Also observed in the images are larger relative density

regions near the circumference of the slugs, which is consistent with previous experimental findings [20, 60, 65, 127, 138]. To reduce the influence of wall effects on the determination of a characteristic gray value for a given relative density, a circumferential region of 50 μm at the edge of the compact was excluded from the calculation.

(a) $\eta_{avg} = 0.6$ (b) $\eta_{avg} = 0.8$ (c) $\eta_{avg} = 0.95$
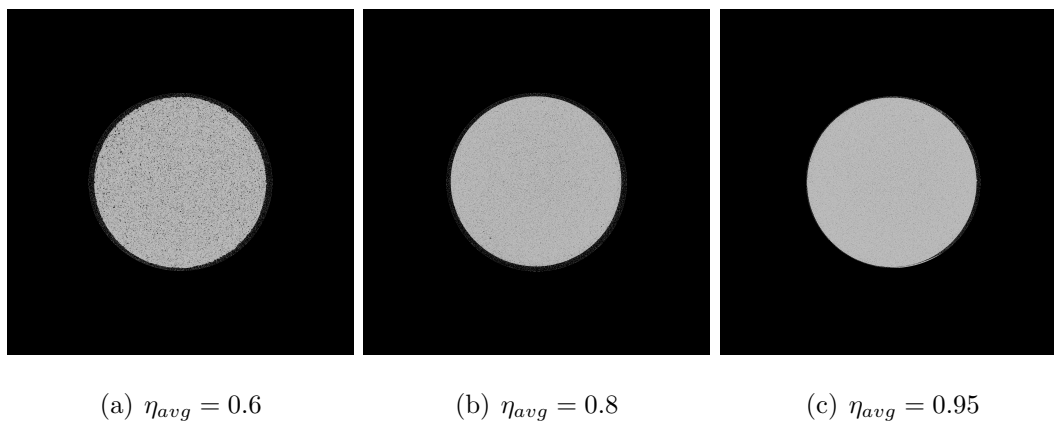
Figure 7.3. X-ray gray intensity map for a 6.43 μm thick slice located in the middle of three calibration slugs, each with a different average relative density.

The average bulk density of a slug was determined by dividing the measured mass of powder used to form the slug by the volume of the slug, which was calculated by assuming a cylindrical shape and measuring the slug diameter and height using a micrometer. The slugs relative density was calculated by dividing its bulk density by the true density of the formulation. The true density was assumed to equal the formulations apparent density, which was measured using helium pycnometry as described in Section 3.4. The mode of the gray intensity frequency distribution was plotted as a function of the average slug relative density as shown in Figure 7.5. The upper and lower cross bars in the plot correspond to the absorption coefficient values corresponding to the 25th and 75th percentiles in the cumulative distributions in order to demonstrate the (small) spread in the slug absorption coefficients. The resulting data were fit with a curve of the form,
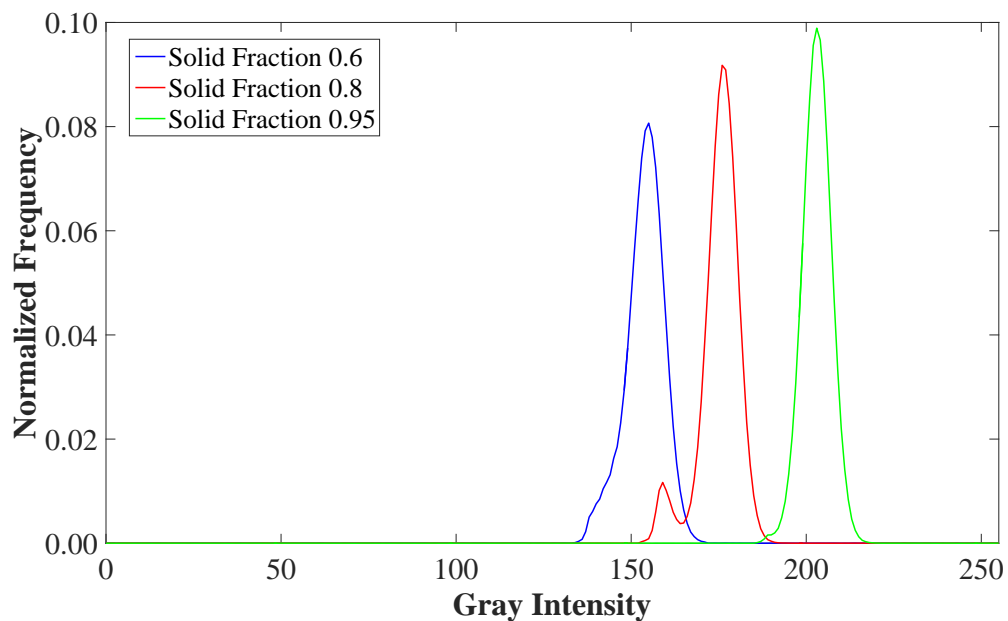
Figure 7.4. Frequency distributions of the x-ray grayscale corresponding to the three slugs shown in Figure 7.3. These frequency distributions include gray intensity values from the entire compact volume.

$$gray\,Intensity = 0.3832 * \exp(5.419 * \eta) + 144.8 \tag{7.2}$$

which was then used for converting between gray intensities and relative densities for the given formulation.
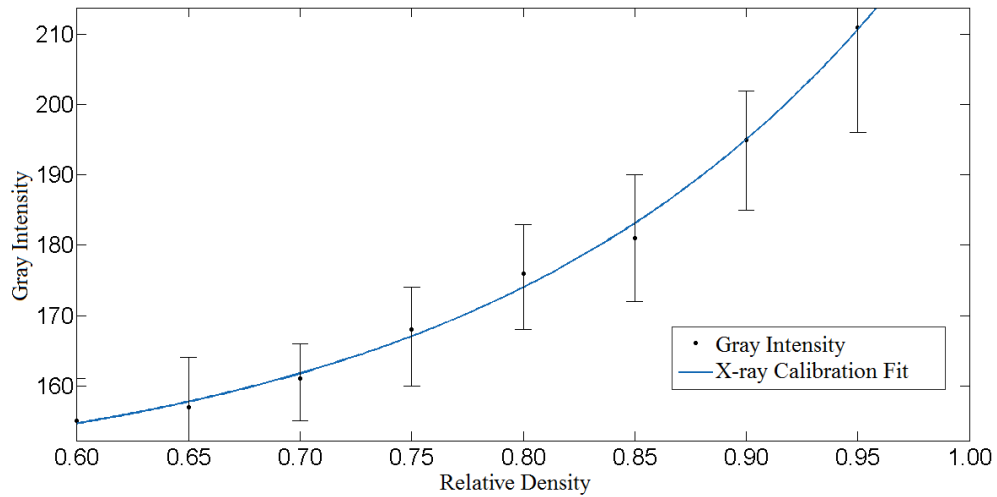
Figure 7.5. The calibration curve relating x-ray absorption coefficient to relative density for one of the formulations. The points in the figure correspond to the median value from the absorption coefficient frequency distribution with the upper and lower cross bars corresponding to the 25th and 75th percentiles.

The curve fit was then converted into a 'jet' (also known as 'rainbow' colormap) such that blue corresponds to low density while red corresponds to high density. The result from applying the colormap to the calibration slugs are shown in Figure 7.6.

7.5 Measurement of Debossed Feature Geometry by Image-Processing

7.5.1 Overview

In this section the MATLAB$^{\text{TM}}$ [139] image-processing algorithms used for calculating geometric features of the debossed region of the compact at the end of de-

(a) $\eta_{avg} = 0.6$　　　　(b) $\eta_{avg} = 0.8$　　　　(c) $\eta_{avg} = 0.95$
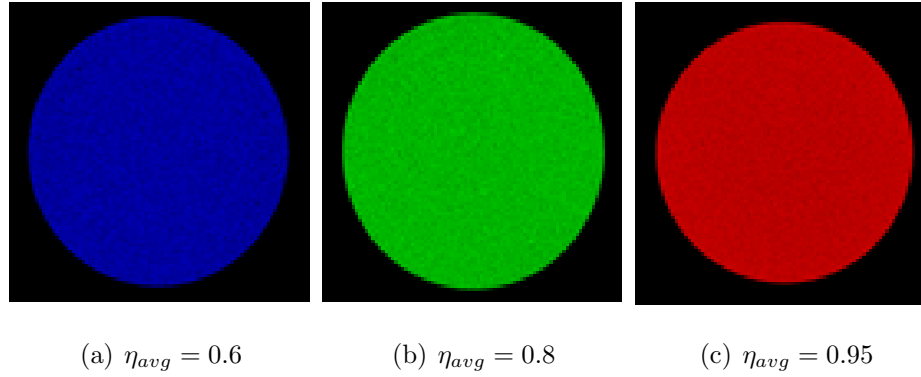
Figure 7.6. 2D slices from the calibration slugs colored using the jet colormap developed using the gray intensity data.

compression are described. In particular, the final debossed volume, feature stroke angle, and feature stroke depth were measured in order to compare to the corresponding embossed elements on the punch face. Larger differences between debossed and embossed parameters are undesirable since it means that the debossed features are further from the desired specifications. Note that the same image-processing algorithm was used to analyze the FEM results and XRCT images in order to ensure consistency in post-processing.

7.5.2 Image Processing Methodology

A 4096 × 4096 pixel image of the post-decompression state of a compact was obtained, as is shown in Figure 7.5.2(a) for an FEM simulation in order to calculate the debossed feature volume as indicated by yellow hatching in Figure 7.5.2f. The image was first converted to a binary, i.e., black and white, representation (Figure 7.5.2(b)), then the MATLAB edge-detection function [MATLAB command "edge()"] was used to find the outline of the compact (Figure 7.5.2(c)). The edge-detection algorithm inverted the color of the image, which was then re-inverted (Figure 7.5.2(d)). A Standard Hough Transform (SHT) [MATLAB command: "hough()"] was applied to detect horizontal, vertical, and lines diagonal lines in the image. These straight lines

were colored based on whether they were horizontal, vertical, or diagonal lines. All horizontal and vertical lines were colored blue, lines at a small angle to the left of the debossing feature were colored red, and diagonal lines to the right of the feature were colored green (Figure 7.5.2(e)). The curved feature was then detected as any part of the remaining upper edge. Next, the top left point on the compact was identified so that the debossed volume could be calculated. This point was found at the intersection of the horizontal line for the top-right edge of the debossed feature and the vertical line from the bottom left edge of the compact. The vertical cross-sectional area of the debossed feature was the area shown by the yellow hatching in Figure 7.5.2(f). The debossed volume was this area integrated around the compacts axis of symmetry.

The stroke angle and stroke depth were also determined for the features as shown in Figure 7.5.2(g). For these parameters, a limited angle range Hough transform was used to identify a straight-line portion along the feature walls. The line segments identified by the Hough transform are highlighted in red in Figure 7.5.2(g). The stroke angle was then obtained by applying the MATLAB polyfit function with a straight-line fit to the contour identified by the Hough transform. To determine the stroke depth of the debossed feature, the MATLAB "findpeaks()" command was used to determine the minimum location of the curved feature. The stroke depth was then calculated by subtracting the vertical location of the minimum for the curved feature from the vertical location of the top right corner of the compact.

In addition to geometric features, the relative density fields were also examined for the parametric studies. Regions of large relative density will have larger cohesion and, thus, are expected to have better mechanical integrity. Conversely, regions of smaller relative density are anticipated to be regions more likely to be subject to damage, such as picking.
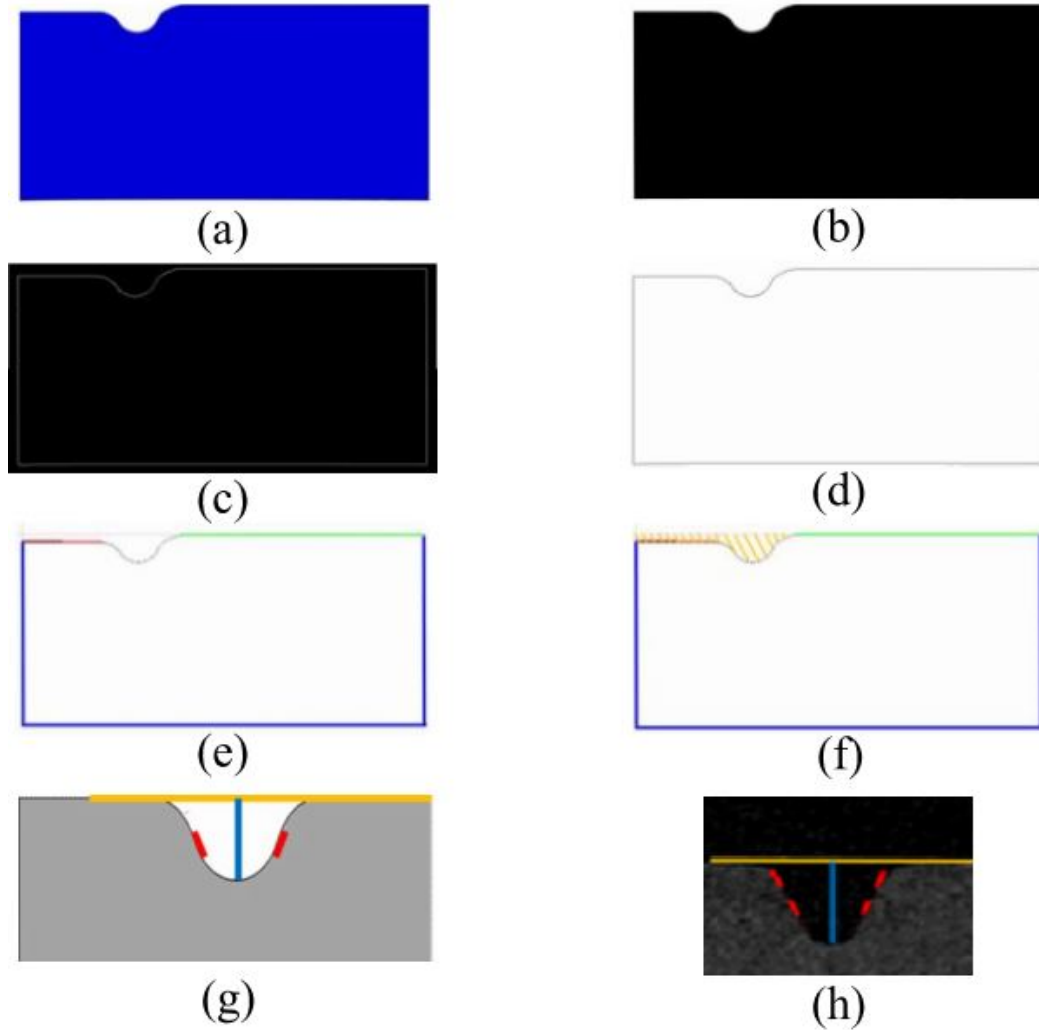
Figure 7.7. Steps used in image-processing of the FEM and XRCT results.

7.6 Summary

In summary, a calibration curve was obtained to co-relate the solid fraction of the compact to the gray intensity obtained from XRCT. The optimum process parameters for XRCT measurements for the powder compacts was determined. Additionally post processing algorithms to mitigate some of the reconstruction artifacts were implemented in Matlab$^{\text{TM}}$. Additionally, the image-processing algorithms used to post-process the XRCT images to obtain dimensions of the debossed features was

also discussed. In the next chapter some of the key findings of the current work have been discussed.

8. RESULTS AND DISCUSSIONS

8.1 Introduction

The motivation behind developing the FEM model and experimental compacts with debossed features was to develop an experimentally validated framework to predict picking in pharmaceutical tablets. Comparisons between the experimental validation using XRCT and the FEM simulation is presented in Section 8.2. An in-depth discussion of the debossed feature geometry on density distribution and crack propagation in the compact feature is presented in Sec 8.3 and Section 8.4. In section 8.5 the effects of adhesive traction separation law on the crack growth is discussed.

8.2 Comparison between FEM and Experiments

(a)   (b)
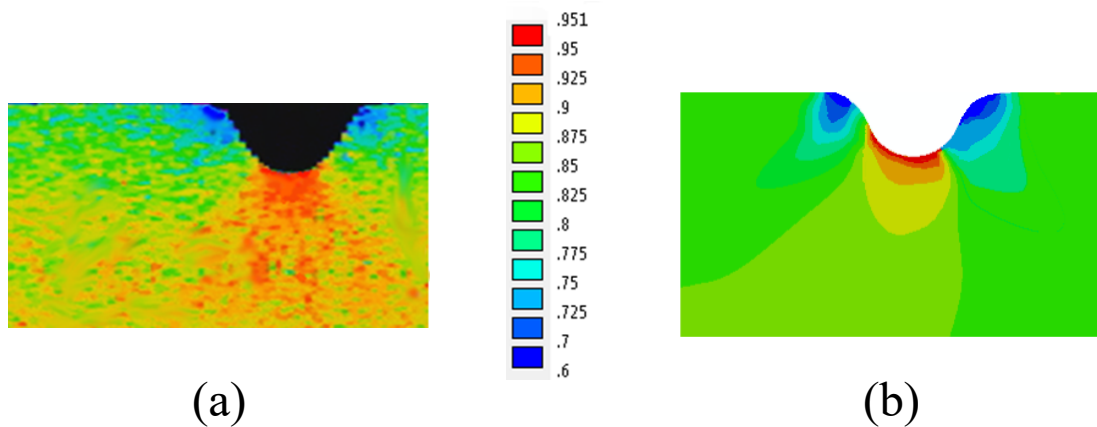
Figure 8.1. A comparison of the FEM compact and experimentally produced compact. The colormap in the image correspond to local solid fraction. (a) XRCT image of a debossed feature produced in the validation experiment (0% pre-pick, 25 degree stroke angle, and 0.2091m̃m. stroke depth) and (b) the corresponding FEM simulation.

To validate the FEM results, compacts with a 0% pre-pick, 25 degree stroke angle, and 0.2091 mm. stroke depth feature were made using the blend containing magnesium stearate. The tooling in these experiments was not pre-lubricated in order to better represent an industrial system. The powder-tooling friction coefficients used in the FEM simulations are given in Section 6.3. The compacts relative density field was measured using XRCT as presented in Section 7.4 and the feature depth and stroke angle were obtained by image processing as discussed in Section 7.5. Figure 8.2 shows the XRCT image in the vicinity of the debossed feature along with the corresponding FEM prediction. The colors in the images correspond to local relative density. The current results qualitatively match those recently reported by Laity [31]. He reported a larger relative density in the valley (furrow in the Laity paper) of the debossed feature and a smaller relative density near the shoulders (referred to as flanks by Laity). Laity also reported cracking and flaking in the vicinity of the smaller relative density regions, which is consistent with the hypothesis that the smaller relative density regions will be prone to picking. Table 8.1 gives the comparison between the measurements made on the XRCT image and the predictions from the FEM simulation. Three items of significance can be observed from the table. First, the final debossed feature geometric measures in both the experiments and simulations are different than the target values, i.e., the embossing feature values. These differences are due to the elastic spring back of the material. Second, the FEM predictions are close to the measured values in all cases. The largest relative difference of 4.9% is for the minimum relative density. The remaining parameters are different by less than 3%. Lastly, the FEM predictions slightly over-predict all aspects of the geometry and relative densities. The reason for this trend is not certain. However, an possible reason could be the use of initial linear part of the unloading curve to derive material parameters may not be sufficient to capture the elastic relaxation of the compact. The results in Table 8.1 demonstrate the power of the FEM simulations to aid in the design of powder compaction tooling where dimensional tolerance are of the utmost importance. The shape of the tooling can be appropriately altered to account for the

elastic relaxation observed in the decompression phase of the powder compaction and provide a high degree of dimensional fidelity.

Table 8.1. Comparisons between the measured and predicted debossed feature geometric measurements and maximum and minimum relative densities.

Parameter	Nominal Value	XRCT	FEM
Debossed Feature Volume [in^3]	$6.835e-6$	$6.731e-6$	$6.795e-6$
Stroke Angle [deg]	25	23.31 ± 0.000264	24.475
Stroke Depth [mm]	0.2091	0.1821 ± 0.00253	0.1897
Max Relative Density [-]	N/A	0.935	0.941
Min Relative Density [-]	N/A	0.54	0.558

8.3 Influence of Stroke Angle and Pre-Pick

Figures 8.2 and 8.3 plot, respectively, the debossed volume and the stroke depth from the FEM simulations, each normalized by the target values measured on the embossing feature, as a function of the degree of pre-pick for different stroke angles and formulations. Normalized values closer to one are more desirable since it means that the feature more faithfully reproduces the target geometry and elastic relaxation is smaller. Large degrees of elastic spring back are also correlated with increased propensity for compact failure [140]. Increasing the degree of pre-pick results in final debossed features that have larger normalized values. Indeed, the normalized values appear to vary linearly with the degree of pre-pick, with the y-axis intercept increasing and the slope decreasing with increasing stroke angle. Thus, the influence of stroke angle is smaller as the degree of pre-pick increases. Hence, to decrease elastic spring back and produce truer features, the degree of pre-pick and stroke angle should be increased. These results are consistent with the recommendations of the Tableting
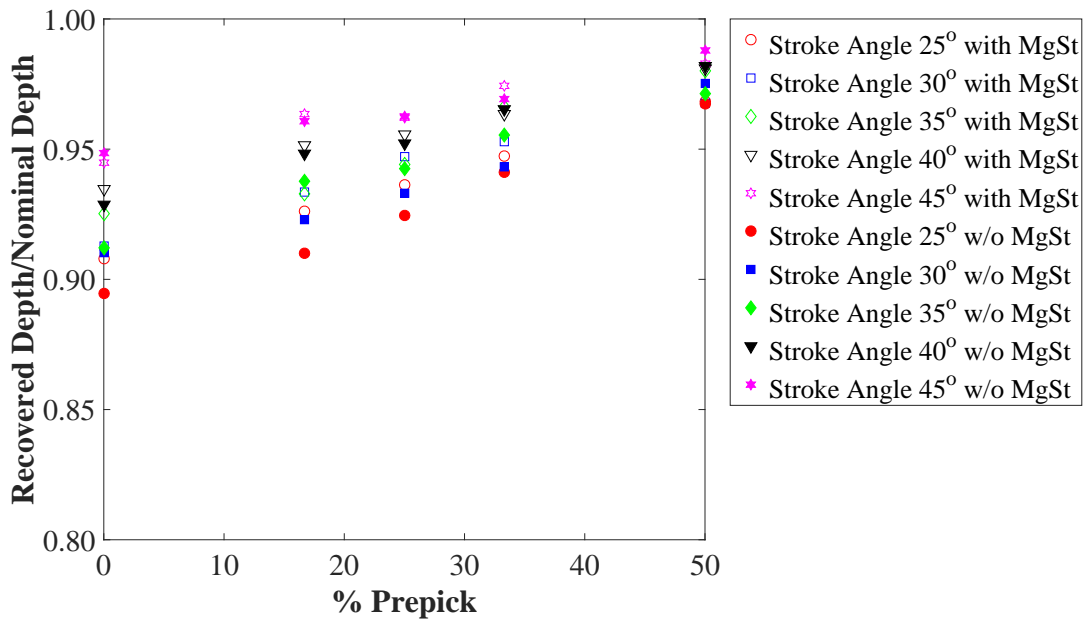
Figure 8.2. FEM predictions of the normalized debossed volume plotted as a function of the degree of pre-pick. Different symbols correspond to different embossing stroke angles. The open symbols correspond to the formulation with MgSt and closed symbols correspond to the formulation without MgSt.

Specification Manual [28], which recommends that in order to reduce the likelihood of picking, the stroke angle and degree of pre-pick should be increased. The addition of MgSt also reduces elastic spring back, but this change in the formulation has a much smaller influence than either stroke angle or degree of pre-pick.

Figures 8.4 and 8.5 show the influence of stroke angle (rows) and pre-pick (columns) on the relative density distribution in the compact for un-lubricated and lubricated formulations. The images in these figures have been cropped in a consistent manner and use identical relative density scales to facilitate comparison. Larger degrees of pre-pick clearly produce compacts with more uniform relative density, while no obvious trend is observed for varying stroke angle. In general, regions of smaller relative density are observed at the shoulders of the features while a larger relative density

region appears at the base of the feature valley. The regions of small relative density are anticipated to be weaker and more prone to damage, such as picking, due to the correspondingly small cohesion in the material. Although not plotted here, the hydrostatic and Mises stress fields look qualitatively similar to the relative density fields. The gray areas in these figures represent regions where the solid fraction is below 0.34 which is equal to the bulk density of the powder. It is expected that there are the regions most susceptible to picking.
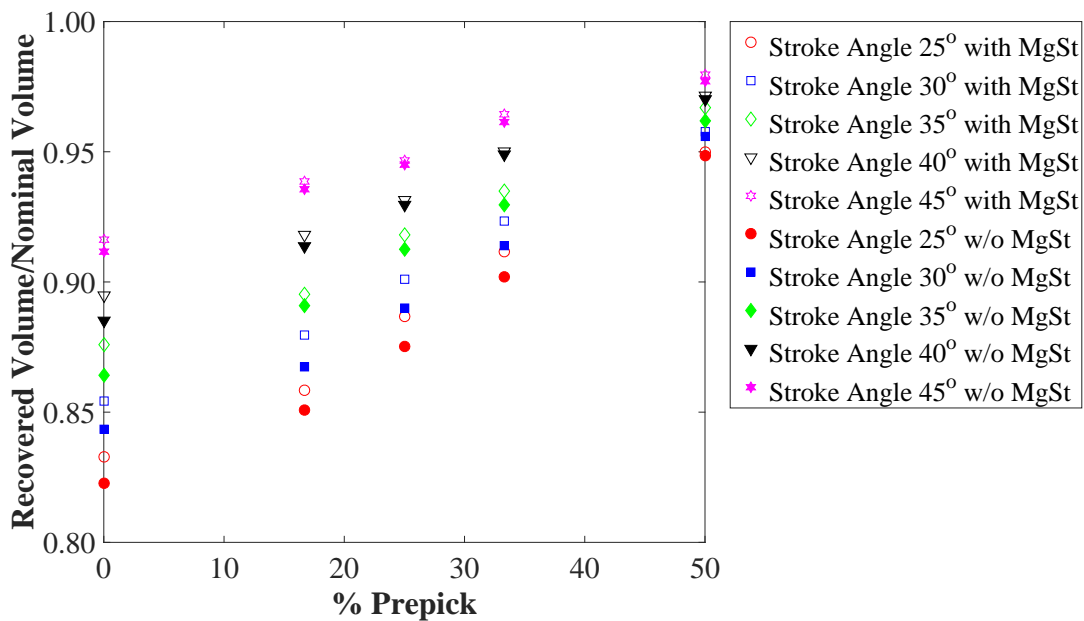
Figure 8.3. FEM predictions of the normalized stroke depth plotted as a function of the degree of pre-pick. Different symbols correspond to different embossing stroke angles. The open symbols correspond to the formulation with MgSt and closed symbols correspond to the formulation without MgSt.

Waimer et al. [29] found that for larger stroke angles, slight sticking was observed with material stuck only to the lateral surfaces of the punch while for smaller stroke angles, significant sticking behavior was observed. The current FEM results do not show obvious trends that support or refute these observations. Empirically [28], it is

know that a larger amount of pre-pick leads to smaller relative density gradients in the compact, lesser sticking in the compact, which is attributed here to a more uniform density gradient in the compact. The addition of a small amounts of lubricant has
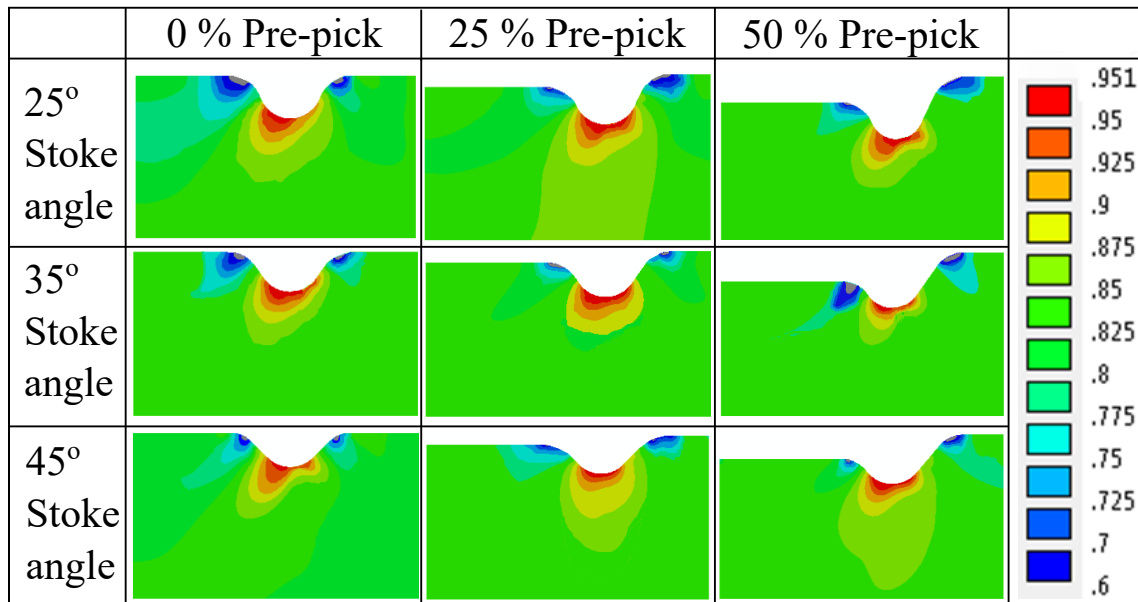
Figure 8.4. FEM predictions of the relative density fields for different stroke angles (rows) and degrees of pre-pick (columns). All of these simulations are for the un-lubricated formulation. Figure shows the region around the debossed feature and not the entire compact. The gray spots indicate regions with solid fraction lower than 0.4 which are prone to picking.

been reported to produce stronger compacts [71, 72]. From Figures 8.4 and 8.5 it can be seen that the relative density distribution of a compact with magnesium stearate is more uniform when compared to a formulation without lubricant, for the 25% and 50% pre-pick cases. The effect of lubricant for the 0% pre-pick case is less obvious. Small amounts of lubricant improves particle rearrangement, thus decreasing density gradients [67]. This behavior can be observed in the DPC material properties. Adding a small amount of magnesium stearate decreases the hydrostatic yield stress for the compact at large relative densities.

The relative density fields were found to vary little in the region of the deboss-
ments as the friction coefficient varied. A region of relative density smaller than the
mean appears in a region at the bottom of the compact near the die wall in all of the
simulations (not seen in Figure 8.4 & 8.5), which is typical of a compact formed via
uniaxial compaction with a stationary bottom punch. The size of this low relative
density region increases as the friction coefficient increases, consistent with the ex-
perimental observations of others, e.g., Sinka et al. [60] and Briscoe and Rough [141].
However, this region did not extend to the debossment region and thus had little
effect on the results discussed previously. FEM simulations were also performed to
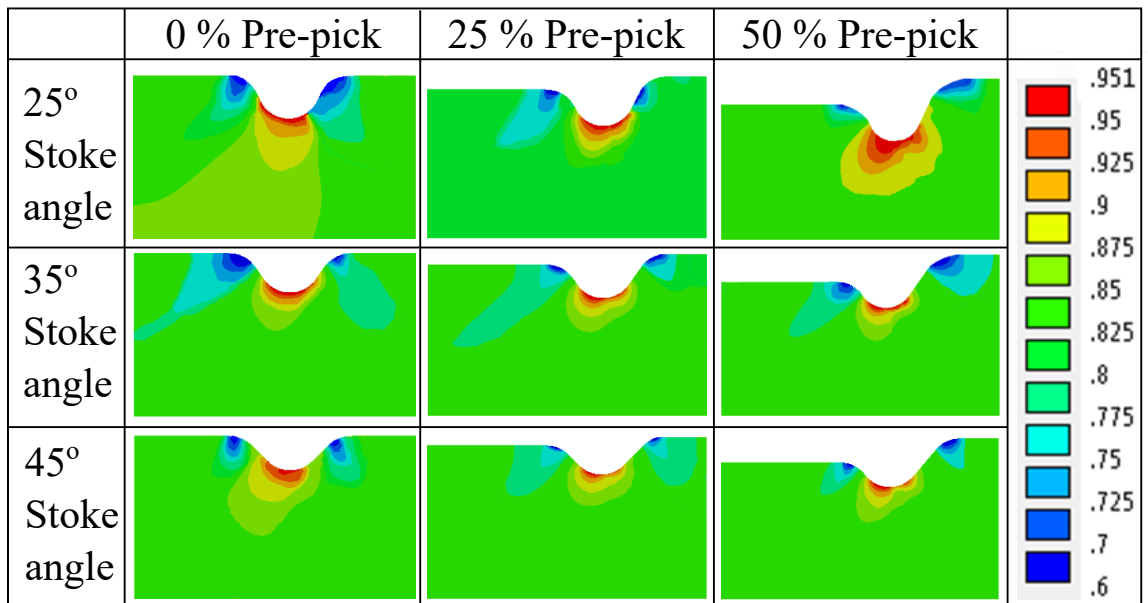
Figure 8.5.   FEM predictions of relative density fields for different
stroke angles (rows) and degrees of pre-pick (columns). All of these
simulations are for the lubricated formulation. Figure shows the re-
gion around the debossed feature and not the entire compact.

investigate the influence of the powder-tooling friction coefficient. In these simula-
tions, the formulations remained the same, but the powder-tooling friction coefficient
had values of 0.05, 0.1, and 0.2. Recall that the unlubricated tooling in the FEM

simulations had friction coefficients of 0.0964 and 0.0786 for the unlubricated and lubricated formulations, respectively.

	0 % Pre-pick	25 % Pre-pick	50 % Pre-pick
25° Stoke angle			
35° Stoke angle			
45° Stoke angle			
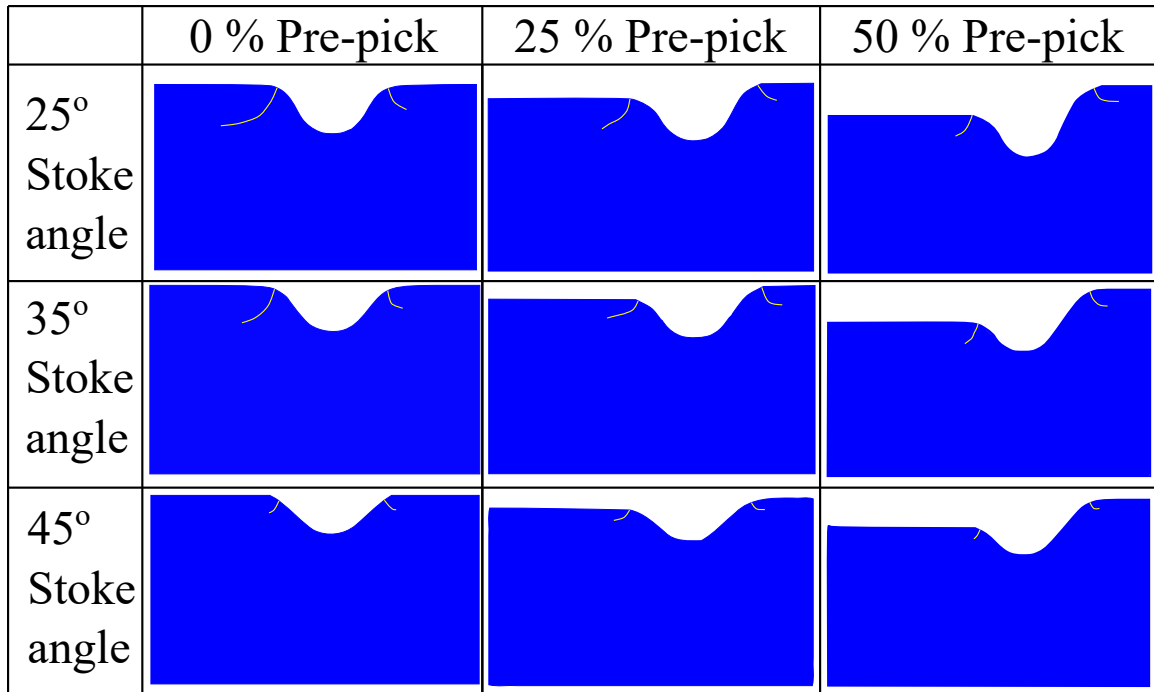
Figure 8.6. FEM predictions of crack initiation and growth for different stroke angles (rows) and degree of pre-pick (columns). All of the simulations are for the unlubricated formulation. The yellow line shows the crack in each figure.

8.4 Crack Initiation and Growth in Powder compacts

Figures 8.6 and 8.7 show the influence of stroke angle (rows) and pre-pick (columns) on crack initiation and growth in the compact for un-lubricated and lubricated formulations respectively. The images in these figures have been cropped in a consistent manner to facilitate comparison. In these images the yellow line represents the crack. Larger degrees of pre-pick and larger stroke angle clearly produce compacts with smaller crack. In general, cracks originate in the shoulders of the feature or the re-

|	0 % Pre-pick	25 % Pre-pick	50 % Pre-pick
25° Stoke angle			
35° Stoke angle			
45° Stoke angle			
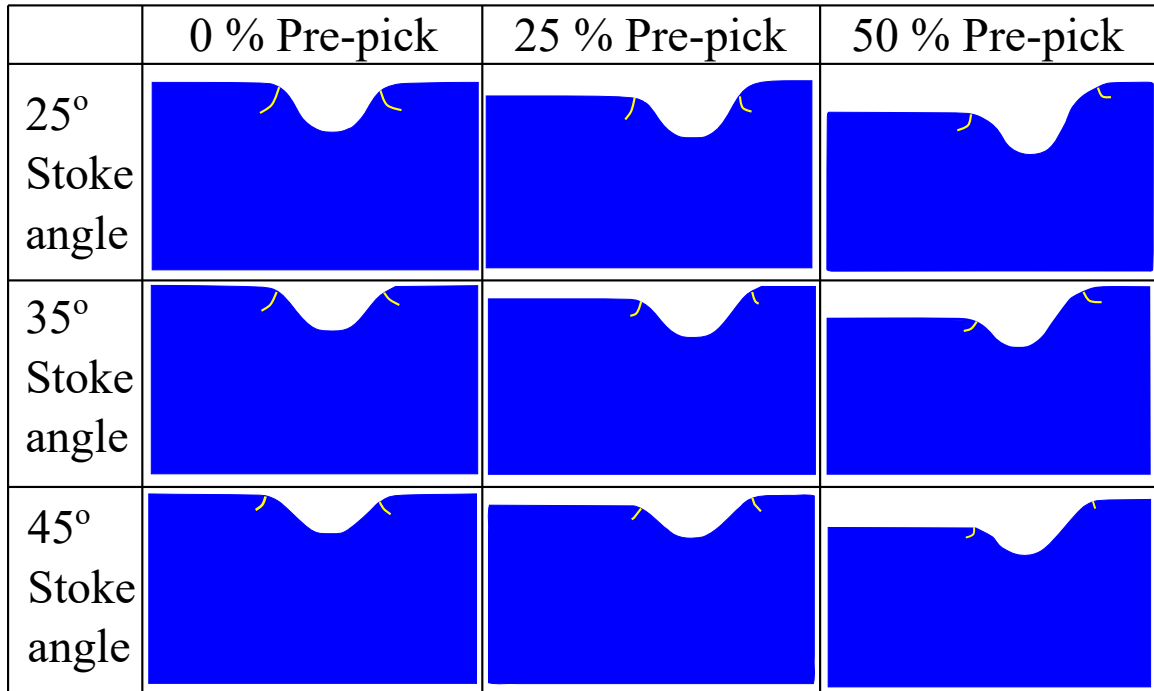
Figure 8.7. FEM predictions of crack initiation and growth for different stroke angles (rows) and degree of pre-pick (columns). All of the simulations are for the lubricated formulation. The yellow line shows the crack in each figure.

gions of smaller relative density and propagate towards the top of the compact. It is interesting to note that length of the crack for the compacts with MgSt or lubricated formulation compacts are always smaller than the unlubricated cases. This can be explained by the smaller values of the adhesive interaction force between the punch face and the powder bed for the lubricated formulation. As aforementioned earlier the length of the crack in the compact will depend on the mesh density and thus quantitative comparisons of the crack length with experimental compacts should be done cautiously. However if the mesh density is the same (as in this case) for all the cases examined then the crack length could be used for qualitative comparisons. Note that the crack initiation and growth only occurred when the adhesive interaction between the punch face and powder compact was specified. Thus modeling the adhesion

behavior between tooling and powder compact is a vital component for modeling the picking behavior. However this could also be seen as a limitation of this approach.

8.5   The Effect of the Adhesive Traction on Crack Growth
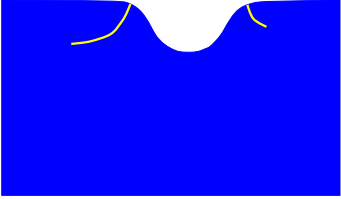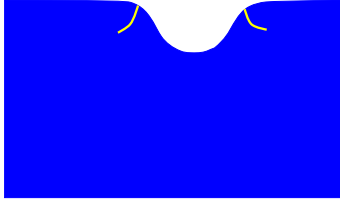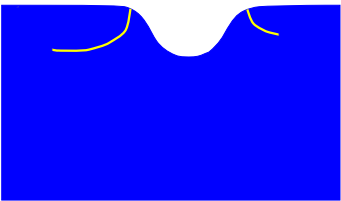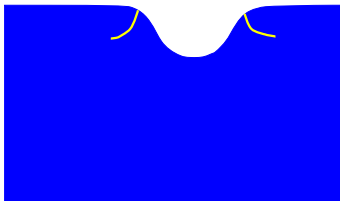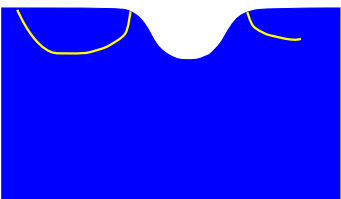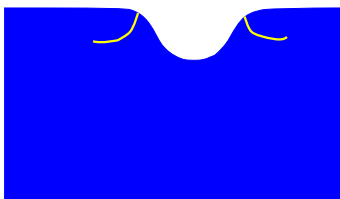
	Unlubricated (w/o MgSt)	Lubricated (with MgSt)
Experimentally Measured Adhesion		
2 x Experimentally Measured Adhesion		
4 x Experimentally Measured Adhesion		

Figure 8.8.   The effect of increasing the peak adhesive traction on crack growth for the lubricated and unlubricated formulations. The yellow line in the figure represents the crack.

One of the drawbacks with the adhesion punch developed in this work is that the actual area of contact between the adhesion punch and powder compact is unknown. Thus, one of the assumptions made in the current work is that the entire compact
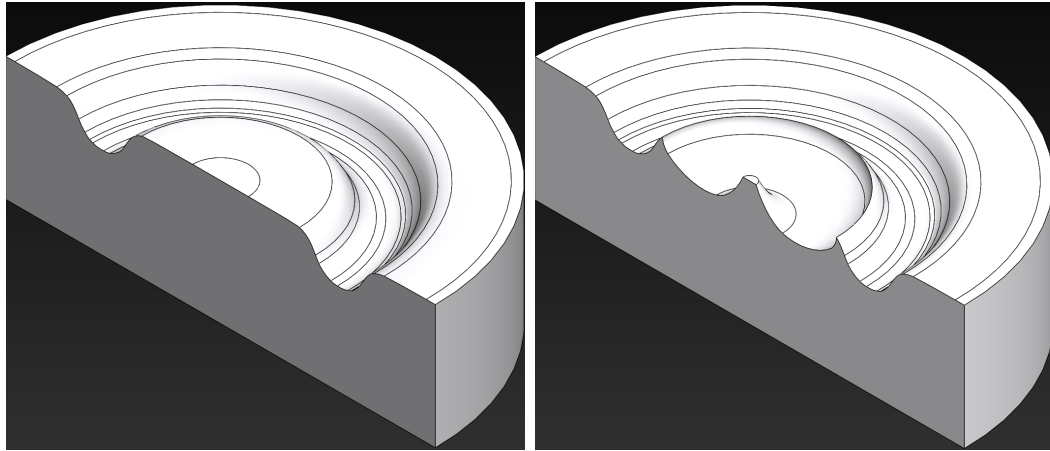
(a) Perfectly transferred debossed feature.   (b) Picked debossed feature.

Figure 8.9.   3D model rendered for the 0% pre-pick and 25 degree stroke angle debossed feature.

is in contact with the punch face during the detachment phase (failure zone) of the adhesion punch (Figure 4.5). However, from past experiences this is known to be inaccurate. In reality the area of contact would change in the failure zone as the compact detaches from the punch face. As a result, the adhesive traction experienced by the punch would be larger that the value used in the FEM simulations. Furthermore, picking behavior was observed in the 0% prepick and 25 degree stroke angle experimentally produced compacts for the unlubricated blend as seen in Figure 7.1 which was not observed in the simulation since the cracks in the simulation propagated into the bulk of the compact and not towards an edge. A exploratory study was performed to see if picking would be observed for a larger values of adhesive traction. In the FEM simulations the peak adhesive traction was increased by a factor for all the solid fraction. Note that the growth and failure displacements were not altered and kept same as the experimentally measured displacement for all the cases. The results of this study are shown in Figure 8.8. for the lubricated and unlubricated blends. The analysis was performed for the 0% pre-pick and 25° debossed geometry. The crack in Figure 8.8 is shown using a yellow solid line. It is clear that the crack propa-

gation is greater for the unlubricated blend in comparison to the lubricated blend. Thus, the addition of small amounts of lubricant in the form of MgSt was effective in inhibiting crack growth for the formulation considered in this study. When the adhesive traction is increased to 400% the experimentally measured adhesion the crack starts at the shoulder of the debossed feature and propagates back to the top edge of the compact. It would be fair to conclude from this simulation that the area of the compact bound between the top edge of the compact, the shoulder of the debossed feature and the crack would be the area that would undergo "picking". To better visualize the picked region 3D CAD models of the expected and picked debossed feature were rendered (Figure 8.9). The 3D model of the debossed for with picking was rendered by revolving the output of the 2D slice from the '4 $\times$ experimentally measured adhesion' simulations.

8.6   Summary

A methodology has been presented to predict picking in tablet compacts. The first study verifies the framework by comparing the results from the FEM simulation to experiments. The parametric study helped recognize the regions of the compact most susceptible to picking. The simulations verified an anecdotally known fact that the shoulders of the debossed feature were most susceptible to picking. The parametric study also demonstrated the power of the FEM simulation by predicting the residual stress in the vicinity of the debossed feature which is extremely difficult to determine experimentally. The FEM simulations could thus be used to design better powder compaction tooling to minimize residual stresses. Further it was show that the FEM simulations in conjunction with CAD modeling could be used to better visualize the geometry of the debossed feature on the compact.

9. CONCLUSIONS

9.1 Summary of Results

The primary objective of this work was to develop a framework to predict picking behavior in powder compacts. As a part of this work a efficient computational approach with FEM was developed to model picking as an alternative to performing labor intensive and time consuming experiments. The model was validated against several experimental measurements of a debossed feature, including the features stroke angle and stroke depth, as well as the extents of the relative density distribution.

This dissertation work required the measurement of the modified-DPC material parameters to calibrate the FEM model which led to the development of the Purdue in-house compaction simulator (PICS). The details of the construction and measurement protocol for the simulator are given in Chapter 3. Material parameter data obtained from PICS were validated against data from prior studies. The scripts used
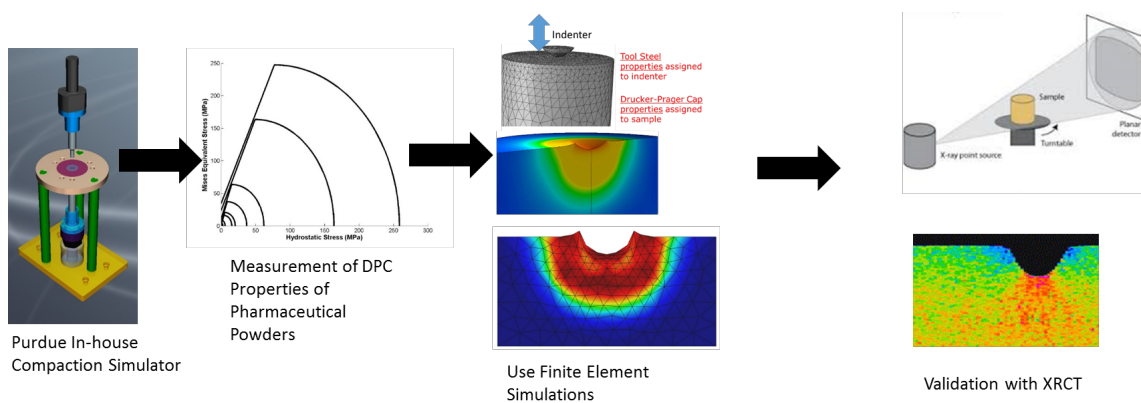
Figure 9.1. Graphical summary of the dissertation.

to extract the modified-DPC parameters from the experimental data have been provided in the appendix.

To model the picking in powder tablets it was essential to quantitatively understand the adhesive interaction between the punch face and the powder compact. A novel adhesion punch was developed in this study to characterize the adhesive interaction. The adhesive punch provided detailed traction displacement information of the adhesive interaction phenomenon and provided incite about the effect of lubrication on the adhesive interaction. The dependence of the adhesive interaction on the solid fraction of the compact was also examined in this work. An brief description of the design and construction of the adhesion punch as well as the measurement protocol is provided in Chapter 4.

The crack initiation and growth in the FEM model which leads to picking was modeled using a fracture mechanics approach. The 3-point single edge notch bend test in conjunction with FEM back-fitting (also known as 'inverse FEM') was used to determine the fracture toughness of the powder compacts. The fracture toughness of the compact was measured for a range of solid fractions. The rationale behind using FEM sub-modeling and FEM back-fitting to determine the fracture toughness is provided in Chapter 5

The FEM modeling framework used in this work is discussed in-depth in Chapter 6. The FEM model used in this work was divided in two parts with one model for to define the loading simulation and a sub-model for the unloading simulation. The material properties from Chapters 3 and 5 and interaction parameters from 4 were used to define the FEM model. Note that all these properties were measured in-house experimentally. A parametric study was performed in FEM to understand the effects of debossed feature geometry and blend lubrication on picking. The results of the parametric study are presented in Chapter 8. The parametric studies using the FEM model showed that the stroke angle, degree of pre-pick and blend lubrication significantly influenced picking behavior. The cracks always formed in the shoulder of the debossed compact in the low density regions. The crack growth was always

smaller in the lubricated blends. It was observed that the crack initiation and growth did not occur in the absence of the adhesive surface interaction model. This can be seen as a limitation of the model.

The parametric studies also revealed that the stroke angle and pre-pick also affected the debossed feature dimensions, with larger degrees of pre-pick and stroke angles giving debossed features that more closely match the target (embossment) values while lubrication plays a much weaker role, at least for the formulations considered here, but did improve the fidelity of the debossed feature slightly. Differences between the debossed and target feature dimensions are due to elastic spring back of the material. The FEM model also shows that the relative density is smallest at the shoulders of the debossed feature and largest at the base of the valley. Although the relative density fields show no obvious trends with stroke angle, the fields are clearly more uniform as the degree of pre-pick increases. The addition of lubricant to the formulation also improves the relative density field uniformity, at least for larger degrees of pre-pick. These results suggest that to improve feature fidelity and decrease the likelihood of damage, larger pre-picks, larger stroke angles, and the addition of a formulation lubricant should be used.

To experimentally validate the FEM results XRCT followed by image-processing was used in this work. The calibration protocol for the XRCT to get the local solid fraction in the compact is provided in Chapter 7. Although XRCT provided qualitative validation of the FEM simulations it was of interest to do some quantitative comparisons for debossed feature dimensions. This quantitative validation was done using image-processing. Results of the qualitative and quantitative comparison as presented in Section 8.2.

In conclusion the FEM simulation is able to provide accurate information of debossed feature geometry even without a fracture model. In conjunction with a fracture model the FEM simulations can provide incite into crack initialization and growth. This could be used as a tool in improving the formulation to alleviate picking problems. It can also be used to design and develop better powder compaction tooling.

In the next section we highlight some of the key contributions of this work.

9.2   Thesis Contributions

The key contributions of the current work can be summarized as follows

- Development of Purdue in-house compaction simulator to measure the DPC material properties.

- Developed a novel methodology to measure the adhesive interaction between the powder bed and tablet.

- Developed a protocol to get the fracture toughness of the powder compacts using inverse FEM and 3-point single edge notch bend test.

- Developed a novel framework in FEM to model picking in pharmaceutical compacts.

- Development of XRCT and image-processing tools to experimentally validate the FEM model results.

10. RECOMMENDATIONS FOR FUTURE WORK

10.1 Improvements to the Adhesion Punch

The adhesive punch in the current study did not characterize the contact area during the detachment phase of the adhesive contact. Thus, the powder was assumed to be in contact with the complete punch face till detachment. In reality the punch powder contact area would change in the detachment phase. Thus the value of adhesive traction used in this study could be an under-estimation. In future works it may be useful to develop an adhesion punch capable of mapping the exact contact area between the punch face and powder bed. This could be accomplished with some image based technique with a transparent punch made or by using a pressure sensitive punch face that capable of measuring local loads on the punch face to get a better idea of the area of contact between the punch face and powder compact. In the current design of the adhesion punch the size of the punch face is fixed at 10 mm. It would be useful to have a detachable punch face to study the influence of the contact area on the adhesive interaction. In the current work the pull out force was measured for a maximum of five compression cycles. However, it is well know that picking is a phenomenon that exacerbates over time. It would be of interest to study the adhesive interaction between the punch face and the powder compact for large number of compression cycles.

10.2 Improvements to the FEM Model

The constitutive relations used in this approach are phenomenological in nature which require complex time consuming experiments to characterize the material behavior. The effect of particle size, shape, density on compaction is not well understood since there are no first principle physics models for powder compaction of granular

materials. Similarly the models used for the adhesive interaction between the powder compact and punch face and also phenomenological in nature. This could be a value area for future contributions.

In the current study we use a constant velocity profile with no dwell. The DPC constitute model used in the current work is a quasi-static model. Thus it cannot capture the effects of the compression profile on the tablet compaction process. It would be interest to extend the DPC model to be able to capture strain-rate effects. A constitutive model that can capture the strain rate effects can be used to study the effect of the compression velocity profile, dwell time on picking and sticking. Some of the compression profiles commonly used in industry are sinusoidal compression profile, constant density reduction compression profile, saw tooth profile.

The current has demonstrated that FEM is a useful tool to model pricking behavior in powder compacts. The FEM model can accurately capture the compaction process to provide debossed feature dimensions. The FEM parametric studies showed the importance of formulation as well as process parameters. I would be useful to develop a tool which could optimize the punch design to mitigate picking problems and/or provide better dimensional fidelity based on the application. An effective approach would be to use the optimization module in Abaqus to improve the design of the debossed features on the punch face iteratively.

The current study was also restricted to cylindrical flat faced tablets. In reality most pharmaceutical tablets have complex shapes like biconvex, almond shape, capsule shape etc. 3D simulation for these complex shapes with debossed feature can provide incite on the influence of debossed feature location on picking. It would be interesting to vary the location of the debossed feature on the surface of a biconvex tablet while simultaneously varying the curvature of the tablet.

The present work was restricted to 2D simulations due to computational limitations. Although valuable insight can be gained from 2D simulations the mechanics of crack growth in 3D would be much more complex. This may also require the alteration of some of the fracture mechanical assumptions used in the FEM model.

With computational resources constantly improving it could be possible to model the compaction process using multi-particle FEM (MPFEM) approach. MPFEM provides greater flexibility in modeling powder mixtures instead of using a lumped approach as chosen in the current work. The use of fracture models in the MPFEM framework may provide better understanding of crack initiation and growth in pharmaceutical tablets. Another feasible approach to model the compaction of multi-component powder mixtures would be using discrete element method with non-local contact force models to account for the large deformations. This approach is currently extremely computationally expensive and only practical for static or quasi-static systems.

10.3 Experimental Validation of Crack initiation and Growth in Pharmaceutical Tablets

In this work the crack initiation and growth predicted using FEM were not validated. It would be useful to develop techniques that could visualize the initiation and growth of the cracks real-time in or on the powder compact. This would also aid in selection of appropriate crack initiation and growth criteria in the FEM model.

In this work the temperature and humidity were measured but not controlled. It would be useful to do a rigorous analysis on the effects of temperature and humidity on the powder compaction process as a whole as well as its effects on individual material and interaction parameters.

To summarize, the avenues for immediate future work are:

- Development of first principle physics model to better understand powder compaction for granular material.

- Use the optimization tools (iSight) in Abaqus to improve tooling design and debossed feature geometry.

- Use the optimization tools in Abaqus to find the best location for the debossed feature on the pharmaceutical tablet.

- Extend the simulation framework to 3D to model complex tablet shapes.

- Experimental validation of crack initiation and growth in the powder compacts.

- Looking at the effect of compression velocity profiles on the picking and sticking phenomenon.

LIST OF REFERENCES

LIST OF REFERENCES

[1] L. Lachman, H. A. Lieberman, and J. L. Kanig. *The theory and practice of industrial pharmacy*. Lea & Febiger, 1986.

[2] J. J. Wang. *Modeling of Adhesion in Tablet Compression*. PhD thesis, Purdue University, 4 2002.

[3] M. P. Mullarney and B.C. Hancock. Mechanical property anisotropy of pharmaceutical excipient compacts. *International journal of pharmaceutics*, 314(1):9–14, 5 2006.

[4] T. Sinha. *Investigation of Compaction, Youngs Modulus and Tensile Strength of Binary Powder Mixtures Using the Multi-Particle Finite Element Method (MPFEM)*. PhD thesis, Purdue University, 2011.

[5] T. Sinha, R. Bharadwaj, J. S. Curtis, B. C. Hancock, and C. Wassgren. Finite element analysis of pharmaceutical tablet compaction using a density dependent material plasticity model. *Powder Technology*, 202(1-3):46–54, 8 2010.

[6] S. M. Razavi, M. Gonzalez, and A. M. Cuitiño. General and mechanistic optimal relationships for tensile strength of doubly convex tablets under diametrical compression. *International Journal of Pharmaceutics*, 484(1-2):29–37, 2015.

[7] S. Otoguro, Y. Hayashi, T. Miura, N. Uehara, S. Utsumi, Y. Onuki, Y. Obata, and K. Takayama. Numerical Investigation of the Residual Stress Distribution of Flat-faced and Convexly Curved Tablets using the Finite Element Method. *Chemical & Pharmaceutical Bulletin*, 63(11):890–900, 2015.

[8] I. Saniocki. *New Insights into Tablet Sticking : Characterization and Quantification of Sticking to Punch Surfaces during Tablet Manufacture by Direct Compaction*. PhD thesis, Universität Hamburg, 2014.

[9] F. Waimer, M. Krumme, P. Danz, U. Tenter, and P. C. Schmidt. A Novel Method for the Detection of Sticking of Tablets. *Pharmaceutical Development and Technology*, 4(3):359–367, 1 1999.

[10] L. H. Han, P. R. Laity, R. E. Cameron, and J. A. Elliott. Density and plastic strain evaluations using small-angle X-ray scattering and finite element simulations for powder compacts of complex shape. *Journal of Materials Science*, 46(18):5977–5990, 2011.

[11] Manual of Policies and Procedures: Scoring Configuration of Generic Drug Products (5223.2). Technical report, Center of Drug Evaluation and Research, FDA, Center for Drug Evaluation and Research, Food and Drug Administration., 2012.

[12] Guidance for Industry Tablet Scoring : Nomenclature , Labeling , and Data for Evaluation. Technical Report March, U.S. Department of Health and Human Services Food and Drug Administration, Center for Drug Evaluation and Research (CDER), CMC, Silver Spring, MD, 2013.

[13] A. R. Muliadi, J. D. Litster, and C. R. Wassgren. Modeling the powder roll compaction process: Comparison of 2-D finite element method and the rolling theory for granular solids (Johanson's model). *Powder Technology*, 221:90–100, 5 2012.

[14] A. R. Muliadi, J. D. Litster, and C. R. Wassgren. Validation of 3-D finite element analysis for predicting the density distribution of roll compacted pharmaceutical powder. *Powder Technology*, 237:386–399, 3 2013.

[15] I. C. Sinka and A. C. F. Cocks. Constitutive modelling of powder compaction II. Evaluation of material data. *Mechanics of Materials*, 39(4):404–416, 4 2007.

[16] G. E. Klinzing, F. Rizk, R. Marcus, and L. S. Leung. *Pneumatic Conveying of Solids: A theorical and practical approach.* 2010.

[17] Dassault Systemes: Abaqus. *Writing User Subroutine with Abaqus.* 2013.

[18] J. C. Cunningham, D. Winstead, and A. Zavaliangos. Understanding variation in roller compaction through finite element-based process modeling. *Computers & Chemical Engineering*, 34(7):1058–1071, 7 2010.

[19] A. Michrafy, H. Diarra, J. A. Dodds, and M. Michrafy. Experimental and numerical analyses of homogeneity over strip width in roll compaction. *Powder Technology*, 206(1-2):154–160, 1 2011.

[20] J. C. Cunningham, I. C. Sinka, and A. Zavaliangos. Analysis of tablet compaction. I. Characterization of mechanical behavior of powder and powder/tooling friction. *Journal of pharmaceutical sciences*, 93(8):2022–39, 8 2004.

[21] Y. Liu and C. R. Wassgren. Modifications to Johanson's roll compaction model for improved relative density predictions. *Powder Technology*, 297:294–302, 2016.

[22] I. C. Sinka, J. C. Cunningham, and A. Zavaliangos. The effect of wall friction in the compaction of pharmaceutical tablets with curved faces: a validation study of the DruckerPrager Cap model. *Powder Technology*, 133(1-3):33–43, 7 2003.

[23] H. Diarra, V. Mazel, V. Busignies, and P. Tchoreloff. FEM simulation of the die compaction of pharmaceutical products: Influence of visco-elastic phenomena and comparison with experiments. *International Journal of Pharmaceutics*, 453(2):389–394, 2013.

[24] C. Y. Wu, O. M. Ruddy, A. C. Bentham, B. C. Hancock, S. M. Best, and J. A. Elliott. Modelling the mechanical behaviour of pharmaceutical powders during compaction. *Powder Technology*, 152(1-3):107–117, 4 2005.

[25] T. Sinha, J. S. Curtis, B. C. Hancock, and C. Wassgren. A study on the sensitivity of DruckerPrager Cap model parameters during the decompression phase of powder compaction simulations. *Powder Technology*, 198(3):315–324, 3 2010.

[26] S. Garner, J. Strong, and A. Zavaliangos. The extrapolation of the Drucker-Prager/Cap material parameters to low and high relative densities. *Powder Technology*, 283:210–226, 2015.

[27] G. S. Wagle. *Die Compaction Simulation: Simplifying the Application of a Complex Constitutive Model Using Numerical and Physical Experiments.* PhD thesis, The Pennsylvania State University, 2006.

[28] 2005 Tableting Specification Manual. *Tableting Specification Manual.* American Pharmacists Association, 7th edition, 2005.

[29] F. Waimer, M. Krumme, P. Danz, U. Tenter, and P. C. Schmidt. The influence of engravings on the sticking of tablets. Investigations with an instrumented upper punch. *Pharmaceutical development and technology*, 4(3):369–75, 8 1999.

[30] M. Roberts, J. L. Ford, G. S. MacLeod, J. T. Fell, G. W. Smith, P. H. Rowe, and a Mark Dyas. Effect of punch tip geometry and embossment on the punch tip adherence of a model ibuprofen formulation. *Journal of Pharmacy and Pharmacology*, 56(7):947–950, 7 2004.

[31] P. R. Laity. Effects of punches with embossed features on compaction behaviour. *Powder Technology*, 254:373–386, 2014.

[32] M. Roberts, J. L. Ford, G. S. MacLeod, J. T. Fell, G. W. Smith, and P. H. Rowe. Effects of surface roughness and chrome plating of punch tips on the sticking tendencies of model ibuprofen formulations. *The Journal of pharmacy and pharmacology*, 55(9):1223–8, 9 2003.

[33] T. Uchimoto, Y. Iwao, T. Yamamoto, K. Sawaguchi, T. Moriuchi, S. Noguchi, and S. Itai. Newly developed surface modification punches treated with alloying techniques reduce sticking during the manufacture of ibuprofen tablets. *International journal of pharmaceutics*, 441(1-2):128–34, 1 2013.

[34] K. Reed, C. Davies, and K. Kelly. Tablet sticking: Using a 'compression toolbox' to assess multiple tooling coatings options. *Powder Technology*, 285:103–109, 2015.

[35] Tsiftsoglou T. B. and R. W. Mendes. Effect of boron alloy coating of tableting tools. *Pharmaceutical Technology*, 6:30–32, 1982.

[36] S. Schumann and G. D. Searle. The Effect of Chromium Nitride Ion Bombardment Treatment of Tablet Tooling on Tablet Adherence. *Drug development and industrial pharmacy*, 18(10):1037–1061, 1992.

[37] W. A. Strickland, E. Nelson, L. W. Busse, and T. Higuchi. The physics of tablet compression IX. Fundamental aspects of tablet lubrication. *Journal of the American Pharmaceutical Association*, 45(1):51–55, 9 1956.

[38] A. M. N. Faqih, A. Mehrotra, S. V. Hammond, and F. J. Muzzio. Effect of moisture and magnesium stearate concentration on flow properties of cohesive granular materials. *International Journal of Pharmaceutics*, 336:338–345, 2007.

[39] J. J. Wang, M. A. Guillot, S. D. Bateman, and K. R. Morris. Modeling of adhesion in tablet compression. II. Compaction studies using a compaction simulator and an instrumented tablet press. *Journal of pharmaceutical sciences*, 93(2):407–17, 2 2004.

[40] S. Likitlersuang. *The Influence Of Magnesium Stearate On Pharmaceutical Powder Consolidation.* PhD thesis, The University of Iowa, 2004.

[41] A. H. Sameh and G. Betz. A novel tool for the prediction of tablet sticking during high speed compaction. *Pharmaceutical development and technology*, 7450(March):1–8, 2011.

[42] A. Sabir, B. Evans, and S. Jain. Formulation and process optimization to eliminate picking from market image tablets. *International Journal of Pharmaceutics*, 215(1-2):123–135, 3 2001.

[43] K. B. Shah, L. L. Augsburger, and Ralph F. Shangraw. Effect of boron alloy coating of tableting tools. *Pharmaceutical Technology*, 6:31 – 34, 1982.

[44] R. J. Roberts and R. C. Rowe. Brittle/ductile behaviour in pharmaceutical materials used in tabletting. *International Journal of Pharmaceutics*, 36(2-3):205–209, 5 1987.

[45] M Pedersen. Tablet tooling: design, maintenance and troubleshooting. *Pharmaceutical Technology Europe*, 2:22–28, 1999.

[46] M. P. Mullarney, B. C. MacDonald, and A. Hutchins. Assessing Tablet- Sticking Propensity. *Pharmaceutical Technology*, 36(1):57, 2012.

[47] J. Dawes, J. F. Gamble, R. Greenwood, P. Robbins, and M. Tobyn. An investigation into the impact of magnesium stearate on powder feeding during roller compaction. *Drug development and industrial pharmacy*, 38(1):111–22, 1 2012.

[48] B. van Veen, G. K. Bolhuis, Y. S. Wu, K. Zuurman, and H. W. Frijlink. Compaction mechanism and tablet strength of unlubricated and lubricated (silicified) microcrystalline cellulose. *European journal of pharmaceutics and biopharmaceutics : official journal of Arbeitsgemeinschaft für Pharmazeutische Verfahrenstechnik e.V*, 59(1):133–8, 1 2005.

[49] M. Otsuka, I. Yamane, and Y. Matsuda. Effects of lubricant mixing on compression properties of various kinds of direct compression excipients and physical properties of the tablets. *Advanced Powder Technology*, 15(4):477–493, 7 2004.

[50] Z. Huang, J. V. Scicolone, L. Gurumuthy, and R. N. Davé. Flow and bulk density enhancements of pharmaceutical powders using a conical screen mill: A continuous dry coating device. *Chemical Engineering Science*, 125:209–224, 3 2015.

[51] F. W. Goodhart, G. Mayorga, and F. C. Ninger. Measurement of Lower Punch Pulldown Force and its Significance. *Journal of Pharmaceutical Sciences*, 58(2):248–251, 2 1969.

[52] D. C. Drucker. Limit analysis of two and three dimensional soil mechanics problems. *Journal of the Mechanics and Physics of Solids*, 1(4):217–226, 1953.

[53] A. N. Schofield. *Critical State Soil Mechanics.* McGraw-Hill, New York, 1930.

[54] R. J. Green. A plasticity theory for porous solids. *International Journal of Mechanical Sciences*, 14(4):215–224, 4 1972.

[55] F. L. DiMaggio and I. S. Sandler. Material Model for Granular Soils. *Journal of Engineering Mechanics*, 97(3):935–950, 1971.

[56] A. L. Gurson. Continuum Theory of Ductile Rupture by Void Nucleation and Growth: Part IYield Criteria and Flow Rules for Porous Ductile Media. *Journal of Engineering Materials and Technology*, 99(1):2, 1977.

[57] T. Kraft and H. Riedel. Numerical simulation of die compaction and sintering. *Powder Metallurgy*, 45(3):227–231, 10 2002.

[58] P. Brewin, O. Coube, P. Doremus, and J. H. Tweed. *Modelling of Powder Die Compaction.* 2007.

[59] W.F . Chen and G. Y. Baladi. *Soil Plasticity: Theory and Implementation.* Elesveir, New York, NY, 1985.

[60] I. C. Sinka, S. F. Burch, J. H. Tweed, and J. C. Cunningham. Measurement of density variations in tablets using X-ray computed tomography. *International Journal of Pharmaceutics*, 271(1-2):215–224, 3 2004.

[61] E. Emery, J. Oliver, T. Pugsley, J. Sharma, and J. Zhou. Flowability of moist pharmaceutical powders. *Powder Technology*, 189(3):409–415, 2009.

[62] E. Teunou and J. J. Fitzpatrick. Effect of relative humidity and temperature on food powder flowability. *Journal of Food Engineering*, 42:109–116, 1999.

[63] G. E. Amidon and M. E. Houghton. The effect of moisture on the mechanical and powder flow properties of microcrystalline cellulose., 1995.

[64] J. J. Fitzpatrick, T. Iqbal, C. Delaney, T. Twomey, and M. K. Keogh. Effect of powder properties and storage conditions on the flowability of milk powders with different fat contents. *Journal of Food Engineering*, 64:435–444, 2004.

[65] A. T. Procopio, A. Zavaliangos, and J. C. Cunningham. Analysis of the diametrical compression test and the applicability to plastically deforming materials. *Journal of Materials Science*, 38(17):3629–3639, 2003.

[66] H. Awaji and S. Sato. Diametral Compressive Testing Method. *Journal of Engineering Materials and Technology*, 101(2):139, 1979.

[67] L. H. Han, J. A. Elliott, A. C. Bentham, A. Mills, G. E. Amidon, and B. C. Hancock. A modified Drucker-Prager Cap model for die compaction simulation of pharmaceutical powders. *International Journal of Solids and Structures*, 45(10):3088–3106, 5 2008.

[68] A. Michrafy, D. Ringenbacher, and P. Tchoreloff. Modelling the compaction behaviour of powders: application to pharmaceutical powders. *Powder Technology*, 127(3):257–266, 11 2002.

[69] K. Zuurman, K. Van der Voort Maarschalk, and G.K. Bolhuis. Effect of magnesium stearate on bonding and porosity expansion of tablets produced from materials with different consolidation properties. *International Journal of Pharmaceutics*, 179(1):107–115, 3 1999.

[70] J. J. Wang, H. Wen, and D. Desai. Lubrication in tablet formulations. *European journal of pharmaceutics and biopharmaceutics : official journal of Arbeitsgemeinschaft für Pharmazeutische Verfahrenstechnik e.V*, 75(1):1–15, 5 2010.

[71] S. Yu, M. Adams, B. Gururajan, G. Reynolds, R. Roberts, and C. Y. Wu. The effects of lubrication on roll compaction, ribbon milling and tabletting. *Chemical Engineering Science*, 86:9–18, 2 2013.

[72] K. LaMarche, D. Buckley, R. Hartley, F. Qian, and S. Badawy. Assessing materials' tablet compaction properties using the DruckerPrager Cap model. *Powder Technology*, 267:208–220, 11 2014.

[73] S. W. Booth and J. M. Newton. Experimental investigation of adhesion between powders and surfaces. *Journal of Pharmacy and Pharmacology*, 39(9):679–684, 9 1987.

[74] E. M. Lifshitz. The Theory of Molecular Attractive Forces between Solids. *Soviet Physics*, 2(1):73 – 83, 1956.

[75] K. K. Lam and J. M. Newton. Influence of particle size on the adhesion behaviour of powders, after application of an initial press-on force. *Powder Technology*, 73(2):117–125, 12 1992.

[76] A. Khilnani. *Particles on Surface 1: Detection, Adhesion and Removal.* Springer, New York, NY, 1 edition, 1988.

[77] H. Rumpf. Particle Adhesion. In *Agglomeration 77: Proc. 2nd lnt. Symp. on Agglomeration,(KVS Sastry, Ed.), American Institute of Mining, Metallurgical, and Petroleum Engineers, New York*, 1977.

[78] C. Somboonvechakarn. *Effects of Particle Size and Density on Separation of Mixtures During Nonelectrostatic and Electrostatic Powder Coating.* PhD thesis, The Ohio State University, 2009.

[79] F. Podczeck. *Particle-particle Adhesion in Pharmaceutical Powder Handling.* Imperial College Press, London, 1st edition, 1998.

[80] D. Tabor and R. H. S. Winterton. Surface Forces: Direct Measurement of Normal and Retarded van der Waals Forces. *Nature*, 219(5159):1120–1121, 9 1968.

[81] M. Ohta, T. Konishi, Y. Sugawara, S. Morita, M. Suzuki, and Y. Enomoto. Observation of Atomic Defects on LiF(100) Surface with Ultrahigh Vacuum Atomic Force Microscope (UHV AFM). *Japanese Journal of Applied Physics*, 32(Part 1, No. 6B):2980–2982, 6 1993.

[82] N. A. Burnham. Measuring the nanomechanical properties and surface forces of materials using an atomic force microscope. *Journal of Vacuum Science & Technology A: Vacuum, Surfaces, and Films*, 7(4):2906, 7 1989.

[83] G. Meyer and N. M. Amer. Simultaneous measurement of lateral and normal forces with an optical-beam-deflection atomic force microscope. *Applied Physics Letters*, 57(20):2089, 1990.

[84] P. Grütter and U. T. Dürig. Growth of vapor-deposited cobalt films on Pt(111) studied by scanning tunneling microscopy. *Physical Review B*, 49(3):2021–2029, 1 1994.

[85] M. C. Thomas and S. P. Beaudoin. An enhanced centrifuge-based approach to powder characterization: Particle size and Hamaker constant determination. *Powder Technology*, 286:412–419, 12 2015.

[86] S. I. Naito and K. Nakamichi. Studies on techniques of manufacturing pharmacy. I. Prediction of tableting troubles such as capping and sticking. 1. *Chemical & pharmaceutical bulletin*, 17(12):2507–14, 12 1969.

[87] A. Mitrove and L. L. Augsburger. Adhesion of Tablets in a Rotary Tablet Press I. Instrumentation and Preliminary Study of Variables Affecting Adhesion. *Drug Development and Industrial Pharmacy*, 6(4):331–377, 1 1980.

[88] K. T. Mitrevej and L. L. Augsburger. Adhesion of Tablets in a Rotary Tablet Press II. Effects of Blending Time, Running Time, and Lubricant Concentration. *Drug Development and Industrial Pharmacy*, 8(2):237–282, 1 1982.

[89] A. Savitzky and M. J. E. Golay. Smoothing and Differentiation of Data by Simplified Least Squares Procedures. *Analytical Chemistry*, 36(8):1627–1639, 7 1964.

[90] K. Pingali, R. Mendez, D. Lewis, B. Michniak-Kohn, A. Cuitino, and F. Muzzio. Mixing order of glidant and lubricant–influence on powder and tablet properties. *International journal of pharmaceutics*, 409(1-2):269–77, 5 2011.

[91] A. U. Vanarase, J. G. Osorio, and F. J. Muzzio. Effects of powder flow properties and shear environment on the performance of continuous mixing of pharmaceutical powders. *Powder Technology*, 246:63–72, 2013.

[92] Y. K. Lam and J. M. Newton. Effect of temperature on particulate solid adhesion to a substrate surface. *Powder Technology*, 73(3):267–274, 12 1992.

[93] K. K. Lam and J. M. Newton. Investigation of applied compression on the adhesion of powders to a substrate surface. *Powder Technology*, 65(1-3):167–175, 3 1991.

[94] F. Podczeck. The influence of constant and changing relative humidity of the air on the autoadhesion force between pharmaceutical powder particles. *International Journal of Pharmaceutics*, 145(1-2):221–229, 12 1996.

[95] K. M. Lee. *The Effects Of Relative Humidity On Lactose Particle Adhesion*. PhD thesis, Purdue University, 2009.

[96] P. A. Gustafson and A. M. Waas. The influence of adhesive constitutive parameters in cohesive zone finite element models of adhesively bonded joints. *International Journal of Solids and Structures*, 46(10):2201–2215, 2009.

[97] S. C. Lee and K. T. Kim. A densification model for powder materials under cold isostatic pressing-Effect of adhesion and friction of rubber molds. *Materials Science and Engineering A*, 498(1-2):359–368, 2008.

[98] K. Park and G. H. Paulino. Cohesive Zone Models : A Critical Review of Traction-Separation Relationships Across Fracture Surfaces. *Applied Mechanics Reviews*, 64(November 2011):20, 2013.

[99] S. Naito, I. Shimizu, and S. Iwaki. Techniques for manufacturing pharmacy. II. Prediction of tableting troubles such as capping and sticking. 2. *Chemical & pharmaceutical bulletin*, 19(9):1949–56, 9 1971.

[100] N. Rasenack and B. W. Müller. Crystal habit and tableting behavior. *International Journal of Pharmaceutics*, 244(1-2):45–57, 2002.

[101] A. B. Mashadi and J. M. Newton. The characterization of the mechanical properties of microcrystalline cellulose: a fracture mechanics approach. *Journal of Pharmacy and Pharmacology*, 39(12):961–965, 12 1987.

[102] P. York, F. Bassam, R. C. Rowe, and R. J. Roberts. Fracture mechanics of microcrystalline cellulose powders. *International Journal of Pharmaceutics*, 66(1-3):143–148, 12 1990.

[103] R. J. Roberts. *The Elasticity, Ductility And Frracture Toughness Of Pharmaceutical Powders*. PhD thesis, University of Bradford, 1991.

[104] B. C. Hancock, S. D. Clas, and K. Christensen. Micro-scale measurement of the mechanical properties of compressed pharmaceutical powders. 1: The elasticity and fracture behavior of microcrystalline cellulose. *International journal of pharmaceutics*, 209(1-2):27–35, 2000.

[105] J. D. Anderson. Governing Equations of Fluid Dynamics. 2009.

[106] E. E. Gdoutos. *Fracture Mechanics An Introduction*, volume 123 of *Solid Mechanics and Its Applications*. Springer-Verlag, Berlin/Heidelberg, 2005.

[107] S. M. Tahir and A. K. Ariffin. Fracture in metal powder compaction. *International Journal of Solids and Structures*, 43(6):1528–1542, 2006.

[108] P. Jonsén, H.-. Häggblad, and G. Gustafsson. Modelling the non-linear elastic behaviour and fracture of metal powder compacts. *Powder Technology*, 284:496–503, 2015.

[109] J. T. Wang. Relating Cohesive Zone Models to Linear Elastic Fracture Mechanics. Technical Report May, Langley Research Center, Hampton, VA, 2010.

[110] X.-P. Xu and A. Needleman. Numerical simulations of fast crack growth in brittle solids. *Journal of the Mechanics and Physics of Solids*, 42(9):1397–1434, 9 1994.

[111] V. Tvergaard and J. W. Hutchinson. On the toughness of ductile adhesive joints. *Journal of the Mechanics and Physics of Solids*, 44(5):789–800, 5 1996.

[112] V. Tvergaard. Crack growth predictions by cohesive zone model for ductile fracture. 49:2191–2207, 2001.

[113] G. T. Camacho and M. Ortiz. Computational modelling of impact damage in brittle materials. *International Journal of Solids and Structures*, 33(20-22):2899–2938, 1996.

[114] G. Vigueras, F. Sket, C. Samaniego, L. Wu, L. Noels, D. Tjahjanto, E. Casoni, G. Houzeaux, A. Makradi, J. M. Molina-Aldareguia, M. Vázquez, and A. Jérusalem. An XFEM/CZM implementation for massively parallel simulations of composites fracture. *Composite Structures*, 125:542–557, 7 2015.

[115] B. Gross and J. E. Strawley. Stress-intensity factors for three-point bend specimens by boundary collocation. Technical report, Lewis Research Center, National Aeronautics and Space Administration, Cleveland OH, 1965.

[116] J. Jakobsen, J. H. Andreasen, and E. Bozhevolnaya. Crack kinking of a delamination at an inclined core junction interface in a sandwich beam. *Engineering Fracture Mechanics*, 75(16):4759–4773, 2008.

[117] F. Bassam, P. York, R. C. Rowe, and R. J. Roberts. The Young's modulus of binary powder mixtures. *Powder Technology*, 65(1-3):103–111, 3 1991.

[118] ASTM E1820-15A. Standard Test Method for Measurement of Fracture Toughness. Technical report, West Conshohocken, 2015.

[119] ASTM E399-12. Standard Test Method for Linear-Elastic Plane-Strain Fracture Toughness KIc of Metallic Materials. Technical report, West Conshohocken, 2012.

[120] B. C. Hancock, J. T. Colvin, M. P. Mullarney, and A. V. Zinchuk. The Relative Densities of Pharmaceutical Powders , Blends , Dry Granulations , and Immediate-Release Tablets. *Pharmaceutical Technology*, 27(April):64–80, 2003.

[121] R. D. S. G. Campilho, M. D. Banea, J. A. B. P. Neto, and L. F. M. Da Silva. Modelling adhesive joints with cohesive zone models: Effect of the cohesive law shape of the adhesive layer. *International Journal of Adhesion and Adhesives*, 44:48–56, 2013.

[122] *Abaqus 6.13 User Reference Manual.* 2013.

[123] W. X. Zhu. Singular stress field of three-dimensional crack. *Engineering Fracture Mechanics*, 36(2):239–244, 1990.

[124] F. Zhou and J. F. Molinari. Dynamic crack propagation with cohesive elements: A methodology to address mesh dependency. *International Journal for Numerical Methods in Engineering*, 59(1):1–24, 2004.

[125] J. Stolk, N. Verdonschot, K. A. Mann, and R. Huiskes. Prevention of mesh-dependent damage growth in finite element simulations of crack formation in acrylic bone cement. *Journal of Biomechanics*, 36(6):861–871, 2003.

[126] L. Farber, G. Tardos, and J. N. Michaels. Use of X-ray tomography to study the porosity and morphology of granules. *Powder Technology*, 132(1):57–63, 5 2003.

[127] V. Busignies, B. Leclerc, P. Porion, P. Evesque, G. Couarraze, and P. Tchoreloff. Quantitative measurements of localized density variations in cylindrical tablets using X-ray microtomography. *European journal of pharmaceutics and biopharmaceutics : official journal of Arbeitsgemeinschaft für Pharmazeutische Verfahrenstechnik e.V*, 64(1):38–50, 8 2006.

[128] A. C. Kak. Computerized Tomography with X-Ray, Emission, and Ultrasound Sources. *Proceedings of the IEEE*, 67(9):1245–1272, 1979.

[129] T. J. Davis. Effect of Temperature Cycling and High Temperature Aging on the Elastic Properties and Failure Modes of Thermal Interface Materials. *Proceedings of the ASME 2015 International Technical Conference and Exhibition on Packaging and Integration of electronic and Photonic microsystems*, pages 1–7, 2015.

[130] S. R. Stock. X-ray microtomography of materials. *International Materials Reviews*, 44(4):141–164, 4 1999.

[131] S. R. Stock. Recent advances in X-ray microtomography applied to materials. *International Materials Reviews*, 53(3):129–181, 5 2008.

[132] S. A. Dale. *Internal structures of wet granulation agglomerates: Measurement, formation, and influence on granule breakage.* PhD thesis, Purdue University, 2014.

[133] E. M. A. Anas, S. Y. Lee, and M. D. Kamrul Hasan. Classification of ring artifacts for their effective removal using type adaptive correction schemes. *Computers in Biology and Medicine*, 41(6):390–401, 2011.

[134] G. R. Davis and J. C. Elliott. X-ray microtomography scanner using time-delay integration for elimination of ring artefacts in the reconstructed image. *Nuclear Instruments and Methods in Physics Research, Section A: Accelerators, Spectrometers, Detectors and Associated Equipment*, 394(1-2):157–162, 1997.

[135] S. Titarenko, P. J. Withers, and A. Yagola. An analytical formula for ring artefact suppression in X-ray tomography. *Applied Mathematics Letters*, 23(12):1489–1495, 2010.

[136] C. Antoine, P. Nygård, Y. W. Gregersen, R. Holmstad, T. Weitkamp, and C. Rau. 3D images of paper obtained by phase-contrast X-ray microtomography: image quality and binarisation. *Nuclear Instruments and Methods in Physics Research Section A: Accelerators, Spectrometers, Detectors and Associated Equipment*, 490(1-2):392–402, 9 2002.

[137] B. De Man, J. Nuyts, P. Dupont, G. Marchal, and P. Suetens. Metal streak artifacts in X-ray computed tomography: a simulation study. *IEEE Transactions on Nuclear Science*, 46(3):691–696, 6 1999.

[138] P. R. Laity and R. E. Cameron. Changes in small-angle X-ray scattering during powder compaction - An explanation based on granule deformation. *Powder Technology*, 198(3):404–411, 2010.

[139] Mathworks Inc. *Image Processing Toolbox User's Guide.* Mathworks, Natick, MA, 2016a edition, 2016.

[140] C. L. Martin. Elasticity, fracture and yielding of cold compacted metal powders. *Journal of the Mechanics and Physics of Solids*, 52(8):1691–1717, 2004.

[141] B.J. Briscoe and S.L. Rough. The effects of wall friction on the ejection of pressed ceramic parts. *Powder Technology*, 99(3):228–233, 10 1998.

VITA

VITA

Shrikant Swaminathan obtained his Bachelor's degree in Mechanical Engineering form Mumbai University in Summer 2009. He was accepted in the Master's program in the School of Mechanical Engineering at Purdue University in Fall 2009. He worked with Prof. Carl R. Wassgren Jr. in the Particulate Systems Group. and obtained a Master's degree in August 2012. He continued with his PhD in the same group and is expected to obtain his degree in August 2016. His work focused on understanding picking and sticking in pharmaceutical powder compacts was funded by Eli Lilly & Company. While in graduate school Shrikant interned at Pfizer, Inc. (Groton,CT), Vertex Pharmaceuticals Inc. (Cambridge, MA) and IBM (Fishkill, NY). Shrikant Swaminathan accepted a position in Alkermes Pharmaceuticals Inc. in Waltham Massachusetts and is expected to begin in July, 2016.